Chapter 1

Mie-Scattering Ellipsometry

Yasuaki Hayashi and Akio Sanpei

Additional information is available at the end of the chapter

http://dx.doi.org/10.5772/intechopen.70278

Abstract

The size and refractive index of particles can be analyzed through the measurement of polarization state of scattered light. The change of polarization state in Mie scattering has been represented by ellipsometric parameters, Ψ and Δ, like the reflection ellipsometry. The analysis method is called Mie-scattering ellipsometry. By in-process Mie-scattering ellipsometry, the growth processes of carbon particles in argon plasma and in methane plasma were analyzed. It was found that carbon particles grow by coagulation in argon plasma, while they grow by carbon coating in methane plasma. It is also shown that imaging Mie-scattering ellipsometry has the potential for the easier confirmation of optical adjustment from a long distance, as well as for the analysis of spatial distribution of particle size.

Keywords: Mie-scattering ellipsometry, Mie scattering, fine particles, monitoring, imaging ellipsometry, imaging Mie-scattering ellipsometry, dusty plasma, Coulomb crystal

1. Introduction

In the same way as in the commonly-used ellipsometry for thin-film analysis by the reflection of polarized light, the size and refractive index of particles can be analyzed through the measurement of polarization state of the scattered light. The change of polarization state in the size range of Mie scattering is able to be defined by using ellipsometric parameters, Ψ and Δ, like the reflection ellipsometry. The analysis method is called Mie-scattering ellipsometry [1–3].

The evaluation of size and size distribution of fine particles is important for their research and production. Since 1994, it has become possible to observe fine particles stationarily suspended in plasmas forming Coulomb crystals [3–5]. In such states, the position and movement of individual fine particles are easily analyzed.

Mie-scattering ellipsometry, including polarization-sensitive light scattering measurement method, was applied for the analyses of the growth of fine particles of amorphous carbon

[2, 3, 6–9] and amorphous silicon [10]. Lately, image sensors were used for the detection of scattered light instead of photodetector [11, 12]. It is a kind of imaging ellipsometry of Mie scattering. Imaging Mie-scattering ellipsometry has the potential for the analysis of spatial distribution of particle size and the easy confirmation of optical adjustment from a long distance [12].

Mie-scattering ellipsometry in Ψ-Δ two-dimensional (2D) plane enables more detailed analysis than the conventional polarization-ratio method [13] or polarization-sensitive method [9], which effectively applies only one ellipsometric parameter in the size region of monotone function. Although "scattering ellipsometry" was termed in the book of "Ellipsometry and Polarized Light" by Azzam and Bashara [14], the detailed description of its analytical method is not shown there. The analysis of trajectory of ellipsometric parameters depicted in the Ψ-Δ coordinate plane by *in situ* ellipsometry during growth of fine particles brings a lot of information about the growth in the same way as the *in situ* refection ellipsometry during film growth [15–21].

In this chapter, the principium of Mie-scattering ellipsometry, its application, imaging method, and their systems are presented.

2. Principium of Mie-scattering ellipsometry

In the same way as in the reflection ellipsometry, ellipsometric parameters Ψ and Δ for the Mie scattering are defined by the ratio between two complex scattering amplitudes in the direction parallel to the scattering plane and their vertical direction [1]. When particles are spherical and monodisperse, the ellipsometric parameters Ψ and Δ are defined by the ratio of the scattering amplitude functions [22] of a parallel polarization component ($\boldsymbol{S_p}$), which is in the scattering plane, to that of a perpendicular one ($\boldsymbol{S_s}$) as

$$\tan\Psi \cdot \exp(\mathrm{i}\Delta) = \frac{\boldsymbol{S_p}}{\boldsymbol{S_s}} \tag{1}$$

$\boldsymbol{S_p}$ and $\boldsymbol{S_s}$ are complex numbers and functions of the scattering angle, the diameter of particles, and the refractive index. The procedures of calculation of $\boldsymbol{S_p}$ and $\boldsymbol{S_s}$ from particle size and its optical index are given in [22, 23].

When particles are polydisperse in the size range of Mie scattering, the scattered light generally results in some depolarization even if the incident light is fully polarized [24]. In this case, the Stokes vector and the Mueller matrix are required for the calculation of polarization state. When incident light is linearly polarized with the azimuth at 45° to the scattering plane, the Stokes vector of scattered light from a particle "i" of a certain diameter is

$$\begin{pmatrix} I_i \\ Q_i \\ U_i \\ V_i \end{pmatrix} = I_0\left(|\boldsymbol{S_p}|^2 + |\boldsymbol{S_s}|^2\right)\begin{pmatrix} 1 \\ -\cos(2\Psi_i) \\ \sin(2\Psi_i)\cos(\Delta_i) \\ -\sin(2\Psi_i)\sin(\Delta_i) \end{pmatrix}, \tag{2}$$

where Ψ_i and Δ_i are the ellipsometric parameters for the particle " i," and I_0 is a constant proportional to the particle density and independent of the diameter. The total Stokes vector of polydisperse particles is obtained by the summation of all Stokes vectors as

$$I = \sum_i I_i, \qquad Q = \sum_i Q_i, \qquad U = \sum_i U_i, \qquad V = \sum_i V_i. \tag{3}$$

Generally, the two polarization components of the light scattered from polydisperse particles are imperfectly coherent. When the degree of coherence is expressed by μ, the ellipsometric parameters Ψ and Δ for the particles are defined here with the Stokes parameters as

$$\begin{pmatrix} I \\ Q \\ U \\ V \end{pmatrix} = I \begin{pmatrix} 1 \\ -\cos(2\Psi) \\ \mu \sin(2\Psi)\cos(\Delta) \\ -\mu \sin(2\Psi)\sin(\Delta) \end{pmatrix}, \tag{4}$$

that is,

$$\Psi = -\frac{1}{2}\cos^{-1}\frac{Q}{I}, \tag{5a}$$

$$\Delta = -\tan^{-1}\frac{V}{U} \quad \text{for } U \geqq 0, \quad \text{otherwise} \bigoplus 180^\circ. \tag{5b}$$

Thus, the ellipsometric parameters Ψ and Δ for polydisperse particles are obtained independently of the degree of coherence μ.

3. Monitoring and analyses by Mie-scattering ellipsometry

3.1. Ψ-Δ trajectory in growth of polydisperse fine particles

The ellipsometric parameters of polydisperse particles are calculated as functions of mean size and size distribution spread. For the calculation, the lognormal size distribution function, which was verified as appropriate to apply to the coagulation process of particles [25], is expressed as

$$N(D) = \frac{1}{\sqrt{2\pi}D\ln\sigma} e^{-\frac{(\ln D - \ln D_m)^2}{2(\ln\sigma)^2}}, \tag{6}$$

where D is the particle diameter, D_m is the geometric mean diameter, and σ is the geometric standard deviation.

Figure 1 shows the evolution of the ellipsometric parameters in the increase of geometric mean diameter with the refractive index of 2.5–0.75i, which is the value for an evaporated carbon foil, the scattering angle of 90°, and the geometric standard deviations of 1.0 (monodispersion), 1.2, and 1.5.

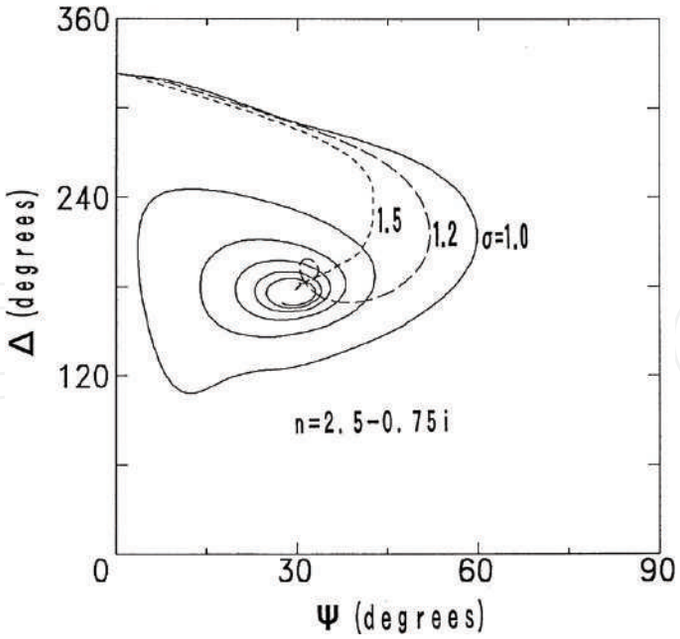

Figure 1. Calculated trajectories of the ellipsometric parameters for growing particles. Values used in the calculation are: 2.5–0.75*i* for the refractive index, 90° for the scattering angle, and 1.0, 1.2, and 1.5 for the geometric standard deviations [1].

3.2. System layout for Mie-scattering ellipsometry

Figure 2 shows the system layout for the Mie-scattering ellipsometry. The incidence light beam from an argon-ion laser (wavelength: 488 nm, output power: 100 mW) was linearly polarized at an azimuth of 45° from the plane of scattering through a Glan-Taylor prism polarizer. Its polarization state is expressed as $\chi = 1$, because $E_p = E_s$. After the scattering from particles in plasma, the polarization state of the light χ' was determined at a right angle from the incident beam line by use of a rotating-analyzer system directly driven by a stepper motor [26]. Light intensity was measured during the rotation of analyzer by two modes: with and without a quarter-wave plate, by using a computer-controlled in-and-out mechanism. When the fast axis of the quarter-wave plate is set in the scattering plane, scattered light intensity changes with analyzer azimuth A as

$$\mathcal{I}(A) = I + Q\cos 2A + U\sin 2A \quad \text{for without quarter-wave plate,} \tag{7a}$$

$$\mathcal{I}(A) = I + Q\cos 2A + V\sin 2A \quad \text{for with quarter-wave plate.} \tag{7b}$$

Thus, all four Stokes parameters are determined through the Fourier integral of Eqs. (7a) and (7b). Then, the ellipsometric parameters Ψ and Δ, which is uniquely determined in the full range of 360°, are calculated by Eqs. (5a) and (5b).

A parallel-plate rf (radio frequency) discharge reactor (rf electrode diameter: 5 cm, grounded electrode size: 22 cm × 6.5 cm, and separation of the electrodes: 2.0 cm) was used in the experiments (**Figure 3**). Argon or methane gas was introduced into the chamber at a position far from the plasma region so as not to disturb or evacuate the suspended particles with its flow. After the generation of plasma at a pressure of 40 Pa and an rf power of 2 or 8 W, the

http://dx.doi.org/10.5772/intechopen.70278

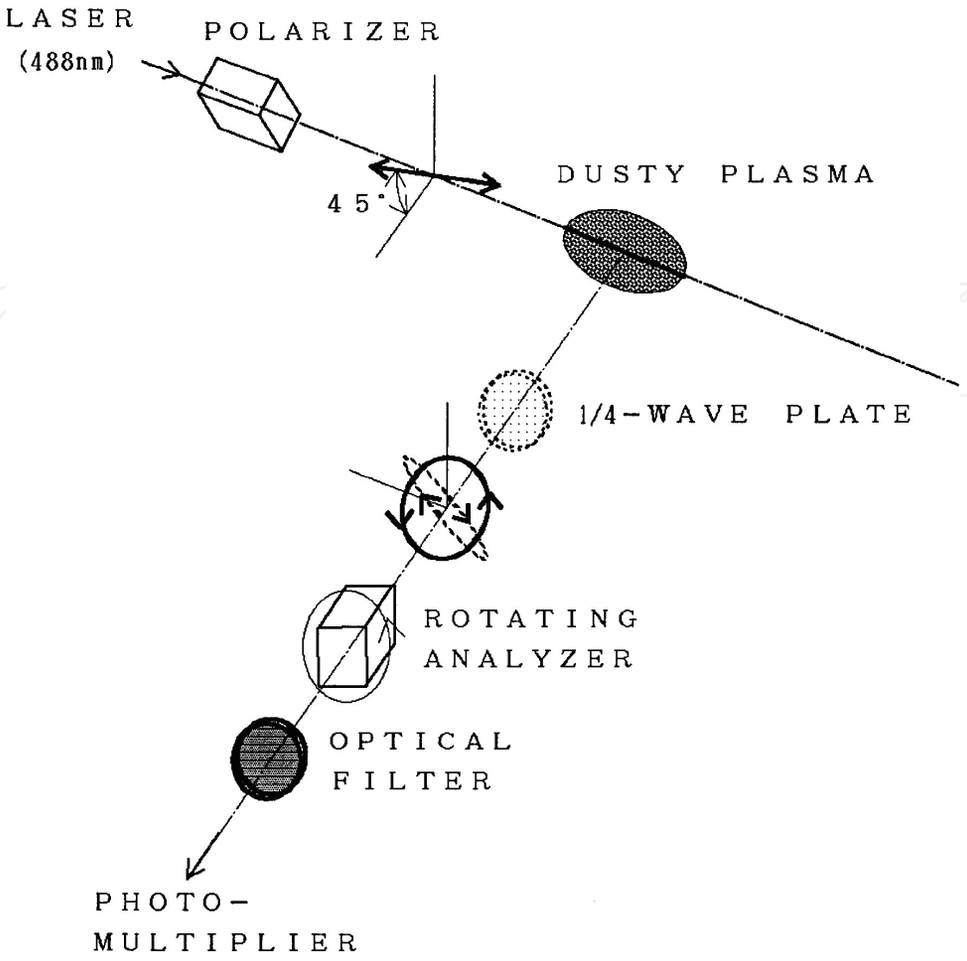

Figure 2. Schematic arrangement for the measurement of Mie-scattering ellipsometry. Incident light from an argon-ion laser is linearly polarized. The polarization state of light scattered from particles is analyzed with the use of a quarter-wave plate and a rotating-analyzer system [1].

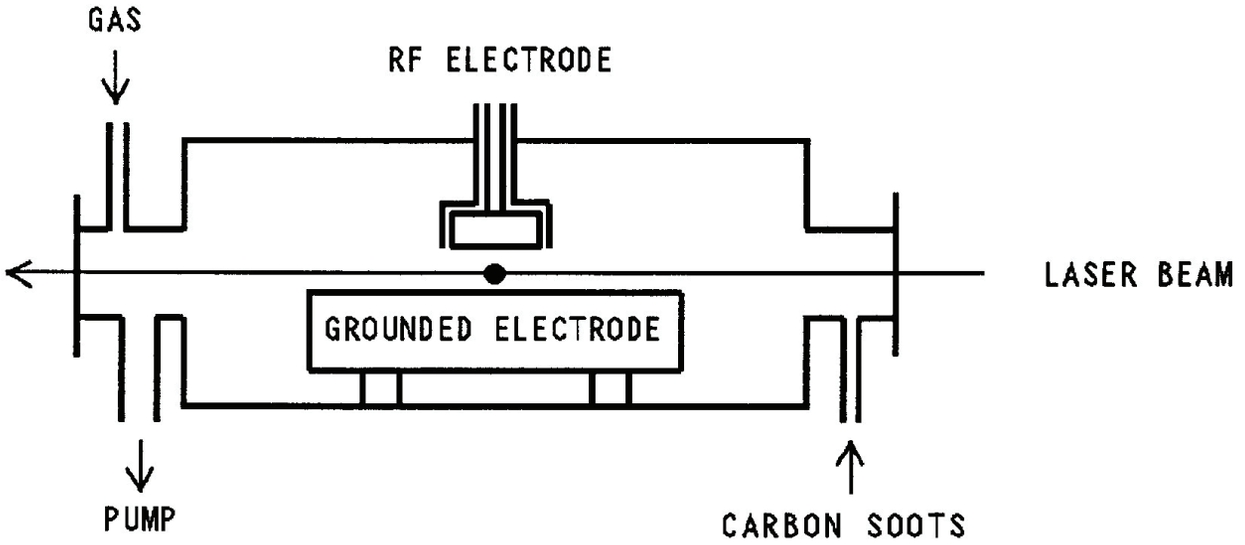

Figure 3. Experimental setup for the measurement of carbon particle growth [2].

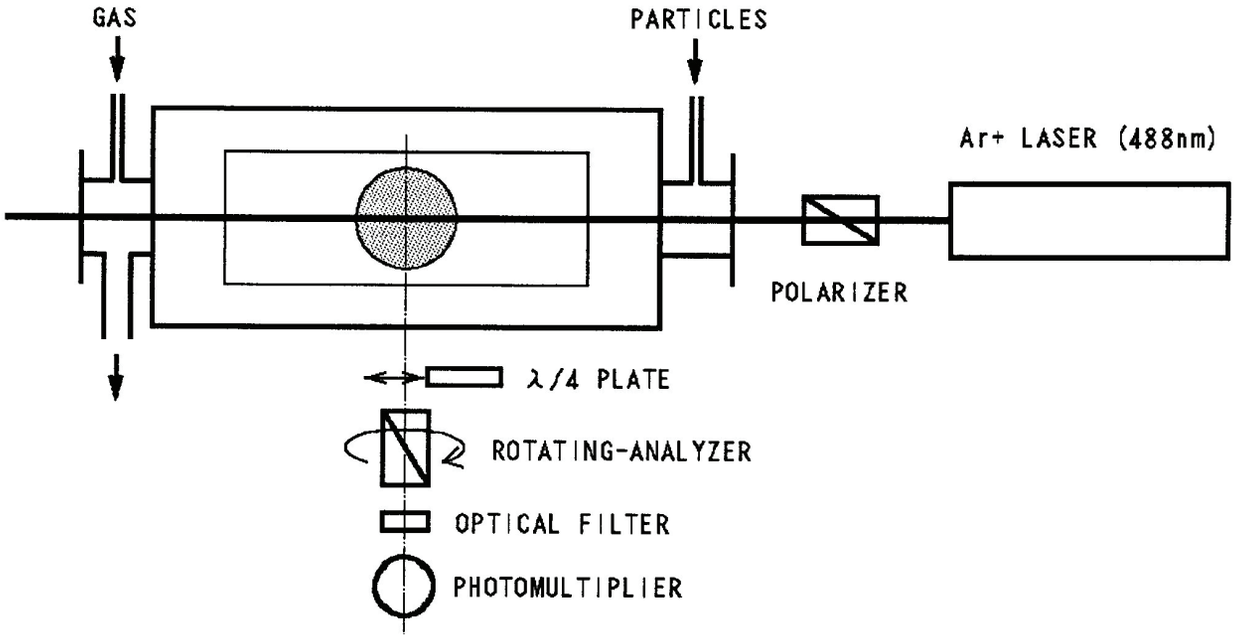

Figure 4. System configuration for Mie-scattering ellipsometry measurement in rf plasma reactor (top view).

ultra-fine particles of carbon were supplied all at once into the plasma. Then the ellipsometric measurement was started. The observation point was fixed at a position 1.2 cm below the rf electrode on the center axis, which was located in the plasma bulk.

System configuration for the measurement of Mie-scattering ellipsometry during the growth of carbon fine particles in the rf plasma reactor is shown in **Figure 4**.

3.3. *In situ* measurement by Mie-scattering ellipsometry

3.3.1. Carbon particle growth by coagulation in argon plasma

Argon gas was introduced into the chamber at a position far from the plasma region so as not to disturb or evacuate the suspended particles with its flow. After the generation of argon plasma at a pressure of 40 Pa and an rf power of 2 W, the particles of carbon soot were supplied all at once into the plasma. Then the ellipsometric measurement was started [1].

The particles were observed from the scattering light to be located at both sides of the measurement position on the laser beam line in the early period. At about 700 seconds after the injection, the light intensity gradually increased at the measurement position. The induction period depended on the experimental conditions. The evolution of the ellipsometric parameters after the initial period is shown on the Ψ-Δ coordinate plane in **Figure 5(a)**. A data point shows the average value of five measurements and data were taken every 9 seconds. During the evolution, the parameter Δ decreased gradually at first and rapidly. The evolution shows larger Δ at the beginning as compared with the calculated trajectories in **Figure 1**. It is understood from the calculation that the difference depends mainly on the employed refractive index of particles.

In order to fit the calculated trajectory to the experimental data, the simulation was carried out changing parameters; in steps of 0.1 for the real part of the refractive index, 0.05 for the

imaginary part, 1 degree for the scattering angle, and 0.1 for the geometric standard deviation along with the assumption of lognormal size distribution of polydisperse particles. The best-fit trajectory was obtained at the refractive index of 2.3–0.35*i*, the scattering angle of 91°, and the standard deviation of 1.5 as shown in **Figure 5(b)**. The smaller value of refractive index than that of evaporated carbon may be due to the inclusion of voids in the carbon particles. It can be estimated from the geometric standard deviation of 1.5 that 68% of all particles have diameters from D_m/1.5 to 1.5D_m.

From the correspondence to the best-fit trajectory, the geometric mean diameter was determined for each experimental data point. Then the particle density was evaluated with the known diameter and the measured scattered intensity. **Figure 6** gives the results and shows that the density gradually increases until the particle begins to grow and then rapidly decreases.

The bright region in the plasma formed by Mie scattering, where particles were distributed, was observed by the naked eye under the same plasma conditions. The region was initially dome-shaped. However, it became concentrated at the center axis and moved toward the rf electrode at the same time [23]. The transition may be due to the time evolution of plasma potential interacting with and interacted by negatively charged particles. The particle transfer and concentration causes coagulation, resulting in the increase of the diameter. Then, the plasma potential distribution is affected and enhances the movement. The abrupt decrease of the density at around 800 s in **Figure 6** supports this speculation.

3.3.2. Carbon particle growth by coating in methane plasma

The inlet port of methane gas was located near a pumping port so as not to disperse particles trapped in methane plasma, which was maintained under the conditions of 40 Pa gas pressure, 16 sccm gas flow rate, and 8 W rf power. Ultra-fine carbon particles were injected instantaneously into the plasma through another gas inlet port [2].

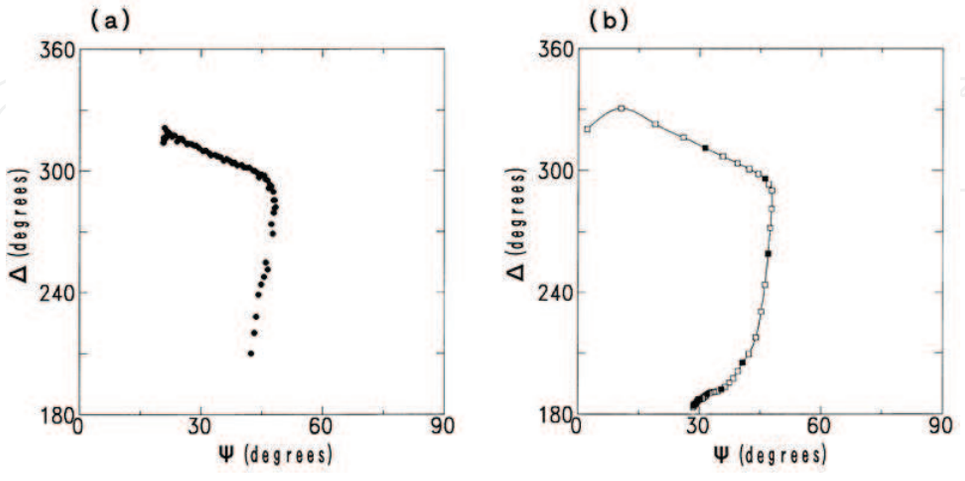

Figure 5. Experimental (a) and simulated (b) results of evolution of the ellipsometric parameters. The solid line (in (b)) shows the best-fit simulated trajectory: values used in the calculation are 2.3–0.35*i* for the refractive index and 91° for the scattering angle. The rectangles on the best-fit trajectory indicate geometric mean diameter increases every 20 nm, and the closed rectangles those every 100 nm [1].

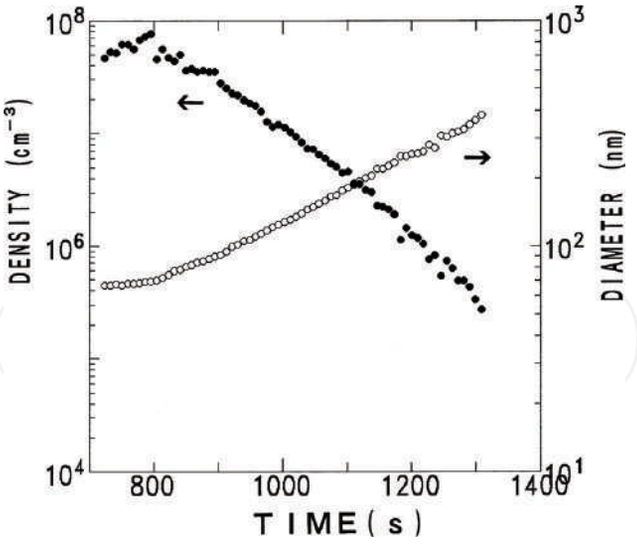

Figure 6. Evolution of density and geometric mean diameter of particles in trap at the measurement point in plasma bulk. Closed circles indicate the density and open circles the mean diameter [1].

After the injection of ultra-fine carbon particles in the plasma, the bright region of Mie scattering was observed visually. The region existed only around the sheath-plasma boundary near the rf electrode for the first 300 second, and then extended into the plasma bulk in the shape of a dome, keeping the almost same shape for about 2000 seconds.

The evolution of the ellipsometric parameters during the period is shown by points on the Ψ-Δ coordinate plane in **Figure 7**. The data were taken from 200 to 2300 seconds after the injection of ultra-fine carbon particles in the plasma. First, the parameter Ψ increased gradually with a slight change of Δ, and at $\Psi > 45°$, loops running counterclockwise were observed on the coordinate plane. Similar trajectories of the ellipsometric parameters with the same speed of

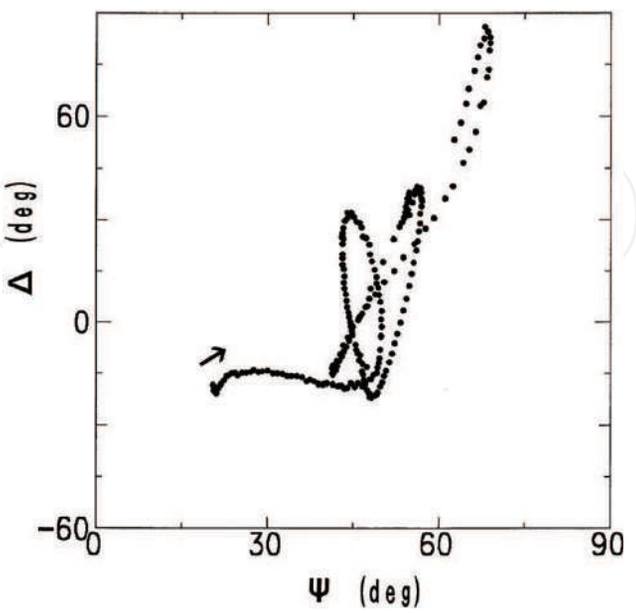

Figure 7. Experimental results of evolution of the ellipsometric parameters during carbon particle growth [2].

evolution were depicted at the other measurement positions on the center axis, except for the plasma-sheath boundaries. From the results mentioned above, it can be supposed that the particles in the plasma bulk had the same size distribution during the period.

The calculation of Mie-scattering ellipsometry of spherical polydisperse particles [1] was performed for the analysis of the experimental data. **Figure 8(a)** shows the results of the

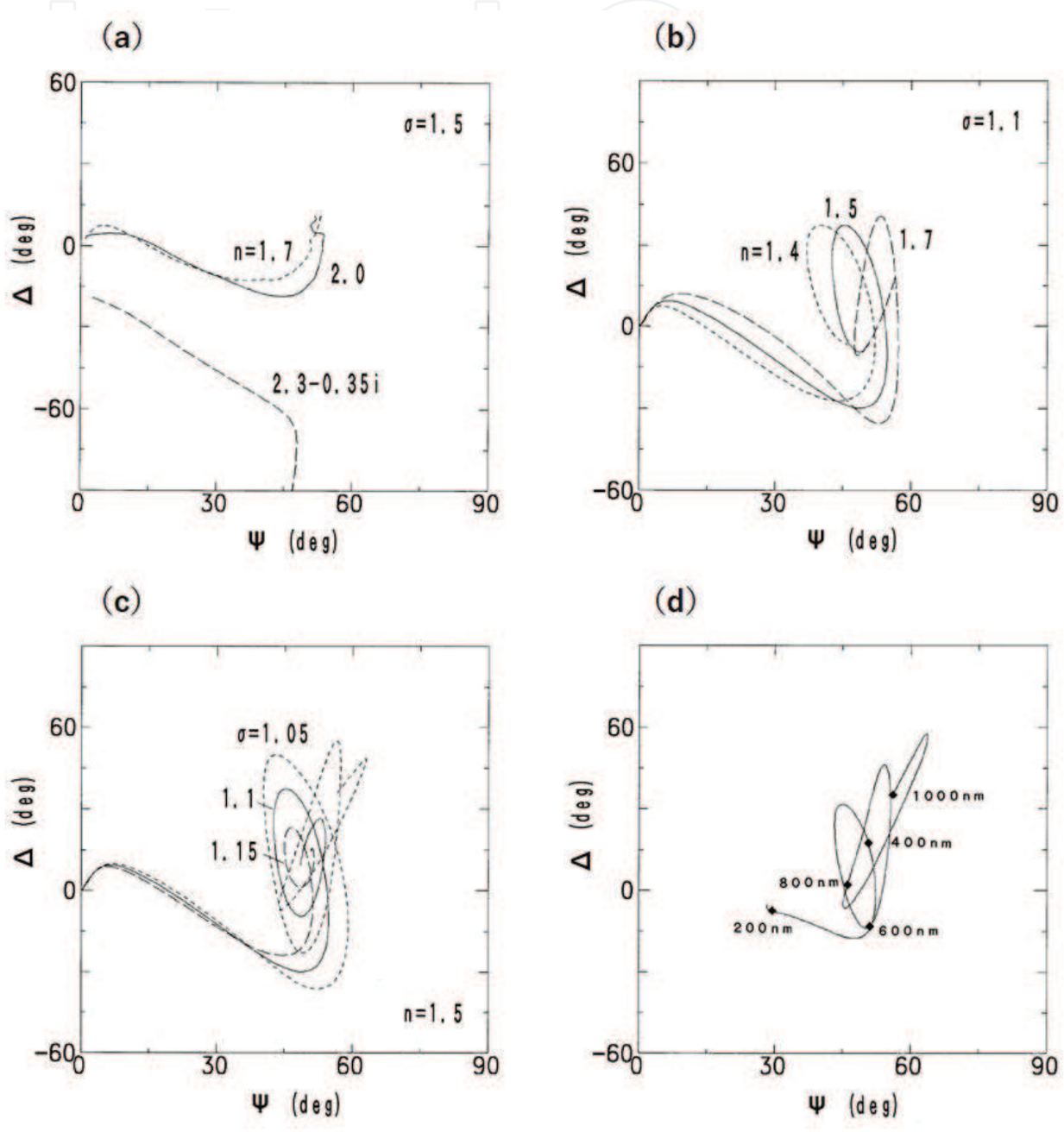

Figure 8. Evolution of the ellipsometric parameters by simulation: (a) the assumed geometric standard deviation of size distribution is 1.4, and the assumed refractive indexes are 2.3–0.35*i*, 2.0, and 1.7; (b) the assumed geometric standard deviation is 1.1, and the assumed refractive indexes are 1.7, 1.5, and 1.4; (c) the assumed geometric standard deviations are 1.15, 1.1, and 1.05, and the assumed refractive index is 1.5; (d) the translation-operated log-normal size distribution on a linear size scale is assumed with the refractive index of 1.5, and the geometric mean size and the geometric standard deviation are 50 nm and 2.0, respectively for the first lognormal distribution [2].

simulation for the growth of an ensemble of particles with a constant geometric standard deviation 1.5 for the lognormal size distribution, of which three different values of refractive index; 2.3–0.35*i*, 2.0, and 1.7, were assumed. The standard deviation and the first index are the values observed in the coagulation process of carbon particles as shown in 3.3.1. The last index is that of a hydrogenated amorphous carbon film at 488 nm [27]. As the particle diameter increases, the trajectory turned clockwise for absorbing particles, while counterclockwise for nonabsorbing particles. From the comparison of the experimental results with the calculation, it is seen that the growing particles are nonabsorbing and have the refractive index of a real number.

The calculated parameters converge to certain values while the experimental ones oscillate remarkably. Then, the calculation with a smaller geometric standard deviation of 1.1 was executed for refractive indexes of 1.7, 1.5, and 1.4 as shown in **Figure 8(b)**. It is seen that the trajectories draw loops. The inclination of the first loop of the experimental data is close to that with the index of 1.5.

Figure 8(c) shows the ellipsometric parameters in further evolution calculated in the case of a fixed refractive index of 1.5 with different geometric standard deviations of 1.15, 1.1, and 1.05. Comparing the results with the experimental trajectory, it can be seen that the standard deviation decreases with the increase of particle size, that is, the size distribution became a rather monodisperse one.

When fine particles grow by coating, size distribution function changes to that of translation-operated lognormal on a linear size scale as

$$N(D) = \frac{1}{\sqrt{2\pi}(D - D_c)\ln\sigma} e^{-\frac{\{\ln(D-D_c)-\ln D_m\}^2}{2(\ln\sigma)^2}}, \tag{8}$$

where D_c means the thickness of coated material on the seeds of ultra-fine particles of the lognormal size distribution function as Eq. (6). **Figure 8(d)** shows the result of the simulation: the geometric mean size and the geometric standard deviation for the distribution of the injected particles are 50 nm and 2.0, respectively, and the refractive index is 1.5. The simulated trajectory agrees with the experimental results better than those in **Figure 8**(a–c). The deviation of the trajectory from the experimental one at the start may be due to the difference of the refractive index between hydrogenated carbon and pure carbon.

Figure 9(a) shows the variation of the value of Δ with time for the coating growth of carbon under conditions similar to those shown above. The best-fitted trajectory by simulation was obtained for the geometric mean size and the geometric standard deviation for the distribution of the injected particles is 50 nm and 1.5, respectively, and the refractive index is 1.53. The variation of Δ value with time for the best-fitted trajectory is shown in **Figure 9(b)** [3]. Characteristics of the two curves in the peaks and dips correspond well to each other. The growing particle diameter was determined from the correspondence. The time evolution of the particle diameter so determined is plotted in **Figure 10**. It is seen that the diameter increases almost linearly for about the first 1500 seconds, then the growth rate decreases gradually. This suggests that the state of particle plasma has changed at about 1500 seconds The density of

http://dx.doi.org/10.5772/intechopen.70278

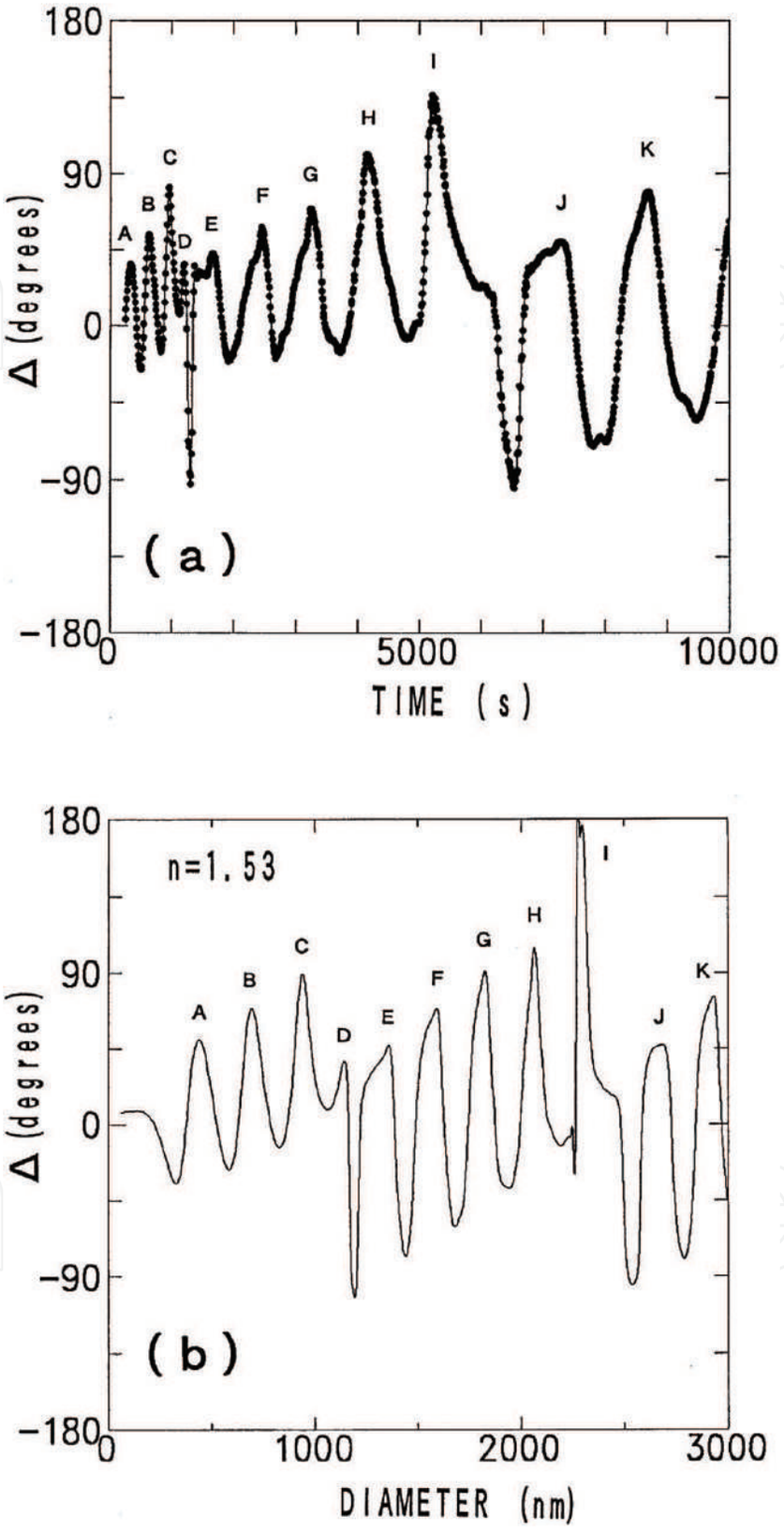

Figure 9. Experimentally obtained evolution of the ellipsometric parameter Δ with time (a), and calculated Δ as a function of the particle diameter with the refractive index 1.53 (b) [3]. The correspondence of the peaks is indicated by the same letters in both figures.

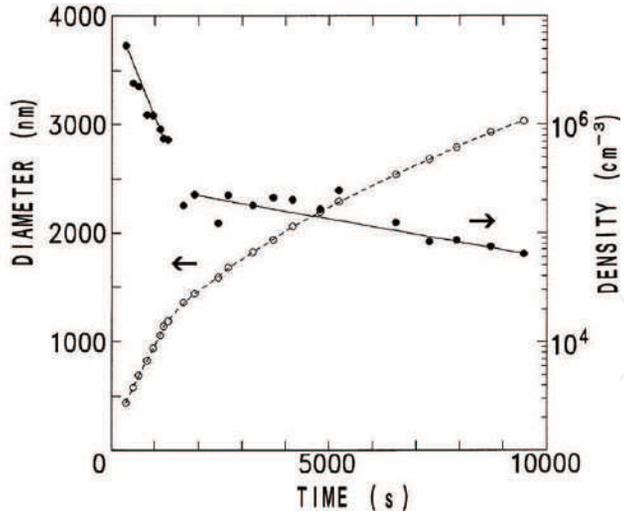

Figure 10. Evolution of particle diameter (open circles and a broken curve) and density (closed circles and solid lines) with time [3].

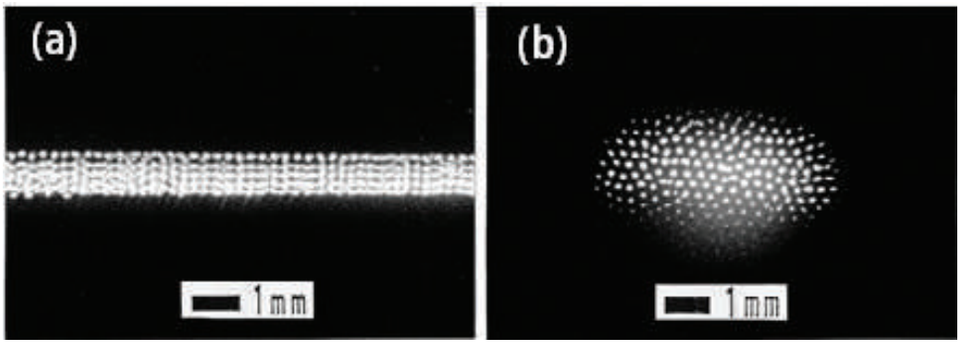

Figure 11. Photographs of a Coulomb crystal viewed from the side port (a) and the upper port (b) of the reactor [3].

particles is determined from the scattered light intensity, which is calibrated by the density evaluated from the interparticle distances in the photo of the Coulomb crystal formed in the plasma as shown in **Figure 11** [3]. It is seen in **Figure 10** that the density decrease is rapid for the first 1500 seconds, but subsequently becomes slow. It is speculated that the particles escape laterally from the plasma region through the side of the electrode gap before they are bound to one another, but they cannot escape easily after the Coulomb crystal is formed. From the consideration, it can be said that the phase transition from the state of "liquid" to that of "solid" [26] occurs at around 1500 seconds after the particle injection. At the point, the particle diameter is 1300 nm and the density is 3×10^5 cm^{-3}. The transition was also confirmed from the magnified photographs taken at times later than 1800 s, in which the particles were observed to be gradually arranged. The Wigner-Seitz radius is calculated from the density N as $[3/(4\ \pi N)]^{1/3}$ [28], and becomes about 90 μm at the phase transition.

The particles suspended in plasma were observed after the growth using a scanning electron microscope (SEM). All particles were single spheres. **Figure 12** shows a SEM micrograph for the particles suspended in plasma for 3 h. It is seen that the particles are nearly spherical and equal in size with the diameter of 3.0–3.1 μm. The spherical shape supports the former discussion on Mie-scattering ellipsometry and coating growth mechanism.

http://dx.doi.org/10.5772/intechopen.70278

Figure 12. Typical SEM micrograph of particles suspended in plasma for 3 h.

From these results, it can be speculated about the growth of the carbon particles as follows. Hydrogenated amorphous carbon coated the ultra-fine carbon particles in methane plasma. About the smaller value of refractive index than that of a hydrogenated amorphous carbon, it can be understood that the void of 25% volume fraction was included in the coated carbon. Without the homogeneous nucleation of carbon particles in the plasma, which was confirmed by the fact that the Mie-scattered light is not observed in methane plasma without the injection of carbon ultra-fine particles under the same plasma conditions, the particles were equally coated independent of their initial size. From the spherical shape of the grown particles, it is imagined that the particles were coated isotropically. These grown particles with diameter of more than 3 μm can be suspended in methane plasma.

4. Imaging Mie-scattering ellipsometry

Imaging Mie-scattering ellipsometry, like the imaging ellipsometry for thin film analysis, enables the analysis of spatial distribution of particle size, as well as the easier confirmation of optical adjustment from a long distance. The difference between imaging Mie-scattering ellipsometer and above-mentioned Mie-scattering ellipsometer is the imaging of the distribution of fine particles using a 2D image sensor instead of a photodetector.

4.1. Experimental setup for imaging Mie-scattering ellipsometry

Ellipsometric measurement by a system with a rotating compensator has an advantage of the determination of all four Stokes parameters in one rotation. The light intensity changes by the rotation of compensator, whose azimuth is C, is expressed by sinusoidal function as [29, 30],

$$\mathcal{I}(C) = A_0 + A_2 \cos 2C + B_2 \sin 2C + A_4 \cos 4C + B_4 \sin 4C. \tag{9}$$

When the azimuth angle of the polarizer (P) and that of the analyzer (A) are 90 and ±45°, respectively, and the rotating compensator is put between the polarizer and particles, Fourier coefficients indicated in Eq. (9) are related with Ψ and Δ for particles as,

$$\Psi = \frac{1}{2} \tan^{-1} \frac{\sqrt{{B_4}^2 + \frac{1}{4}{B_2}^2}}{A_4} \quad \text{for } A_4 \geqq 0, \text{ otherwise} \bigoplus 90°, \tag{10a}$$

$$\Delta = \tan^{-1} \frac{B_2}{2B_4} \quad \text{for } B_4 < 0 (\mathrm{A} = 45°);\ B_4 \geqq 0 (\mathrm{A} = -45°), \text{ otherwise} \bigoplus 180°. \tag{10b}$$

The system for the experimental example of imaging Mie-scattering ellipsometry is shown in **Figure 13** [12]. The ellipsometer consists of polarizer and analyzer modules and a 2D image sensor. The polarizer module includes a 532 nm wavelength laser, a polarizer (P = 90°), and a rotating compensator. The analyzer module includes a wire grid polarizer (A = −45°) and a mirror. A digital video camera containing a 2D image sensor for the detection of 2D distributed

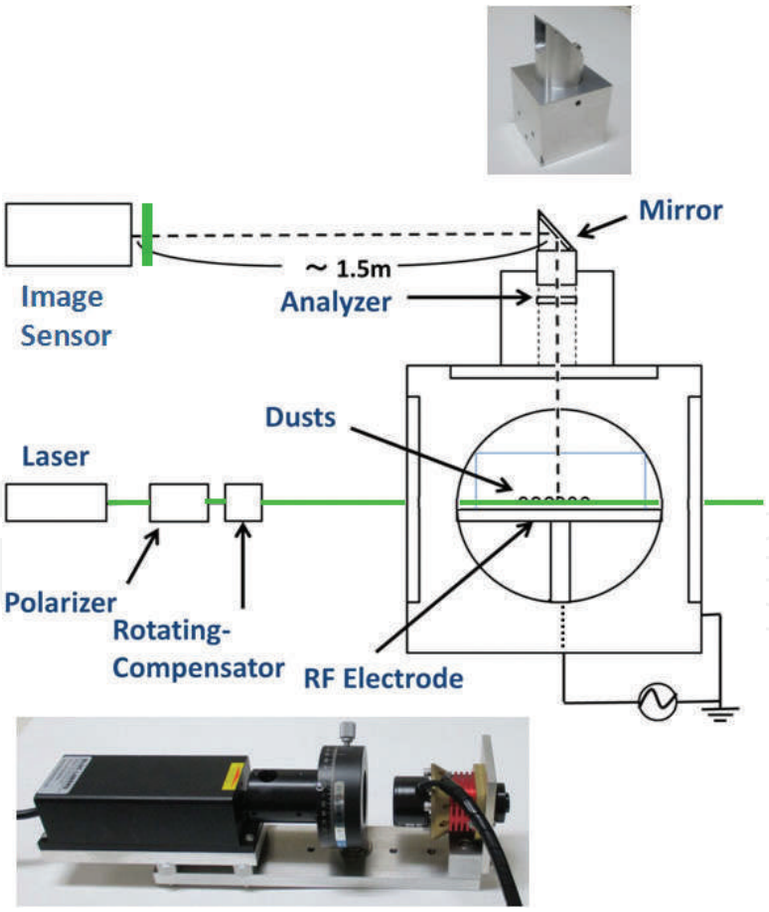

Figure 13. Schematic of ellipsometry measurement with dust plasma chamber. Inserted upper and lower photos are analyzer module and polarizer module, respectively [12].

light intensity was placed 1.5 m apart from the analyzer module. An optical band-pass filter with 1 nm FWHM at 532 nm is attached in front of the video camera. The images of distribution of fine particles by scattered light are expanded and focused using built-in functions and an extra lens. Thirty 2D images were captured every second. Although a rotating compensator is set in analyzer modules in conventional rotating-compensator ellipsometers [31, 32], it was set in the polarizer module in this case for the analyzer module able to be installed in a vacuum vessel.

The polarizer module and the digital video camera can be attached to view windows of a large plasma device in the atmosphere. The analyzer module is prepared to be fixed in a vacuum vessel [12]. It was ascertained that an image reflected by the mirror in the analyzed module could be viewed and recorded with the video camera out of the vacuum vessel of the large helical devise (LHD), a nuclear fusion experimental devise in Toki in Japan, when laser light was scattered by a small test material placed at the point of dust particle measurement.

4.2. Experiments of imaging Mie-scattering ellipsometry

In order to confirm the functional capability of the ellipsometric system, a preliminary experiment was carried out using a small dust plasma cubic chamber, 15 cm on a side [33]. Spherical divinylbenzene polymer particles of 2.27 μm in diameter with a dispersion degree of 0.1 μm were injected and suspended in argon plasma under a pressure of 50 Pa.

Light intensity data for 1600 pixels in the area covering the light scattering image were less than 75 of the maximum value of 255. Average values, i.e., total summed values of the data divided by pixel number, were calculated for images every 6° of compensator azimuth angle. The average light intensity (C_n) was obtained for each provisional azimuth angle C_n, where $C_n = 6n$. Then, Fourier analysis was performed and coefficients were obtained. After the difference between true compensator azimuth angle C and provisional one C_n was calculated through the obtained Fourier coefficients, true Fourier coefficients were calculated as

$$A_0 = 6.9009, \quad A_2 = 0, \quad B_2 = -0.9281, \quad A_4 = -1.2814, \quad B_4 = -0.6747. \tag{11}$$

Finally, ellipsometric parameters are determined by Eqs. (6a) and (6b) as

$$\Psi = 73.7^\circ, \quad \Delta = 214.5^\circ. \tag{12}$$

These values are plotted in Ψ-Δ coordinate (**Figure 14**). Meanwhile, Ψ and Δ was calculated based on the Mie scattering theory for the values of the refractive index of 1.56 (for divinylbenzene), the diameter of 2.22–2.30 μm, and the scattering angle of 90°. The calculated values are also shown in **Figure 14**. It can be stated that they agree fairly well with each other and that the measurement method is reliable. This method has the advantage of easy optical adjustment from a long distance observing the image of fine particles.

Using the same system of imaging Mie-scattering ellipsometry, the spatial size distribution of parallelly layered fine particles in argon plasma was analyzed [34]. **Figure 15** shows a video image of light scattered by spherical divinylbenzene particles of 2.74±0.09 μm in diameter

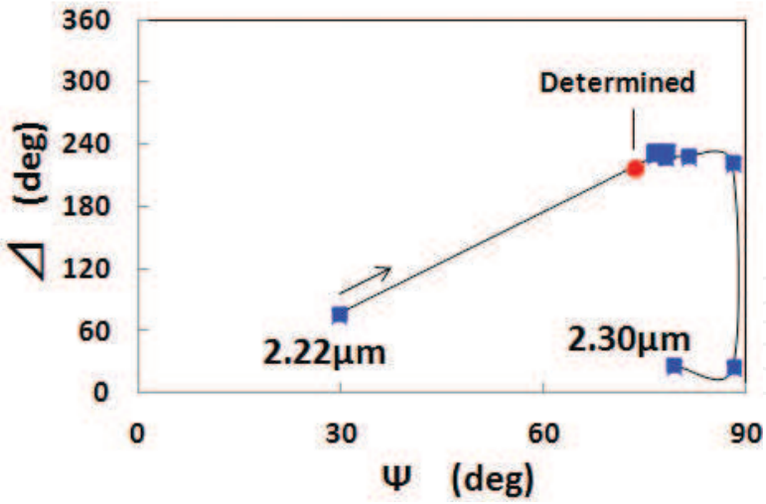

Figure 14. Ellipsometric parameters Ψ and Δ determined by measurement (circle) and calculation (squares). Calculation was carried out based on Eq. (1) and the Mie-scattering theory for the values of refractive index of 1.56, the diameter of 2.22–2.30 μm by 0.01 μm and the scattering angle of 90° [12].

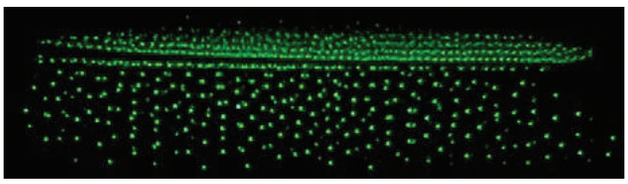

Figure 15. Video image of light scattered by spherical divinylbenzene particles of 2.74 ± 0.09 μm in diameter suspended in argon plasma at 65 Pa.

suspended in argon plasma with the pressure of 65 Pa. It is seen that the particles form vertical strings in the lower region and horizontal layers parallelly in the upper region. Fine particles more than 10 in each parallel layers were analyzed by imaging Mie-scattering ellipsometry for each area of 1320 pixels in video images. By the comparison of the determined values Ψ and Δ with calculation, the size was evaluated to be 2.70, 2.74, 2.75, and 2.77 μm for particles in upper to lower layers.

5. Conclusion

The principium of Mie-scattering ellipsometry and its analytical method were explained in detail. Then, the results of analyses by in-process Mie-scattering ellipsometry for carbon particle growth in argon plasma, as well as in methane plasma, were shown.

In argon plasma, it was suggested from the simulated trajectory best fit to the experimental data that the carbon particles included voids and the size distribution was that of polydisperse particles, such as the diameter ranging mostly from 70 to 150 nm for the mean size of 100 nm. The mean diameter and the density of particles were evaluated, and their time dependence suggests that the size increase of the particles is mostly due to coagulation.

In the case of methane plasma, the trajectory obtained by the model of translation-operated lognormal size distribution on a linear scale agreed with experimental result better than that of lognormal of a constant geometric standard deviation. It was found that ultra-fine carbon particles were coated by hydrogenated amorphous carbon during suspension in methane plasma. The particles were equally coated independent of their initial size without homogeneous nucleation in the plasma. The spherical shape of carbon particles observed in SEM image supports that the particles were coated isotropically with carbon.

An imaging Mie-scattering ellipsometry system, consisting a laser, a polarizer, a rotating compensator, an analyzer and a 2D image sensor, was developed. It was shown that the use of a 2D image sensor instead of a photodetector enables easy confirmation of optical adjustment from a long distance by the image of fine particles without any problems for measurement. The size of distributed fine particles was determined for each separated area. The developed system of imaging Mie-scattering ellipsometer has the potential for the easier confirmation of optical adjustment from a long distance, as well as for the analysis of spatial distribution of particle size.

Acknowledgements

The authors thank Mr. Masahiro Kawano and Mr. Toshihiko Arayama for experimental assistance, and Prof. Suguru Masuzaki and Prof. Kunihide Tachibana for useful discussions. This work was partly supported by the Ministry of Education, Science, Sports and Culture of Japan under Grant Number 24244094.

Author details

Yasuaki Hayashi* and Akio Sanpei

*Address all correspondence to: hayashiy@kit.ac.jp

Kyoto Institute of Technology, Kyoto, Japan

References

[1] Hayashi Y, Tachibana K. Mie-scattering ellipsometry for analysis of particle behaviors in processing plasmas. Japanese Journal of Applied Physics. 1994;**33**(3B):L476-L478. DOI: 10.1143/JJAP.33.L476

[2] Hayashi Y, Tachibana K. Analysis of spherical carbon particle growth in methane plasma by Mie-scattering ellipsometry. Japanese Journal of Applied Physics. 1994;**33**(7B):4208-4211. DOI: 10.1143/JJAP.33.4208

[3] Hayashi Y, Tachibana K. Observation of Coulomb-Crystal formation from growing particles grown in a methane plasma. Japanese Journal of Applied Physics. 1994;**33**(6A):L804-L806. DOI: 10.1143/JJAP.33.L804

[4] Chu JH, Lin I. Direct observation of Coulomb crystals and liquids in strongly coupled rf dusty plasmas. Physical Review Letters. 1994;**72**(25):4009-4012. DOI: 10.1103/PhysRevLett.72.4009

[5] Thomas H, Morfill GE, Demmel V, Goree J, Feuerbach B, Möhlmann D. Plasma crystal: Coulomb crystallization in a dusty plasma. Physical Review Letters. 1994;**73**(5):652-655. DOI: 10.1103/PhysRevLett.73.652

[6] Tachibana K, Hayashi Y. Analysis of the Coulomb-solidification process in particle plasma. Australian Journal of Physics. 1995;**48**:469-477. DOI: 10.1071/PH950469

[7] Hayashi Y, Tachibana K. Coulomb crystal formation from growing particles in a plasma and the analysis. Journal of Vacuum Science and Technology. 1996;**14**(2):506-510. DOI: 10.1116/1.580116

[8] Hong SH, Winter J. Size dependence of optical properties and internal structure of plasma grown carbonaceous nanoparticles studies by in situ Rayleigh-Mie scattering ellipsometry. Journal of Applied Physics. 2006;**100**:064303. DOI: 10.1063/1.2338132

[9] Groth S, Greiner F, Tadsen B, Piel A. Kinetic Mie ellipsometry to determine the time-resolved particle growth in nanodusty plasmas. Journal of Physics D: Applied Physics. 2015;**48**:465203. DOI: 10.1088/0022-3727/48/46/465203

[10] Shiratani M, Kawasaki H, Fukuzawa T, Yoshioka T, Ueda Y, Singh S, Watanabe Y. Simultaneous in situ measurements of properties of particulates in rfsilane plasmas using a polarization-sensitive laser-light-scattering method. Journal of Applied Physics. 1996;**79**(1):104-109. DOI: 10.1063/1.360916

[11] Greiner F, Carstensen J, Kohler N, Pilch I, Ketelsen H, Knist S, Piel A. Imaging Mie-ellipsometry: Dynamics of nanodust clouds in an argon-acetylene plasma. Plasma Sources, Science and Technology. 2012;**21**(6):065005. DOI: 10.1088/0963-0252/21/6/065005

[12] Hayashi Y, Kawano M, Sanpei A, Masuzaki S. Mie-scattering ellipsometry system for analysis of dust formation process in large plasma device. IEEE Transactions on Plasma Science. 2016;**44**(6):1032-1035. DOI: 10.1109/TPS.2016.2542349

[13] Kerker M. The use of white light in determining particle radius by the polarization ratio of the scattered light. Journal of Colloidal Science. 1950;**5**:165-167

[14] Azzam RMA, Bashara NM. Ellipsometry and Polarized Light. Amsterdam: North Holland; 1987. p. 539

[15] Theeten JB, Hottier F, Hallais J. Ellipsometric assessment of (Ga, Al) As/GaAs epitaxial layers during their growth in an organometallic VPE system. Journal of Crystal Growth. 1979;**46**(2):245-252. DOI: 10.1016/0022-0248(79)90064-2

[16] Theeten JB. Real-time and spectroscopic ellipsometry of film growth: Application to multilayer systems in plasma and CVD processing of semiconductors. Surface Science. 1980;**96**(1-3):275-293. DOI: 10.1016/0039-6028(80)90307-6

[17] Hayashi Y, Itoh A. Ellipsometric monitor for film thickness control in plasma processes. In: Proceedings of International Ion Engineering Congress, ISIAT'83 & IPAT'83; Kyoto, Japan. 1983. pp. 1469-1474

[18] Collins RW, Pawlowski A. The nucleation and growth of glow-discharge hydrogenated amorphous silicon. Journal of Applied Physics. 1986;**59**(4):1160-1166. DOI: 10.1063/1.336553

[19] Antoine AM, Drevillon B, Roca i Cabarrocas P. In situ investigation of the growth of rf glow-discharge deposited amorphous germanium and silicon films. Journal of Applied Physics. 1987;**61**(7):2501-2508. DOI: 10.1063/1.337924

[20] Hayashi Y, Drawl W, Collins RW, Messier R. In-process ellipsometric monitoring of diamond film growth by microwave plasma enhanced chemical vapor deposition. Applied Physics Letters. 1992;**60**(23):2868-2870. DOI: 10.1063/1.106827

[21] Hayashi Y, Drawl W, Messier R. Temperature dependence of nucleation density of chemical vapor deposition diamond. Japanese Journal of Applied Physics. 1992;**31**(2B):L193-L196. DOI: 10.1143/JJAP.31.L193

[22] van de Hulst HC. Light Scattering by Small Particles. New York: Dover; 1981. p. 470

[23] Tachibana K, Hayashi Y, Okuno T, Tatsuta T. Spectroscopic and probe measurements of structures in a parallel-plates RF discharge with particles. Plasma Sources Science and Technology. 1994;**3**(3):314-319. DOI: 10.1088/0963-0252/3/3/012

[24] Deirmendjian D. Electromagnetic Scattering on Spherical Polydispersions. New York: American Elsevier; 1969. p. 290

[25] Yoshida T, Okuyama K, Kousaka Y, Kida Y. Change in particle size distributions of polydisperse aerosols undergoing Brownian coagulation. Journal of Chemical Engineering of Japan. 1975;**8**(4):317-322. DOI: 10.1252/jcej.8.317

[26] Hayashi Y. Thin film monitoring with ellipsometry in in-line processing equipment. Japanese Journal of Applied Physics. 1990;**29**(11):2514-2518. DOI: 10.1143/JJAP.29.2514

[27] Ikezi H. Coulomb solid of small particles in plasmas. The Physics of Fluids. 1986;**29**:1764-1766. DOI: 10.1063/1.865653

[28] Ichimaru S. Strongly coupled plasmas: High-density classical plasmas and degenerate electron liquids. Reviews of Modern Physics. 1982;**54**(4):1017-1059. DOI: 10.1103/RevModPhys.54.1017

[29] Hauge PS, Dill FH. A rotating-compensator Fourier ellipsometer. Optics Communications. 1975;**14**(4):431-437. DOI: 10.1016/0030-4018(75)90012-7

[30] Hauge PS. Generalized rotating-compensator ellipsometry. Surface Science. 1976;**56**:148-160. DOI: 10.1016/0039-6028(76)90442-8

[31] Lee J, Rovira PI, An I, Collins RW. Rotating-compensator multichannel ellipsometry: Applications for real time Stokes vector spectroscopy of thin film growth. Review of Scientific Instruments. 1998;**69**(4):1800-1810. DOI: 10.1063/1.1148844

[32] Weiß R, Hong S-H, Ränsch J, Winter J. Rayleigh. Mie scattering ellipsometry as an in situ diagnostic for the production of 'smart nanoparticles'. Physica Status Solidi A. 2008;**205**(4): 802-805. DOI: 10.1002/pssa.200777803

[33] Hayashi Y, Mizobata Y, Takahashi K. Experiments of fine-particle plasma using planar magnetron plasma system. International Journal of Microgravity Science and Application. 2011;**28**(2):S23-S26

[34] Hayashi Y, Sanpei A, Mieno T, Masuzaki S. Analysis of spatial distribution of fine particles in plasma by imaging Mie-Scattering ellipsometry. In: 8th International Conference on the Physics of Dusty Plasmas; 20-25 May 2017; Prague, Czech Republic

Chapter 2

Achromatic Ellipsometry: Theory and Applications

Eralci Moreira Therézio, Gustavo G. Dalkiranis, André A. Vieira, Hugo Gallardo, Ivan H. Bechtold, Patricia Targon Campana and Alexandre Marletta

Additional information is available at the end of the chapter

http://dx.doi.org/10.5772/intechopen.70089

Abstract

In the present chapter, the theory and some applications of Achromatic Ellipsometry, including transmittance, absorbance, and emission, are presented. The new methodology introduced here comprises the calculation of Stokes parameters using Fourier series analysis. Light polarization was determined by calculating the polarization degree, anisotropy, asymmetry parameters, and rotational and ellipsometry angles. The nematic liquid crystal E7™ doped with 4,7-bis{2-[4-(4-decylpiperazin-1-yl) phenyl]ethynyl}-[2,1,3]-benzothiadiazole (5A) within twisted and parallel structures, was used to illustrate the applications for this technique, that has been shown to be an innovative and versatile tool to correlate the photophysics with materials structure.

Keywords: ellipsometry, optical spectroscopy, Stokes parameters

1. Introduction

The understanding of light polarization from materials absorption, emission, and reflection can be addressed by matching one or more polarizers in the optical path of conventional photoluminescence and UV-vis spectrometers, called polarized photoluminescence and polarized absorbance, respectively [1–4]. These methodologies have been applied with the aim of acquiring information on the molecular arrangement (anisotropy and order factor) [3–6]. Besides that, Circular Dichroism spectroscopy has also been widely used to understand molecular organization based on their chirality [2, 6, 7]. Nevertheless, these techniques fail to identify all possible polarization states when applied separately. In the case of photoluminescence, for example, it is possible to get information from linear polarization states, but not from circular

ones. The polarized absorption, on the other hand, can elucidate the molecular order, but does not provide information on circular birefringence effects and Circular Dichroism. The last one consists in the difference between left and right circularly polarized light, thus resulting in the molecular asymmetry [6, 8, 9]. For instance, the study of energy transfer processes by means of the investigation of emitted polarized light can be very complicated when the polarized state is not completely described.

In this sense, Emission Ellipsometry (EE) is a technique that, combined with the Stokes theory, allows the complete description of the emitted light polarization states [6, 8, 9] being, in this manner, an excellent alternative in the study of energy transfer processes, mainly in polymeric materials [2, 5, 10, 11]. In addition, it is possible to obtain full information regarding molecular organization [2, 12], anisotropy [10], and asymmetry [13] factors in photoluminescent materials. All these studies and several applications in diverse materials lead to the development of a new method for Raman Optical Activity studies, named ellipsometric Raman spectroscopy (ERS) [14, 15]. In this new methodology, Basilio et al. [14] have been shown that EE combined with the Stokes theory can also be applied, not only for emitted but also for the scattered light. From this experiment, one can obtain meaningful information about materials optical activity even for easily photodegradable ones (both biological and polymeric) due to the limited exposition to exciting light.

This chapter aims a detailed review of Achromatic Ellipsometry from the appliance of Stokes theory on the determination of polarization parameters to its applications on materials studies.

2. Stokes theory

In the middle of the nineteenth century, the light polarization has had been mathematically characterized by Augustin Jean Fresnel (1788–1827) and Dominique François Arago (1786–1853), among others. Notwithstanding, the concept of partially polarized light was only formulated until the period around the year 1852, by Sir George Gabriel Stokes [12]. Fresnel and Arago used to describe polarized light in terms of its polarization ellipse. Such representation was incomplete, because it did not include partially polarized light. Stokes, on the other hand, solved the problem by demonstrating that it was possible to completely characterize any arbitrary polarization state from four experimental measurements (observables), in his work "On the Composition and Resolution of Streams of Polarized Light from Different Sources" [16]. Here and now, these observables are designated as Stokes parameters, which describe nonpolarized, partially, and complete polarized lights. Despite its fundamental contribution, his work was practically ignored by the scientific community for almost 100 years. In 1946, the Nobel laureate Subrahmanyan Chandrasekhar formulated the equations for radioactive transfer of partially polarized light [12], which was only possible due to Stokes' work. In addition to Stokes theory, new material developments for achromatic optical elements made possible the measuring of all polarization states as a function of wavelengths (optical spectrum), i.e., the necessary observables to enlighten the materials structure [2, 13, 14, 17, 18].

2.1. Polarization ellipse

Light description in terms of polarization ellipse, which is valid as long as the studied light is completely polarized, is very convenient. It allows the characterization of several states of light polarization using one equation [14, 18] and can result in forms interpreted as linearly and circularly polarized light. Beyond that, from the concept of polarization ellipse, it is possible to understand Stokes' description to identify all states of light polarization, including partially polarized beams [12]. In this sense, polarized light propagating along the z direction, and the electric field in two orthogonal components propagating along x and y directions can be represented by the following equations:

$$E_x(z, t) = E_{0x} \cos(\tau + \delta_x) \tag{1}$$

$$E_y(z, t) = E_{0y} \cos(\tau + \delta_y) \tag{2}$$

where E_{0x} and E_{0y} are the maximum amplitude, δ_x and δ_y are the phase constants at x and y axis respectively, and $\tau = \omega t - kz$ is the diffuser. From Eqs. (1) and (2), one can obtain the equation for an arbitrary instant of time, t:

$$\frac{E_x^2}{E_{0x}^2} + \frac{E_y^2}{E_{0y}^2} - 2\frac{E_x E_y}{E_{0x} E_{0y}} \cos\delta = \sin^2(\delta) \tag{3}$$

where $\delta = \delta_y - \delta_x$. Equation (3) is named polarization ellipse [12, 19]. The ellipse described by Eq. (3) has its a and b axis rotated by an angle Ψ relatively to the reference plan xy, as can be seen in **Figure 1**.

From the diagram above (**Figure 1**), it is possible to write the components E'_x and E'_y relatively to the components E_x and E_y and to the angle Ψ, in a way that:

$$E'_x = a\cos(\tau + \delta') \tag{4}$$

$$E'_y = \pm b\sin(\tau + \delta') \tag{5}$$

$$\frac{E'^2_x}{a^2} + \frac{E'^2_y}{b^2} = 1 \tag{6}$$

Equation (6) describes a standard ellipse, straight, where a and b are the major and minor axis, respectively [2, 12, 19]. It is important to note that, when the phase angle equals 90° and 270°, the angle Ψ will be zero. This condition is only reached when E_{0x} and E_{0y} are zero, that is, for linearly polarized light along vertical (y-axis) or horizontal (x-axis) directions. Another important parameter is defined as ellipticity (χ) [5, 12]:

$$\tan(\chi) = \pm\frac{a}{b} \tag{7}$$

In this case, if $a = b$, which means that the light is left or right circularly polarized or even random, then the ellipticity became zero.

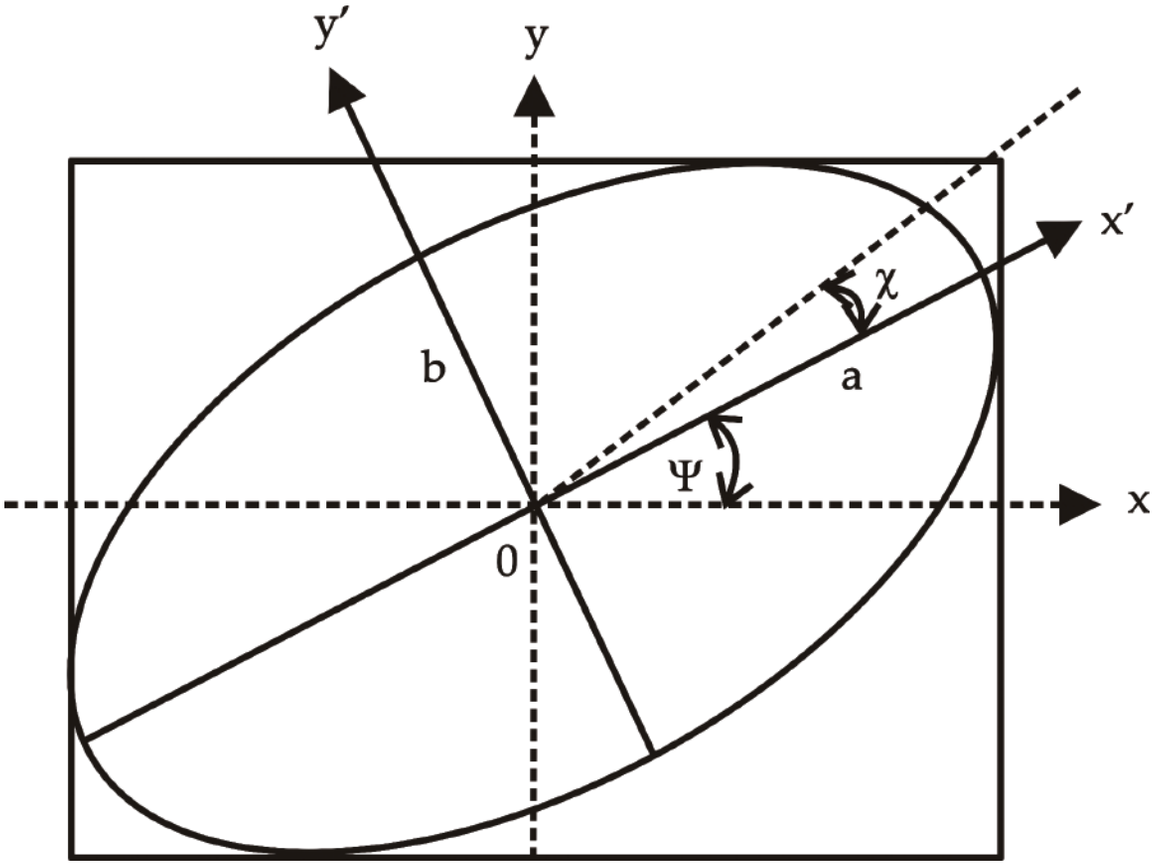

Figure 1. Polarization ellipse representation.

2.2. Stokes parameters

It is well known that the amplitude of the optical field cannot be observed [12, 15, 16, 19]. However, its intensity, derivative from the temporal average of square amplitude, can be observed. Therefore, one can obtain the polarization ellipse observables by taking the temporal average of nonobservables from the polarization ellipse. By doing that, it is possible to collect four parameters, the Stokes parameters [12, 16]. Consequently, Stokes parameters are a natural outcome of the wave theory of light, in a way that provide a complete description of any light polarization state [12]. More important, they are exactly the measured quantities.

Formerly, the Stokes parameters were used only for describing intensity measurements and polarization states of optical fields. Still, when these parameters are found in the form of column matrix (also known as Stokes vectors) they can lead to the study of spectroscopic observables [11–14, 17, 18]. Therein formalism, in Eq. (6), each term represents the temporal average, such as in Eq. (8) in its general form [19]:

$$\frac{E_x^2(t)}{E_{0x}^2} + \frac{E_y^2(t)}{E_{0y}^2} - 2\frac{E_x(t)E_y(t)}{E_{0x}E_{0y}}\cos\delta = \sin^2(\delta) \tag{8}$$

and the temporal average for each term is given by [12, 16]:

$$E_x^2(t) = \frac{1}{2}E_{0x}^2, \quad E_y^2(t) = \frac{1}{2}E_{0y}^2, \text{ and } E_x(t)E_y(t) = \frac{1}{2}E_{0x}E_{0y}\cos\delta \tag{9}$$

Combining the equations (8) and (9), one can extract the Stokes parameters[1] from the following equation:

$$(E_{0x}^2 + E_{0y}^2)^2 - (E_{0x}^2 - E_{0y}^2)^2 - (2E_{0x}E_{0y}\cos\delta)^2 = (2E_{0x}E_{0y}\sin\delta)^2 \tag{10}$$

arranged as follows:

$$\begin{aligned} S_0 &= E_{ox}^2 + E_{oy}^2 \\ S_1 &= E_{ox}^2 - E_{oy}^2 \\ S_2 &= 2E_{0x}E_{0y}\cos\delta \\ S_3 &= 2E_{0x}E_{0y}\sin\delta \end{aligned} \tag{11}$$

Using the parameters above, Eq. (10) can be rewritten in terms of complete polarized light:

$$S_0^2 = S_1^2 + S_2^2 + S_3^2 \tag{12}$$

The Stokes parameters, resulted from the definitions in Eq. (11), are real quantities expressed in terms of intensity. More than that, they are the observables from the polarization ellipse and, therefore, they represent the optical field.

The first parameter, S_0, represents the total light intensity. The following parameters describe the differences between: (i) horizontal or vertical linear polarization – S_1, (ii) linear polarization at $\pm$ 45° – S_2, and (iii) left or right circular polarization – S_3. For partially polarized light, using the Cauchy-Schwarz Inequality [12, 16], Eq. (12) can be rewritten as follows:

$$S_0^2 \geq S_1^2 + S_2^2 + S_3^2 \tag{13}$$

where equality applies for completely polarized light and inequality for nonpolarized or partially polarized light. Since the Stokes parameters directly reflect the observables, one can represent the rotation angle (Ψ) and the ellipticity (χ) using Eqs. (11) – (13) as:

$$\tan(2\Psi) = \frac{S_2}{S_1} \tag{14}$$

$$\sin(2\chi) = \frac{S_3}{S_0} \tag{15}$$

Finally, the degree of polarization (P) can be described using the Stokes parameters for any polarization state [2, 12, 19]:

[1]Stokes parameters can also be obtained by means of plane waves. This solution can be found at Refs. [12, 16, 19].

$$P = \frac{I_{pol}}{I_{tot}} = \frac{(S_1^2 + S_2^2 + S_3^2)^{\frac{1}{2}}}{S_0} \tag{16}$$

where I_{pol} means intensity of the sum of polarized components and I_{tot} is the total intensity of the light beam. The value $P = 1$ corresponds to completely polarized light, whereas $P = 0$ corresponds to nonpolarized and $0 < P < 1$ to partially polarized light.

2.3. How to measure Stokes parameters

As described in earlier sections, the Stokes parameters are real observables. To measure them, it is necessary at least two optical components with which the light must interact to be analyzed successfully. Generally, these elements are polarizers and quarter-wave plates that can be set up in several ways in order to acquire the Stokes parameters. These optical components can be mathematically represented as a Muller matrix [2, 12], and, from the mathematic relations, the Stokes parameters can be obtained (see Eq. (18)).

There are several available methods to get the Stokes parameters. Collet describes diverse optical configurations and measurement modes to calculate them [12]. Although, one must be careful with systematic errors, alignment and intensity corrections that can be introduced in the system depending on the chosen experimental assembly, mainly on those which the exchange of optical elements during the experiment is required. One way to avoid this problem is to keep the optical elements fixed, reducing a significant amount of errors from alignment and problems from light intensity corrections due to reflections or absorptions. This is the main proposal of this chapter: keeping the optical elements fixed, the observables will be decomposed by Fourier series. This method also provides the advantage of using achromatic optical elements that work in a broad spectral range, especially at visible spectrum.

The representation of light polarization states as Stokes parameters in the form of column matrix (Stokes vector) can be seen below:

$$S = \begin{pmatrix} S_0 \\ S_1 \\ S_2 \\ S_3 \end{pmatrix} \tag{17}$$

In this matrix formalism, the effects on the light polarization from any beam due to optical components can be mathematically represented also by matrix, in this case, the Muller matrix [12, 14]. Concerning the fixed optical components, the analysis method via Fourier series employs a quarter-wave plate and a fixed linear polarizer, as can be seen in **Figure 2**.

From the arrangement shown in **Figure 2**, it is possible to correlate the intensity of emerging field (E'_x and E'_y) with the Stokes parameters from incident field (E_x and E_y) through Eqs. (5), (14), and (16):

$$I(\theta) = \frac{1}{2}[A + B.\sin(2\theta) + C.\cos(4\theta) + D.\sin(4\theta)] \tag{18}$$

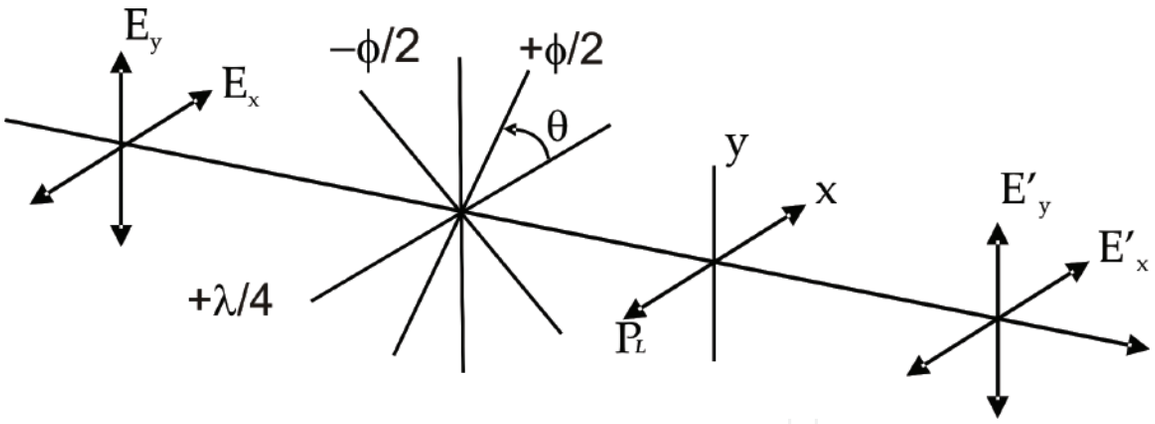

Figure 2. Diagram of an electromagnetic wave propagating through a quarter-wave plate, rotated by an angle θ, and a linear polarizer P_L (horizontal) for the measurement of Stokes Parameters.

where for a polarizer with transmission axis along the horizontal direction (x-axis): $A = S_0 + \frac{S_1}{2}$, $B = -S_3$, $C = \frac{S_1}{2}$, and $D = \frac{S_2}{2}$; or a polarizer with transmission axis along the vertical direction (y-axis): $A = S_0 - \frac{S_1}{2}$, $B = S_3$, $C = \frac{-S_1}{2}$, and $D = \frac{-S_2}{2}$.

Eq. (18) is a truncated Fourier series, with a constant term A, a term with double frequency (B), and two more terms with quadruple frequencies (C and D). As a Fourier series, this equation admits only one solution for parameters A, B, C, and D; thus resulting in a very precise way to obtain Stokes parameters. It is also likely to obtain the polarization degree (P) for the emerging light, from Eq. (18). In addition, Alliprandini-Filho [2], describes the asymmetry factor (g) and Circular Dichroism acquired from Stokes parameters, providing more complex information about the chirality of the molecules that compose the studied material. One can see that the technique described here is a powerful tool in the understanding of material conformations and structure.

2.3.1. Anisotropy

Similarly to the new approach as presented at previous sections, Therézio et al. [10] outlined a new method to determine anisotropy using Stokes parameters. In this methodology, the Stokes parameters are firstly rewritten as a function of electric field intensities, as described in Eq. (18). Then, the y component is considered in the same direction as the laboratory frame of reference, and x in the horizontal direction at the same reference. Besides, $E_{ox}^2 = I_{0x}$ and $E_{oy}^2 = I_{0y}$, where I_{0i} is the beam intensity at i direction. Then, considering that a sample is excited by a beam at y direction is possible to obtain $E_{ox}^2 = I_{\parallel,\perp}$ and $E_{oy}^2 = I_{\parallel,\parallel}$, where $I_{\parallel,\perp}$ refers to the emission at perpendicular direction ($\perp$) due to parallel excitation ($\parallel$). Hence, the first and second equations from Eq. (11) set can be expressed as:

$$\begin{cases} S_0 = I_{\parallel,\perp} + I_{\parallel,\parallel} \\ S_1 = I_{\parallel,\perp} - I_{\parallel,\parallel} \end{cases} \tag{19}$$

From the conventional equation that determines the anisotropy factor, r [1, 10]:

$$r = \frac{I_{\parallel,\parallel} - I_{\parallel,\perp}}{I_{\parallel,\parallel} + 2I_{\parallel,\perp}}. \tag{20}$$

combined with Eq. (11), the anisotropy factor as a function of Stokes parameters is given by:

$$r = \frac{-2\frac{S_1}{S_0}}{3 + \frac{S_1}{S_0}}. \tag{21}$$

Perhaps the most advantage of Eq. (21), besides the obvious application as efficient technique for the studies of photophysical properties of luminescent materials, is the useless of corrections related to optical components, such as diffraction grade and slits when compared with the traditional methods as the one described by Eq. (20).

2.3.2. Anisotropy and Circular Dichroism

Despite the fact that Therézio et al. [13] had originally described this methodology for the study and characterization of a cholesteric liquid crystal, the dissymmetry and Circular Dichroism can be measured and studied with this method for any material of interest, since the material presents the measurable physical characteristics, as symmetry, for example.

Here the asymmetry factor, g, is defined by:

$$g = -2\frac{I^R - I^L}{I^R + I^L} \tag{22}$$

where I^R and I^L are the light intensities with excitation from right (R) and left (L) circularly polarized light. It is also related to parameter Δ, the difference between the two circularized lights, and is expressed by:

$$\Delta = \frac{-g}{2} \tag{23}$$

The asymmetry factor becomes a Circular Dichroism measurement when the absorption of linearly polarized light across a sample is analyzed.

In the formulation presented here, g can be determined from Stokes parameters. It can be noticed, in Eq. (19), that the Stokes parameter S_3 represents the difference $I^R - I^L$ and S_0 the sum of intensities $I^R + I^L$. As the linearly polarized light can be decomposed into the sum of two circularly polarized light beams (left and right), the Stokes parameters S_3 and S_0 can be directly related to g parameter [13] by the following equation:

$$g = 2\frac{S_3}{S_0} \tag{24}$$

2.3.3. Ellipsometric Raman Spectroscopy

The Raman Optical Activity (ROA) has been provided numerous information about chiral molecules conformation. Those molecules have fundamental relevance in many areas of

knowledge including Biology and Medicine. Basilio et al. [14] present details of a new technique to measure the Raman of chiral carbon: the ellipsometric Raman spectroscopy (ERS). The technique ERS quantifies the vibrational optical activity through measurement of small differences in intensity of Raman scattering for chiral molecules, when the impinging light is right and left circularly polarized. In other words, ERS is the application of Achromatic Ellipsometry to measure the Raman scattering. That is for say, through the technique of Ellipsometry one can measure the Stokes parameters, thus describing the complete light polarization states. The exciting light in ERS is a laser source which can be decomposed into two circular polarizations: right and left. Similarly to ROA experiments, the parameter S_3 describes the amount of light when normalized. ESR technique was validated by the successful characterization of the chiral alcohol (*S*)-(−)-1-phenylethanol (1-PhEtOH).

3. Applications

In this section, applications of Achromatic Ellipsometry will be briefly presented: the utilization of Emission Ellipsometry for studying a luminescent dye into a nematic liquid crystal. In this example, the importance of using the right optical elements will be noticed.

3.1. Nematic Liquid Crystal E7™ doped with a benzothiadiazole derivative dye

Samples were prepared using nematic liquid crystal E7™. Basically, it consists of a mixture of LC 5CB (47%), 7CB (25%), 8OCB (18%), and 5CT (10%), doped with a luminescent dye 4,7-bis {2-[4-(4-decylpiperazin-1-yl) phenyl]ethynyl}-[2,1,3]-benzothiadiazole (5A) at 0.025% of molar concentration [20]. Cells were prepared by superimposing two BK7 glass substrates coated with Poly(vinyl alcohol) (PVA) films separated by 20 mm thick Mylar spacers. The PVA films were previously rubbed with soft velvet to induce a specific aligning direction to the liquid crystal molecules. In this work, three different configurations were investigated considering the aligning direction induced in each glass plate of the cell: S00, S45 and S90 represent the rotation angles between the two substrates of the cells at 0° (parallel configuration), 45° and 90° (twisted), respectively. The alignment direction 0° was determined to be parallel with the vertical direction of lab reference. The scheme of the cells is presented in **Figure 3**.

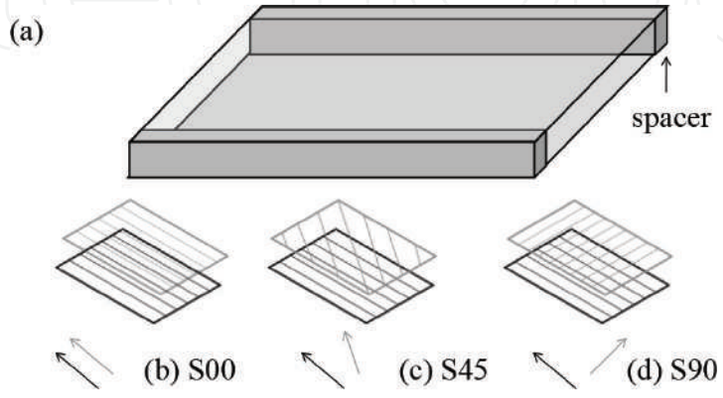

Figure 3. (a) Scheme of the liquid crystal cell. Rows indicate the alignment direction of each substrate of the cells (b) S00 – parallel axis (0°), (c) S45 – axis rotated in 45° and (d) S90 – perpendicular axis (90°).

Optical absorption (OA) measurements in UV-Vis-NIR were made in a FEMT O 800XI spectrometer. In the measurements of polarized optical absorption (POA), calcite polarizer Mugta10™ was inserted in the optical pathway of incident light, generating linear horizontally polarized light (LHP) and vertically polarized light (LVP). Photoluminescence measurements were made with an incident light of argon laser from Spectra Physics Inc. Stabilite 2017, with excitation wavelength at 457 nm. The emitted light from the sample was collimated by a set of lenses and detected by the Ocean Optics USB 2000 spectrometer. PL measurements were made on the two faces of the samples and the light was recorded on the same face.

Samples also followed EE and TE measurements. For the TE measurements, polarized light was analyzed by the Fourier series decomposition. The incident light was polarized vertically, right and left circularly. In the experimental set up, in the optical way of the transmitted light, an achromatic quarter-wave retarder was used, and a fixed calcite polarizer was placed before the spectrometer. In this case, a power meter of the OPHIR laser measurement group was used as a detector. The argon laser from Spectra Physics Inc. Stabilite 2017 at 457 nm and the He-Ne laser at 633 nm were used as light source. In this experiment, the quarter-wave retarder rotates around the propagation axis of transmitted light from 0 to 360° in steps of 10°.

Figure 4a presents absorbance and PL spectra normalized at maximum intensity of S00, S45 and S90 samples. Optical properties of the 5A dye did not change the electronics-vibrational transitions $\pi \rightarrow \pi^*$ e $\pi^* \rightarrow \pi$ significantly due to guest-host interaction in different cell configurations. The PL measurements were also performed with the wavelength excitation at 488 and 514 nm, and the emission did not show changes in the line shape or in the band position. In **Figure 4b–d**, polarized absorption spectrum, parallel, and perpendicular polarization are presented for S00, S45, and S90 samples, respectively. With these measurements, it was possible to observe that the 5A dye molecules are oriented in the same direction of the liquid crystal [21, 22]. An important fact is that S45 and S90 samples did not present the same line shape for the polarized absorption optical spectrum when the light interacted firstly in the different faces of samples. This clearly shows an asymmetry in the molecular ordering along the optical way, induced by liquid crystal molecular alignment, the exception in this case being the S00 sample. As a result, there are changes in the light polarization transmitted by this type of system [23].

Table 1 shows S_1, S_2 and S_3 parameters normalized by S_0 obtained during EE measurements and its polarizations. In general, data of **Table 1** show that the change in the excitation wavelength does not change either the Stokes parameter and the degree polarization for each sample dramatically, mainly at 457 and 488 nm, due to absorption intensity (**Figure 4a**) is very close ($A_{457nm}/A_{514nm} = 0.91$). This means that the average orientation of molecules closer to the surface is what contributes the most to the emission. In the S00 sample, the emitted light is LPV due to the high value of S_1 with a negative signal. This is due to molecular alignment at 0° direction (or parallel to the y axis), and consequently, the LPV light is emitted. The high value of S_2 module shows that molecules are not fully oriented to the vertical direction. For this reason, a linear +45° polarized light is observed. This type of polarization does not change significantly in relation to the wavelength and polarization of excitation source. This result is corroborated by the different value of zero in the OA for perpendicular direction as shown in

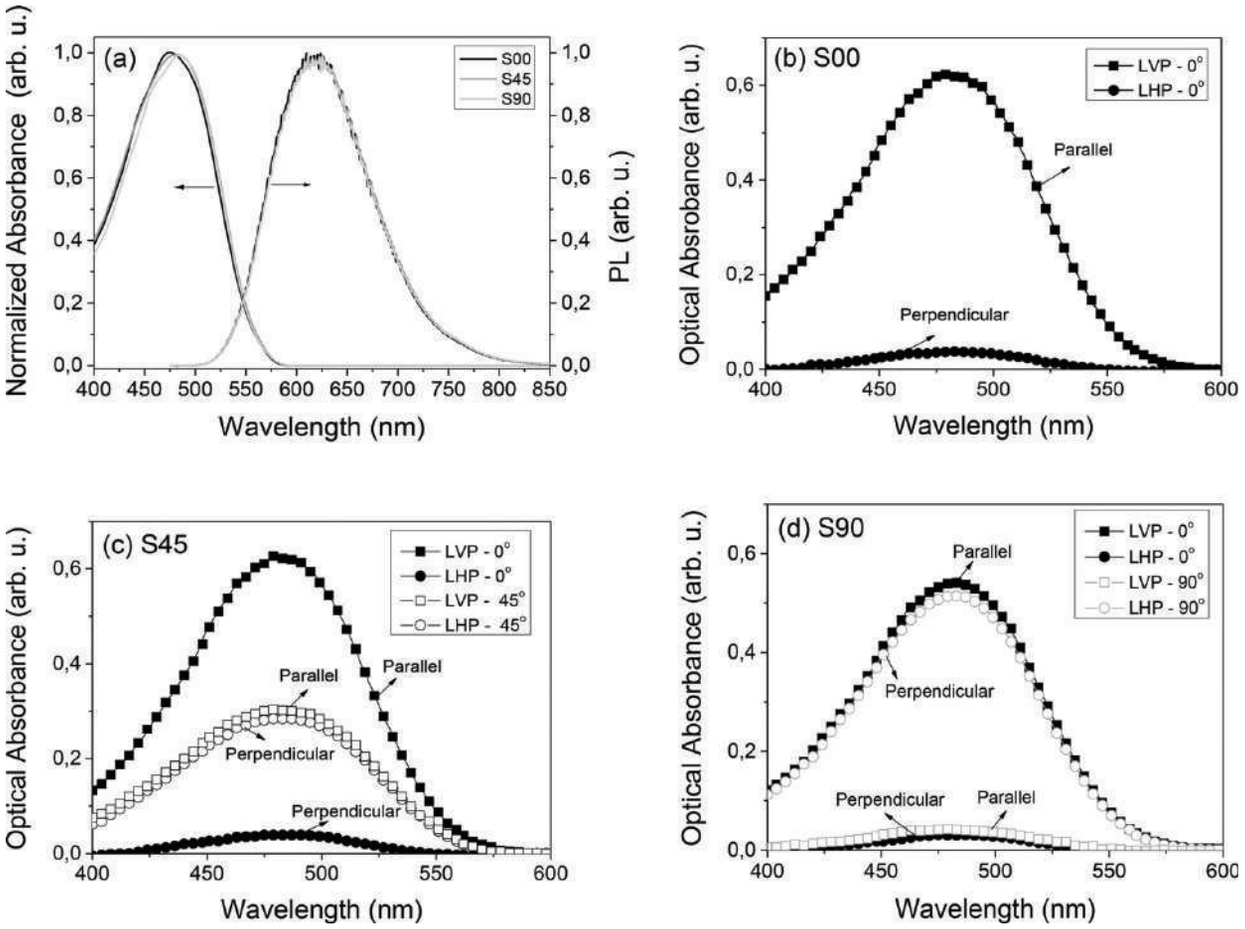

Figure 4. (a) OA and PL (excitation light at 457 nm) spectrums of S00, S45, and S90 samples. POA in parallel (vertical) and perpendicular (horizontal) direction of S00 (b), S45(c), and S90 samples (d). The direction at 0° of PVA films is considered parallel in relation to the vertical direction of laboratory.

Figure 3b. For the S45 sample, it can be seen by the S_1 value that on the face of 0° alignment, the light emitted is mostly linear vertically polarized as in the S00 sample. However, for the face with 45° alignment, this parameter decreases significantly. On the other hand, that face presents a significant increase in the S_2 parameter, which shows the emission of polarized light linear at 45° caused by the molecular ordering at 45°. Still for the S45 sample, the change in the wavelength and polarization of the excitation source does not cause a significant change in the Stokes parameter. Therefore, the emitted light remains with the same type of polarization. For the S90 sample, the light interacts first in the face with 0° alignment, independently of polarization and wavelength of excitation source, the emitted light is LVP as in the other samples. However, in the face with 90° alignment, the sample exhibits the emission of LHP light because the signal of S_1 is positive. This was expected due to molecules that, on this face, are horizontally oriented in relation to referential. An important point is that in the face with 0° alignment, this sample does not show linear polarized light at 45°, whereas on the face with 90° alignment, the emitted light presents a percentage of linear 45° polarized light. For the same face, when the wavelength of excitation source is at 514 nm, there is emission of circularly polarized light. This shows that molecules are rotating inside the liquid crystal cell and the emission of

			S_1/S_0	S_2/S_0	S_3/S_0	P	r
Sample S00							
λ_{exc} = 457 nm	RCP	Face 00°	−0.67	−0.33	0.09	0.75	0.58
	LVP	Face 00°	−0.74	−0.41	0.09	0.86	0.65
λ_{exc} = 488 nm	RCP	Face 00°	−0.55	−0.33	0.07	0.68	0.45
	LVP	Face 00°	−0.64	−0.35	0.09	0.73	0.54
λ_{exc} = 514 nm	RCP	Face 00°	−0.47	−0.47	0.05	0.67	0.37
	LVP	Face 00°	−0.52	−0.40	0.10	0.67	0.41
Sample S45							
λexc = 457 nm	RCP	Face 00°	−0.85	−0.11	0.03	0.86	0.79
		Face 45°	−0.25	0.73	0.02	0.78	0.18
	LVP	Face 00°	−0.84	−0.10	0.05	0.85	0.77
		Face 45°	−0.25	0.76	0.04	0.81	0.18
λexc = 488 nm	RCP	Face 00°	−0.86	−0.12	0.04	0.87	0.80
		Face 45°	−0.31	0.87	0.03	0.92	0.23
	LVP	Face 00°	−0.87	−0.12	0.03	0.88	0.81
		Face 45°	−0.32	0.86	0.03	0.92	0.23
λexc = 514 nm	RCP	Face 00°	−0.80	−0.16	0.03	0.81	0.73
		Face 45°	−0.34	0.83	0.02	0.90	0.26
	LVP	Face 00°	−0.85	−0.18	0.13	0.88	0.79
		Face 45°	−0.32	0.82	0.02	0.89	0.23
Sample S90							
λexc = 457 nm	RCP	Face 00°	−0.79	0.03	−0.06	0.79	0.71
		Face 90°	0.80	0.20	−0.05	0.82	−0.42
	LVP	Face 00°	−0.74	0.06	0.03	0.74	0.65
		Face 90°	0.53	0.16	−0.04	0.55	−0.30
λexc = 488 nm	RCP	Face 00°	−0.80	0.03	0.02	0.80	0.73
		Face 90°	0.74	0.16	−0.07	0.76	−0.40
	LVP	Face 00°	−0.85	0.03	0.00	0.86	0.79
		Face 90°	0.58	0.11	−0.10	0.60	−0.32
λexc = 514 nm	RCP	Face 00°	−0.85	−0.04	0.12	0.86	0.79
		Face 90°	0.78	0.20	−0.12	0.81	−0.41
	LVP	Face 00°	−0.81	−0.03	0.01	0.81	0.73
		Face 90°	0.56	0.12	−0.11	0.59	−0.31

Table 1. Normalized Stokes parameter and polarization degree of S00, S45, and S90 samples.

http://dx.doi.org/10.5772/intechopen.70089

LHP light occurs by molecules that are preferably oriented in the horizontal direction (**Figure 2d**), but have components in the vertical direction. For this reason, there is linear horizontally polarized emitted light even when the excitation source is LVP. The circularly polarized light can be easily observed when the excitation wavelength is at 514 nm. This happens because the length of penetration in the sample for this wavelength is higher ($A_{457nm}/A_{514nm} = 1.29$) than the other wavelengths.

Figure 5 shows two EE measurements performed in the S45 sample using the excitation light at 488 nm and LVP. By the fitting of EE data and using Eq. (18), Stokes parameters of samples' emitted light in function of the different excitation wavelengths and the type of the light polarization could be obtained. These measurements were performed on the two faces of the cell. Thereby, the molecular orientation within the liquid crystal cell by the emission of the dyes could be seen.

In order to verify the transmitted light properties, TE measurements were made at two wavelengths: 457 and 633 nm. Optical absorption of the 5A dye is present at 457 nm. For 633 nm changes in the polarization of transmitted light are caused only by the refractive index of the system, as there is not absorption. **Figure 6** shows two TSE measurements of the S45 and S90 samples.

By TE measurements, Stokes parameters were obtained and the polarization state of transmitted light was described. **Table 2** shows the Stokes parameters and the polarization degree of samples' transmitted light.

The first important point to discuss in these results is the polarization values higher than one. This occurs in three measures and it is due to the measurements' error that is around 5%. However, these values are not higher than recommended. From TE measurements, it could be seen that samples change the polarization of transmitted light and that this variation occurs even when the wavelength is not in the OA spectrum range of 5A dye. This is due to system birefringence [23]. Based on **Table 2**, it is clear that for the S00 sample, when the incident light

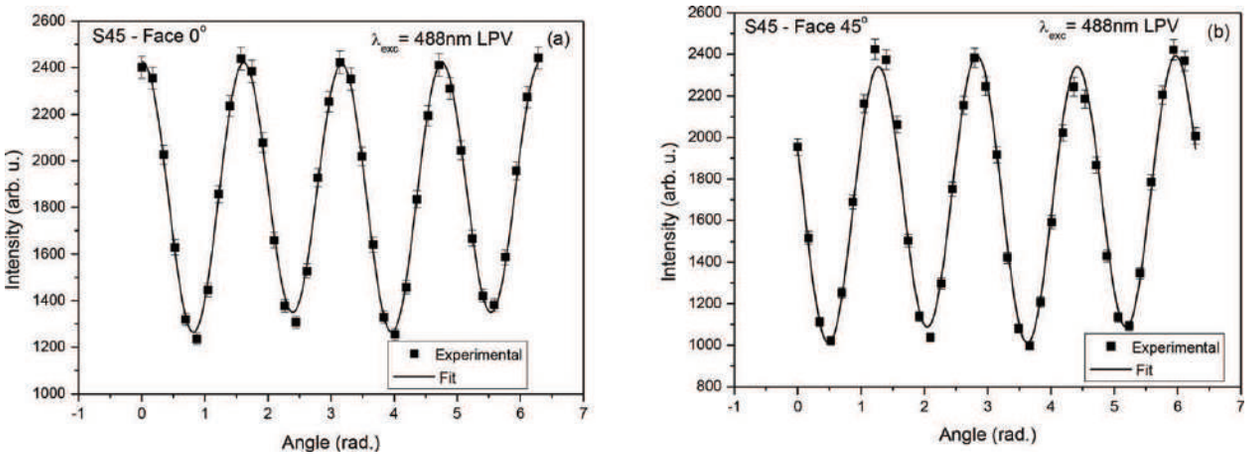

Figure 5. EE Measurement made in the S45 sample at face 0° (a) and 45° (b).

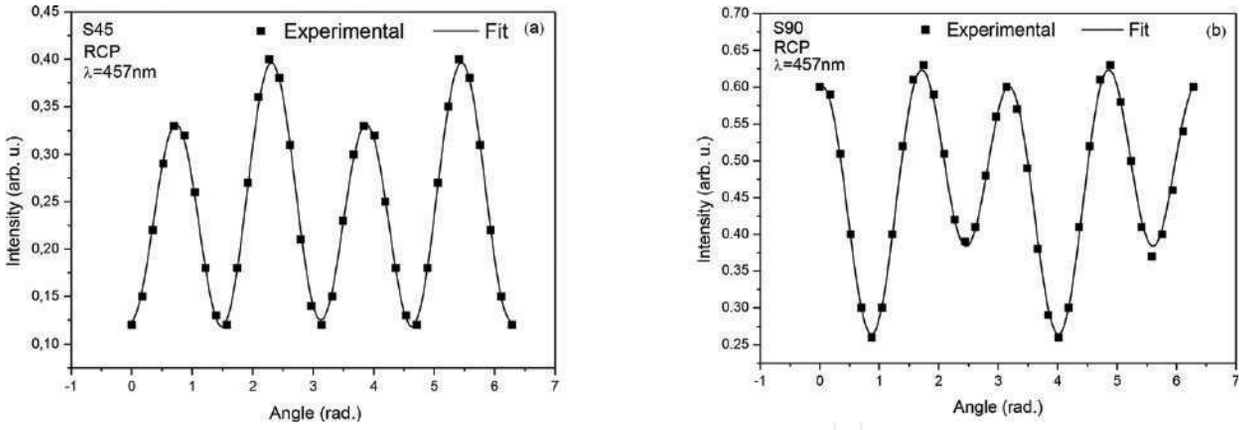

Figure 6. (a) Transmittance Ellipsometry measurements of the S45 sample, the light interacting firstly in the face with molecules oriented at 45° and the source at 457 nm is right circularly polarized. (b) Transmittance Ellipsometry measurements of the S90 sample, the light interacting firstly in the face with molecules oriented at 0° and the source at 457 nm is right circularly polarized.

is at 457 nm and right circularly polarized, the transmitted light is linear horizontally polarized due to the high value of S_1 with positive signal. There is also a significant amount of linear +45° polarization because of the value of S_2 and a small percentage of light is left circularly polarized. It is important to observe that the incident light is right circularly polarized, and the S00 sample changes the type of polarization of transmitted light for the small percentage of left circular polarization. In case of the incident light is left circularly polarized, the transmitted light through the sample is linear +45° polarized by the high value of S_2. There is also an amount of the linear horizontally polarized light due to the value of S_1, the transmitted light presents a small percentage of right circular polarization. When the incident light is linear vertically polarized, the transmitted light is linear vertically polarized by the S_1 value, and there is a small part of transmitted light that is right circularly polarized. Therefore, in this case, there are practically no changes in the polarization of incident light. Still for the S00 sample, when the incident light is right circularly polarized and the wavelength at 633 nm, the transmitted light changes its polarization for the linear −45°. There is a small percentage of light that is linear horizontally and right circularly polarized. For the measurement performed with the left circularly polarized incident light, a similar behavior of that when the incident light is right circularly polarized was shown. However, the transmitted light is linear +45° polarized, which is the majority of transmitted light polarization. When the incident light is linear vertically polarized, the sample does not change the polarization of transmitted light, which occurs in the same way when the wavelength is at 457nm and there is not optical absorption of dyes.

For the S45 sample, the same measurements as those of the S00 were obtained. However, in this sample, the incidence of light was carried out in the two faces of the sample, and it allows the verification of whether the polarization of transmitted light changes with molecular ordering. When the incident light has right circular polarization and wavelength at 457 nm, it can be observed that when the light interacts first in the face with 0° alignment, the transmitted light is linear +45° polarized, and a part of light is linear horizontally polarized, which should be

			S_1/S_0	S_2/S_0	S_3/S_0	P
Sample S00						
λ = 457 nm	RCP	Face 00°	0.62	0.36	−0.16	0.74
	LCP	Face 00°	0.44	−0.82	0.20	0.95
	LVP	Face 00°	−1.00	0.03	0.13	1.01
λ = 633 nm	RCP	Face 00°	0.11	−0.79	0.09	0.80
	LCP	Face 00°	−0.08	0.79	0.06	0.80
	LVP	Face 00°	−0.95	0.06	−0.03	0.95
Sample S45						
λ =457 nm	RCP	Face 00°	0.19	0.53	0.02	0.56
		Face 45°	0.66	−0.13	0.08	0.68
	LCP	Face 00°	0.05	0.63	0.03	0.63
		Face 45°	0.69	−0.02	0.08	0.69
	LVP	Face 00°	−0.38	−0.93	0.00	1.01
		Face 45°	0.48	−0.12	−0.03	0.50
λ = 633 nm	RCP	Face 00°	0.57	0.04	0.11	0.59
		Face 45°	0.30	−0.52	0.03	0.60
	LCP	Face 00°	−0.22	0.03	0.45	0.50
		Face 45°	0.22	0.11	0.55	0.61
	LVP	Face 00°	−0.35	−0.97	0.00	1.04
		Face 45°	−0.02	−0.27	−0.14	0.30
Sample S90						
λ = 457 nm	RCP	Face 00°	−0.82	−0.32	0.18	0.90
		Face 90°	0.56	0.52	−0.15	0.78
	LCP	Face 00°	−0.53	0.37	−0.52	0.84
		Face 90°	0.63	−0.39	0.42	0.85
	LVP	Face 00°	0.94	−0.14	0.17	0.97
		Face 90°	0.98	−0.02	−0.01	0.98
λ = 633 nm	RCP	Face 00°	−0.02	0.84	0.05	0.84
		Face 90°	0.44	−0.67	0.23	0.84
	LCP	Face 00°	−0.37	−0.68	−0.42	0.88
		Face 90°	0.24	0.80	0.00	0.84
	LVP	Face 00°	0.87	−0.42	−0.25	1.00
		Face 90°	0.98	−0.12	−0.07	0.99

Table 2. Stokes parameters and the polarization degree of S00, S45, and S90 samples.

noticed for the S_1 value. This value increases significantly when the incidence occurs in the other face. On the other hand, the amount of linear at 45° polarized light decreases and changes the signal for negative. When the incident light is left circularly polarized, the transmitted light through the sample has the same state of that when the incidence occurs with the right circularly polarized light. However, the smallest part of polarized light (S_1 for the face at 0° and S_2 for the face at 45°) becomes practically zero. When the incident light is linear vertically polarized and the light interacts firstly with the face with 0° alignment, the polarization of transmitted light was changed to linear −45° polarization, there is still a small percentage of linear vertically polarized light. When the incidence occurs firstly in the face with 45° alignment, the transmitted light has linear horizontal polarization. However, the value of linear 45° polarized light that in the other face (0° alignment) is very high, decreases significantly. Measurements were made with the wavelength at 633 nm, and in this case, there is not OA of dye. The incident light is right circularly polarized and interacting first in the face with 0° alignment, the transmitted light has the linear horizontal polarization, and a small part of light is right circularly polarized. Nevertheless, when the light interacts first in the face with 45° alignment, the transmitted light is linear −45° polarized, there is still a part of the transmitted light that has the linear horizontal polarization. When the incident light is left circularly polarized and interacts first in the face with 0° alignment, the transmitted light has right circular polarization. There is still a part of the transmitted light that is linear vertically polarized. In the case of light interacting firstly with the other face (45° alignment), it can be verified that the majority of transmitted light is right circularly polarized, There is still a significant part of linear horizontally polarized light and a small part of linear +45° polarized light. When the incident light is linear vertically polarized, it can be observed that when the light interacts initially with the face with 0° alignment, the greater part of transmitted light has linear +45° polarization. There is also a percentage of linear vertically polarized light for the measurement performed when the light interacts first in the other face (45° alignment) of the sample. The transmitted light has very little polarization and the main polarization is linear −45°.

In the S90 sample, measurements were made in the same way as those of the S45 sample. For the incident light with wavelength at 457 nm and the right circular polarization, it can be seen that when the light interacts firstly with the face with 0° alignment, the transmitted light is linear vertically polarized. There is still a part of the light that is linear −45° polarized and a small part that is right circularly polarized. When the incident light interacts initially with the other face (90° alignment), the transmitted light has linear horizontal polarization, linear +45°, and a small part of light is left circularly polarized. When the incident light has left circular polarization, it could be verified that when the light interacts first in the face with 0° alignment, the transmitted light has a significant value of linear vertically and left circularly polarized light. There is also a small amount of linear +45° polarized light. When the light interacts initially with the other face (90° alignment), the transmitted light changes the signal of Stokes parameters in relation to the face with 0° alignment. Moreover, the transmitted light has linear horizontal polarization and it also has right circular polarization and a small percentage of linear −45° polarized light. When the incident light has linear vertical polarization, the transmitted light is practically linear horizontally polarized. There is only a small part of linear −45°

and right circularly polarized light when the incidence is performed firstly in the face with 0° alignment.

Like the other samples, measurements in the S90 were also made with the wavelength at 633 nm. When the incident light has right circular polarization, if the incident light interacts firstly in the face with 0° alignment, the transmitted light is linear +45° polarized. If the incidence occurs firstly in the other face (90° alignment), the transmitted light is mainly linear +45° polarized, in this case there is still a small amount of linear horizontal polarization and right circular polarization. When the incident light has left circular polarization, what happens is a similar process when the incident light is right circularly polarized? However, there is an inversion of the main polarization state of light between the face with 0° and 90° alignment. Measurement was also made with the incidence of linear vertically polarized light. For the two faces, the transmitted light is linear horizontally polarized. Therefore, the transmitted light changes completely its type of polarization. It is possible to observe that when the incident light interacts initially in the face with 0° alignment, the transmitted light has a percentage of linear −45° and left circularly polarized light. For the incidence performed in the other face (90° alignment) a percentage of this polarization state for the transmitted light is much smaller in relation to the incidence achieved firstly in the face with 0° alignment.

With EE and TE measurements, a complete molecular ordering inside the doped liquid crystal cell could be verified. It is important to observe that the EE measurements, in general, allow characterization of the molecular ordering onto the substrate surface. It can be changed by the excitation wavelength and molecules along the cell. With TE measurements, results allow the presence of an effect that occurs in the molecular ordering along of the doped liquid crystal cell. This can be related to the birefringence of system only when the light is transmitted by the sample and there is no optical absorption of 5A dye, or it can be related to the optical absorption and the birefringence simultaneously.

4. Conclusion

In this work, we illustrated a new methodology for measuring Raman Optical Activity [14] and the application of achromatic Ellipsometry in the study of benzotiadiazol derivative dye doped in the E7 nematic liquid crystal. Emission and transmittance Ellipsometry experiments were used to verify its molecular ordering within a liquid crystal cell. The obtained results showed that chromophores were ordered in the same direction of the E7 molecules. In addition, due to the change in the excitation wavelength, penetration depth in the sample could be verified, enabling the analysis of molecules ordering within a liquid crystal cell. Ellipsometry experiments also indicate that the molecular orientation inside the cells somehow changes the polarization of transmitted light. This effect can be due to system birefringence (both liquid crystal and dye) or due to combined process between dyes optical absorption and system birefringence. It is important to emphasize that changes in light polarization occur differently for one process (birefringence) or two processes simultaneously (birefringence and optical absorption). Finally, achromatic Ellipsometry was demonstrated to be a complete spectroscopic technique that enables the analysis of bulk and interfacial molecular ordering.

Acknowledgements

The authors are grateful to the following Brazilian Agencies: FAPEMAT, FAPEMIG, CNPQ, INCT/INEO, and INCT/INFo. The authors are grateful to Heidi C. Piva for helping with grammar corrections.

Author details

Eralci Moreira Therézio[1]*, Gustavo G. Dalkiranis[2], André A. Vieira[3], Hugo Gallardo[4], Ivan H. Bechtold[5], Patricia Targon Campana[6] and Alexandre Marletta[7]

*Address all correspondence to: therezio@ufmt.br

1 Institute of Exact and Natural Sciences, Federal University of Mato Grosso, Rondonópolis, Brazil

2 Physics Department, Universitat Autònoma de Barcelona, Bellaterra, Spain

3 Chemistry Institute, Federal University of Bahia, Salvador, Brazil

4 Chemistry Department, Federal University of Santa Catarina, Florianópolis, Brazil

5 Physics Department, Federal University of Santa Catarina, Florianópolis, Brazil

6 School of Arts, Sciences and Humanities, University of São Paulo, São Paulo, Brazil

7 Physics Institute, Federal University of Uberlândia, Uberlândia, Brazil

References

[1] Marletta A. Optical Properties of Organic Semiconductors Based on Light Emitting Polymers. São Carlos: Universidade de São Paulo; 2001

[2] Alliprandini-Filho P. Emission Ellipsometry Technique Application for Luminescent Materials Characterization. Uberlândia: Universidade Federal de Uberlândia; 2012

[3] Valeur B. Molecular Fluorescence: Principles and Applications. Weinheim: Wiley-VCH; 2001

[4] Kaito A, Nakayama K, Kanetsuna H. Infrared dichroism and visible-ultraviolet dichroism studies on roller-drawn polypropylene and polyethylene sheets. Journal of Macromolecular Science, Part B. 1987;**26**(3):281–306

[5] Alliprandini-Filho P, da Silva GB, Barbosa Neto NM, Silva RA, Marletta A. Induced secondary structure in nanostructured films of poly(p-phenylene vinylene). Journal of Nanoscience and Nanotechnology. 2009;**9**:5981–5989

[6] Berova N, Nakanishi K, Woody RW. Circular Dichroism: Principles and Applications. New York: Wiley-VCH; 1994

[7] Lin SH. Band shape of the circular dichroism. The Journal of Chemical Physics. 1971;**55** (7):3546–3554

[8] Shirvani-Mahdavi H, Mohajerani E, Wu S-T. Circularly polarized high-efficiency cholesteric liquid crystal lasers with a tunable nematic phase retarder. Optics Express. 2009;**18** (5):5021–5027

[9] Oda M, Nothofer HG, Lieser G, Scherf U, Meskers SCJ, Neher D. Circularly polarized electroluminescence from liquid-crystalline chiral polyfluorenes. Advanced Materials. 2000;**12**(5):362–365

[10] Therézio EM, Piovesan E, Vega ML, Silva RA, Oliveira ON, Marletta A. Thickness and annealing temperature effects on the optical properties and surface morphology of layer-by-layer poly(p-phenyline vinylene)+dodecylbenzenesulfonate films. Journal of Polymer Science Part B: Polymer Physics. 2011;**49**(3):206–213

[11] Alliprandini-Filho P, da Silva RA, Barbosa Neto NM, Marletta A. Partially polarized fluorescence emitted by MEHPPV in solution. Chemical Physics Letters. 2009;**469**(1-3):94–98

[12] Collet E. Polarized Light: Fundamentals and Applications. New York: Marcel Dekker; 1993

[13] Therézio EM, da Silva SFC, Dalkiranis GG, Alliprandini-Filho P, Santos GC, Ely F, et al. Light polarization states of a cholesteric liquid crystal probed with optical ellipsometry. Optical Materials. 2015;**48**:7–11

[14] Basílio FC, Campana PT, Therézio EM, Barbosa Neto NM, Serein-Spirau F, Silva RA, et al. Ellipsometric Raman spectroscopy. The Journal of Physical Chemistry C. 2016;**120** (43):25101–25109

[15] Basílio FC. Implementation of the New Technique Raman Spectroscopy by Elipsometry no Chiral Molecules Study. Uberlândia: Universidade Federal de Uberlândia; 2014

[16] Stokes GG. On the composition and resolution of streams of polarized light from different sources. Transactions of the Cambridge Philosophical Society. 1852;**9**:399–416

[17] Therézio EM, Franchello F, Dias IFL, Laureto E, Foschini M, Bottecchia OL, et al. Emission ellipsometry as a tool for optimizing the electrosynthesis of conjugated polymers thin films. Thin Solid Films. 2013;**527**:255–260

[18] Therézio EM, Rodrigues PC, Tozoni JR, Marletta A, Akcelrud L. Energy-transfer processes in donor-acceptor poly(fluorenevinylene-alt-4,7-dithienyl-2,1,3-benzothiadiazole). The Journal of Physical Chemistry C. 2013;**117**(25):13173–13180

[19] Pereira GGD. Study of liquid crystal mesophases by emission ellipsometry technique [dissertation]. Uberlândia: Universidade Federal de Uberlândia; 2013

[20] Alliprandini-Filho P, Dalkiranis GG, Armond RASZ, Therezio EM, Bechtold IH, Vieira AA, et al. Emission ellipsometry used to probe aggregation of the luminescent 2,1,3-benzothiadiazole dyes and ordering in an E7 liquid crystal matrix. Physical Chemistry Chemical Physics. 2014;**16**(7):2892–2896

[21] Galyametdinov YG, Knyazev AA, Dzhabarov VI, Cardinaels T, Driesen K, Görller-Walrand C, et al. Polarized luminescence from aligned samples of nematogenic lanthanide complexes. Advanced Materials. 2008;**20**(2):252–257

[22] Alliprandini-Filho P, Borges GF, Calixto WB, Bechtold IH, Vieira AA, Cristiano R, et al. Molecular alignment effects on spectroscopic properties 2,1,3-benzothiadiazole guested in liquid–crystalline compounds. Chemical Physics Letters. 2010;**487**(4-6):263–267

[23] Cristaldi DJR, Pennisi S, Pulvirenti F. Liquid Crystal Display Drivers: Techniques and Circuits. Catania: Springer; 2009

Chapter 3

The Development of Three-Intensity Measurement in PSA Ellipsometry and Photoelastic Modulation Ellipsometry

Yu-Faye Chao

Additional information is available at the end of the chapter

http://dx.doi.org/10.5772/intechopen.70086

Abstract

A three-intensity measurement technique in a polarizer-sample-analyzer (PSA) ellipsometry will be introduced. The alignment of the azimuth angle of polarizer and analyzer to the incident plane will be discussed. Its applications to measure the ellipsometric parameters for deducing the optical parameters will be stated. In addition to the PSA ellipsometry, one can insert a photoelastic modulator (PEM) in the PSA ellipsometry for developing a PEM ellipsometry. There is no moving part in the system and its measuring speed is only limited by a modulator. An in situ/real-time and post-flight ellipsometry can be established for monitoring the dynamically varying process.

Keywords: alignment, calibrations, curved surface, real time

1. Introduction

The ellipsometry measures the change in polarization upon reflection or transmission [1] and then compares it with a model to deduce the optical parameters, such as the complex refractive index, film thickness, crystalline nature, and roughness of a sample. The ratio of the reflection coefficient in p-polarized light (r_p) to s-polarized light (r_s) has been noted as $\tan\Psi\, e^{i\Delta}$, where Ψ and Δ are the two ellipsometric parameters measured in ellipsometer. These parameters are very sensitive to the change in the optical response of incident radiation that interacts with the material. A commercial ellipsometer for measuring the thickness of a thin film has to achieve the precision within 2 Å in order to attract the IC industry for thin film measurement. This means the precision of Ψ and Δ have to be less than 0.02° and 0.04°, respectively. In ellipsometry, the alignment and calibration are the crucial techniques for achieving these precisions. These techniques fully depend on the configuration of the system. First, one has to

establish the plane of incident by aligning the azimuth angle of polarizer and analyzer to the plane of incident, both of which are the fundamental components of ellipsometer. Collins [2] and Chao [3] applied the null technique and the intensity ratio technique to locate the azimuth zeros of polarizer (P) and analyzer (A) with respect to the plane of incident, respectively. Both methods are complicated and time consuming. Due to the development of symbolic computer program Mathematica, one can analytically obtain the zeros of polarizer and analyzer with respect to the incident plane. In this chapter, the azimuth zeros of P and A to the incident plane will be located by an intensity ratio method. By rotating the analyzer, a three-intensity measurement technique will be applied to measure the ellipsometric parameters. According to the theoretical models, one can deduce the optical parameters from the measured ellipsometric parameters. Since only three intensities are needed to be measured, the imaging ellipsometry can be established. By using the following models: (a) the film thickness of flat and curved surface; (b) the refractive indices of homogeneous and nonhomogeneous bulk medium; (c) focused beam for surface plasmon resonance (SPR) phenomena, one can prove that this simple imaging ellipsometry has many different applications.

The photoelastic modulator (PEM) will be introduced in the polarizer-sample-analyzer (PSA) ellipsometric system for an in situ/real-time ellipsometry. The in situ alignment technique of the optical axis of PEM is essential for establishing a real-time ellipsometry. Here, the real-time measurements of the ellipsometric parameters under etching and thermal heating processes will be presented. In addition to real time, one can also use the post-flight technique to analyze the digital waveform of an anisotropic medium.

2. The alignment in PSA ellipsometry

The PSA ellipsometry setup is shown in **Figure 1**. Before inserting the PEM, one can setup the PSA ellipsometry for three-intensity measurement. For aligning the azimuth angles of P and A with respect to the incident plane, one can setup the PSA configuration in the interested incident angle (typical 70° in IC industry). The measured reflected intensity is expressed in the ellipsometric parameters, Ψ, Δ, and azimuth angles of P and A:

$$I(P,A) = I_0\left[\sin^2 P \sin^2 A + \tan^2\Psi \cos^2 P \cos^2 A + \frac{1}{2}\tan\Psi \cos\Delta \sin 2P \sin 2A\right] \quad (1)$$

By considering the polarizer and analyzer separately, Chao [4] improved Steel's [5] intensity ratio technique to align the polarizer and analyzer to the incident plane. For alignment, the following intensity ratios A and B are defined:

$$A(\alpha,\beta) = \frac{I(45^\circ+\alpha,\beta)}{I(45^\circ+\alpha,90^\circ+\beta)} \quad (2)$$

$$B(\alpha,\beta) = \frac{I(-45^\circ+\alpha,\beta)}{I(-45^\circ+\alpha,90^\circ+\beta)} \quad (3)$$

http://dx.doi.org/10.5772/intechopen.70086

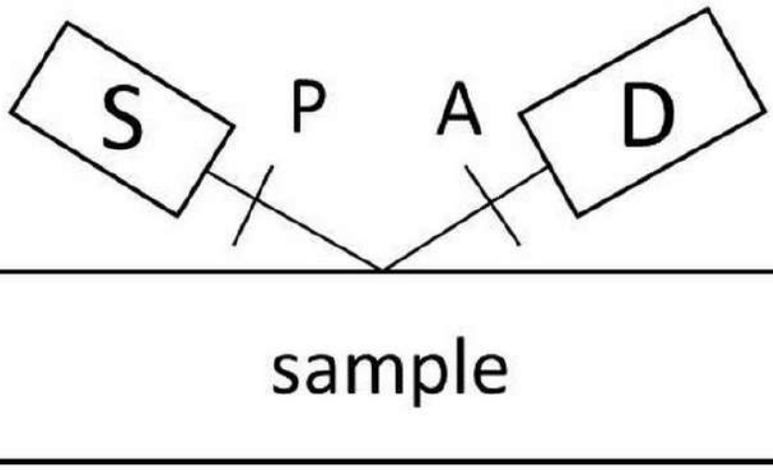

Figure 1. Schematic setup of PSA ellipsometry: A: analyzer, S, light source; P, polarizer; D, detector.

In addition to the azimuth angle of P and A, the small angle deviation α and β from the incident plane, respectively, are considered. These intensity ratios are expanded to the first-order approximation around their respective scales, and expressed as follows:

$$A(\alpha,\beta) \cong \tan^2\psi - 2\left[2\tan^2\Psi\ \alpha - \sec^2\Psi\ \tan\Psi\ \cos\Delta\ \beta\right] \tag{4}$$

$$B(\alpha,\beta) \cong \tan^2\Psi + 2\left[2\tan^2\Psi\ \alpha - \sec^2\Psi\ \tan\Psi\ \cos\Delta\ \beta\right] \tag{5}$$

These two equations intersect with each other when

$$2\tan^2\Psi\ \alpha - \sec^2\Psi\ \tan\Psi\ \cos\Delta\ \beta = 0 \tag{6}$$

so the deviation of α and β can be easily obtained for the opposite of cosΔ. Two incident angles [3], and fixed incident angle by two samples and two wavelengths [6] are proposed to align the azimuth angles of polarizer and analyzer. These complicated processes can be substituted by an analytical measurement technique [7]. In polar coordinates, if the incident light is E_p=E_s, the reflected intensity is distributed in an elliptical form [5] as shown in **Figure 2**, which can be formulated as

$$I(A) = L\cos^2(A-\theta) + T\sin^2(A-\theta) \tag{7}$$

where L and T are the magnitudes of the maximum and minimum intensities, respectively, and θ is the azimuth of maximum intensity. Since there are only three unknowns, one can measure three intensities to deduce the three parameters. Eq. (7) can also be written as follows:

$$I(A) = B(1 + C\cos 2A + D\sin 2A) \tag{8}$$

where the parameters B, C, and D can be written in terms of L, T, and θ, that is, B = 0.5(L+T), C = (L−T)cos2θ/(L+T), and D = (L−T)sin2θ/(L+T). It is easy to prove that parameters B, C, and D can be measured by three intensities measured at A = 0°, 60°, and 120°;

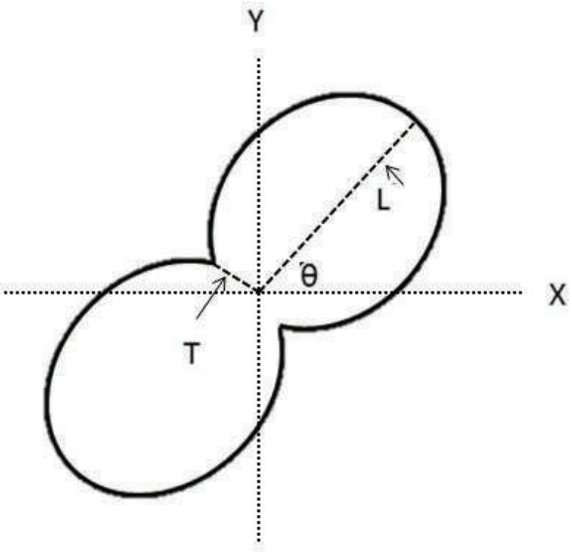

Figure 2. Intensity distribution in polar coordinates at various azimuth angles of analyzer.

$$B = \frac{1}{3}[I(0^\circ) + I(60^\circ) + I(120^\circ)] \tag{9}$$

$$C = 2 - [I(60^\circ) + I(120^\circ)]/B \tag{10}$$

$$D = \frac{1}{B\sqrt{3}}[I(60^\circ) - I(120^\circ)] \tag{11}$$

So, $\tan 2\theta = D/C$; $L = B + DB/\sin 2\theta$ and $T = 2B - L$. By comparing the expansion of Eq. (1), one can obtain the following relationships:

$$\tan 2\theta = \frac{\cos\Delta \ \sin 2P \ \sin 2\Psi}{\cos 2P - \cos 2\Psi} \tag{12}$$

$$\tan^2\Psi = \frac{1+C}{1-C}\tan^2 P \tag{13}$$

$$\frac{(L-T)^2}{4LT}\sin^2 2\theta = \cot^2\Delta \tag{14}$$

when there is no deviation in the azimuth angles of polarizer and analyzer. Even there are deviations α and β for P and A, respectively, one can substitute those errors in the previous relations and obtain the analytical results, that is

$$\sin 2\alpha = \frac{1 - \sqrt{\frac{(1+C_1)(1-C_2)}{(1-C_1)(1+C_2)}}}{1 + \sqrt{\frac{(1+C_1)(1-C_2)}{(1-C_1)(1+C_2)}}} \tag{15}$$

$$\tan\Psi = 4\sqrt{\frac{1 - \sqrt{\frac{(1+C_1)(1-C_2)}{(1-C_1)(1+C_2)}}}{1 + \sqrt{\frac{(1+C_1)(1-C_2)}{(1-C_1)(1+C_2)}}}} \tag{16}$$

http://dx.doi.org/10.5772/intechopen.70086

$$\beta = \frac{1}{4}\left(\tan^{-1}\frac{D_1}{C_1} - \tan^{-1}\frac{D_2}{C_2}\right) \tag{17}$$

where subscripts 1 and 2 indicate the three-intensity measurement obtained at P = 45° and −45°, respectively. After correction, the value Δ can be obtained by substituting the corrected value into the appropriate relation. The most important aspect of this technique is the concept of direct determination, in contrast to locating the minimum intensity in the null ellipsometry, which not only requires a sensitivity detector but also requires a polarizer with a high extinction ratio. This intensity ratio technique only needs a minimum amount of data to deduce the deviations and ellipsometric parameters simultaneously. If the detector is a high-dynamic range detector, the precision of this three-intensity measurement technique will be compatible to the commercial ellipsometer. Moreover, a complicated alignment process is not required in the simple PSA ellipsometry.

3. Three-intensity measurements technique in PSA ellipsometry

The analytical alignment technique provides a simple and accurate alignment technique in ellipsometry. Since only three-intensity measurements are required, one can use charge-coupled device (CCD) as a detector for imaging ellipsometry.

3.1. Film thickness of SiO_2/Si thin film

In the beginning, the azimuth angles of polarizer and analyzer are aligned to the incident plane by the Brewster angle of a nonabsorbent as the reference zero. After the rough alignment, the azimuth angle of polarizer is set at 45° and −45°, respectively, for analyzer to be at three angles, that is, 0°, 60°, and 120°, and the corresponding three-intensity measurements. One can choose an appropriate incident angle (typical 70°) for ellipsometric measurements. Using the relations in the last section, one can calculate Ψ, Δ, α, and β from three-intensity measurements. According to the definition of ellipsometric parameters to Fresnel reflection coefficient [1], one can deduce the film thickness of thin film (SiO_2/Si thin film) through computer program. The primary objective is to compare the ellipsometric parameters measured with rough alignment to the analytically corrected values. Just as expected, the system errors are clearly observable in the deduced values of Ψ and Δ, measured at P = 45° and −45° separately, as shown in **Figure 3**. After readjusting the azimuth angles of polarizer and analyzer, one can observe the flat distribution of Ψ and Δ measured at P = 45° and −45°. The corrected ellipsometric parameters of the results deviated from each other by less than 0.01°, as shown in **Tables 1** and **2**. The corrected values are used for film thickness deduction. It is known that a rotating polarizer ellipsometry can deviate the incident angle [8]; the incident angle for thickness deduction is 69.94° instead of 70°.

3.2. Imaging ellipsometry

In the PSA ellipsometry, one can add a beam expander and use CCD as a detector, such as shown in **Figure 4**. This imaging ellipsometry can measure the refractive index of a flat bulk

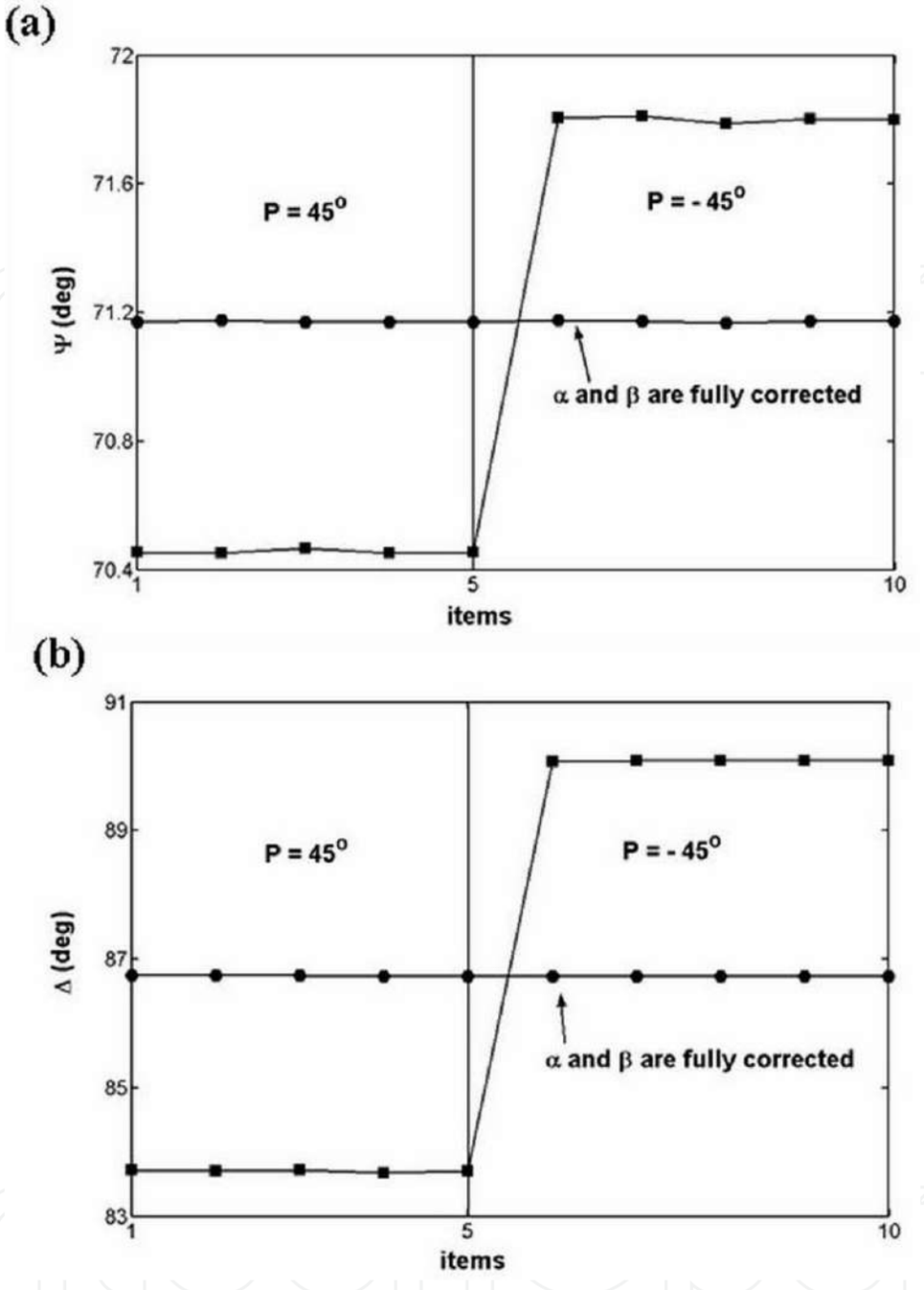

Figure 3. Ellipsometric measurements of PSA ellipsometry for a SiO_2 film on a Si substrate: (a) ψ and (b) Δ measured after a rough alignment (filled squares) at P = 45° and −45°, where $\alpha = 0.998 \pm 0.011°$ and $\beta = 1.233 \pm 0.005°$ and after readjusted (filled circles) at P = 45° and −45°, where $\alpha = 0.015 \pm 0.009°$ and $\beta = 0.006 \pm 0.003°$.

medium, curved surface, and film thickness on a curved surface. Moreover, the SPR phenomena will be presented by a focused light beam.

3.2.1. Refractive index of flat surface of a bulk medium

Since there is no multiple reflection on a bulk medium, the refractive index of a bulk medium can be easily obtained by the ellipsometric parameter from the following relationship, let $\rho = \tan\Psi e^{i\Delta}$, then

http://dx.doi.org/10.5772/intechopen.70086

Experiment	'ψ (deg)	Δ (deg)	Thickness (nm)	α (deg)	β (deg)
1	71.172	86.742	129.89	0.993	−1.229
2	71.175	86.745	129.93	1.000	−1.234
3	71.169	86.754	129.85	0.968	−1.231
4	71.171	86.727	129.88	0.991	−1.241
Mean	71.171	86.741	129.88	0.988	−1.233
Standard deviation	0.003	0.011	0.03	0.011	0.005
Jobin-Yvon ellipsometer			129.3		

Table 1. Optimized ellipsometric measurements of PSA ellipsometry for a SiO_2 film on a Si substrate after rough alignment.

Experiment	'ψ (deg)	Δ (deg)	Thickness (nm)	α (deg)	β (deg)
1	71.176	86.739	129.94	0.017	−0.011
2	71.174	86.731	129.93	0.013	−0.005
3	71.166	86.728	129.87	0.003	−0.005
4	71.174	86.726	129.91	0.026	−0.004
Mean	71.173	86.731	129.91	0.015	−0.006
Standard deviation	0.004	0.006	0.03	0.009	0.003

Table 2. Optimized ellipsometric measurements of PSA ellipsometry for a SiO_2 film on a Si substrate after readjusting azimuth angles of polarizer and analyzer.

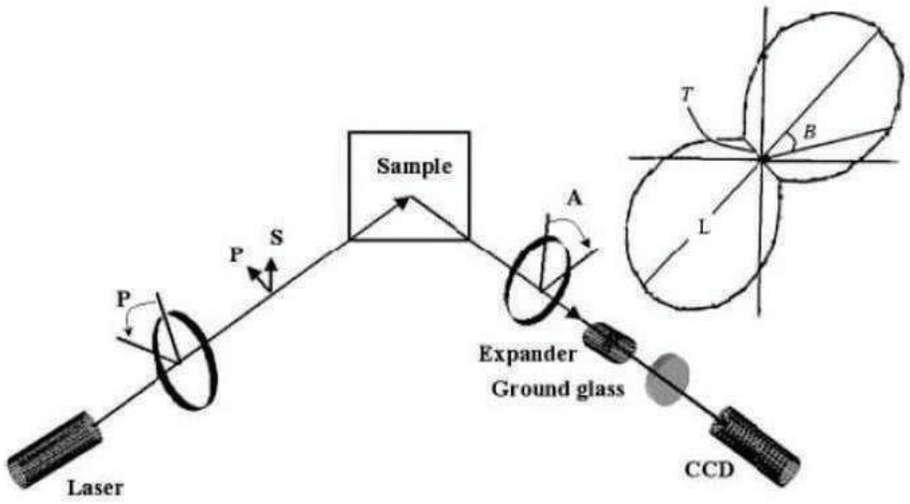

Figure 4. Schematic setup of the PSA imaging ellipsometer: Laser; P, polarizer; A, analyzer; S, sample; Expander, beam expander, and CCD camera. The elliptically distributed intensity on the right is under various azimuth angles of A in the polar coordinates.

$$n_1 = n_0 \tan\theta_i \left[1 - \frac{4\rho}{(1+\rho)^2} \sin^2\theta_i\right]^{\frac{1}{2}} \tag{18}$$

where n_1, n_0 are the refractive indices of bulk medium and incident medium, respectively. $\theta\iota$ is the incident angle.

The graded index structure has been widely used in fiber communication, in technologies such as the graded index fiber, and the gradient-index (GRIN) lens. The knowledge of the refractive index profile (RIP) of this graded index structure is important not only to assess its performance in optical devices but also to control the quality of products [9]. Since it is very important to measure the RIP of a gradient index material, the nondestructive measurement using imaging ellipsometry is suggested. The well-known material BK7 glass can be used to evaluate this imaging ellipsometry, such as shown in **Figure 5**. Since glass is nonabsorbent, the refractive index can be obtained by Ψ. In addition, the RIP of a gradient index fiber can be measured; its surface property can also be examined by α, such as shown in **Figure 6**, which will be proved that it is the direction of surface's normal.

3.2.2. The curved surface

Surface topography is a topic of great interest to science, technology, and industry. Both the contact stylus-based instruments [10] and noncontact optical instruments [11] can be used to measure and characterize the topography of a surface. By performing the ellipsometric measurements at two azimuth angles of the polarizer that differ by 90°, one can determine the azimuth deviation (α) of polarizer with respect to the incident plan by the three-intensity technique of PSA ellipsometry. After adjusting the deviation, one can prove that the azimuth

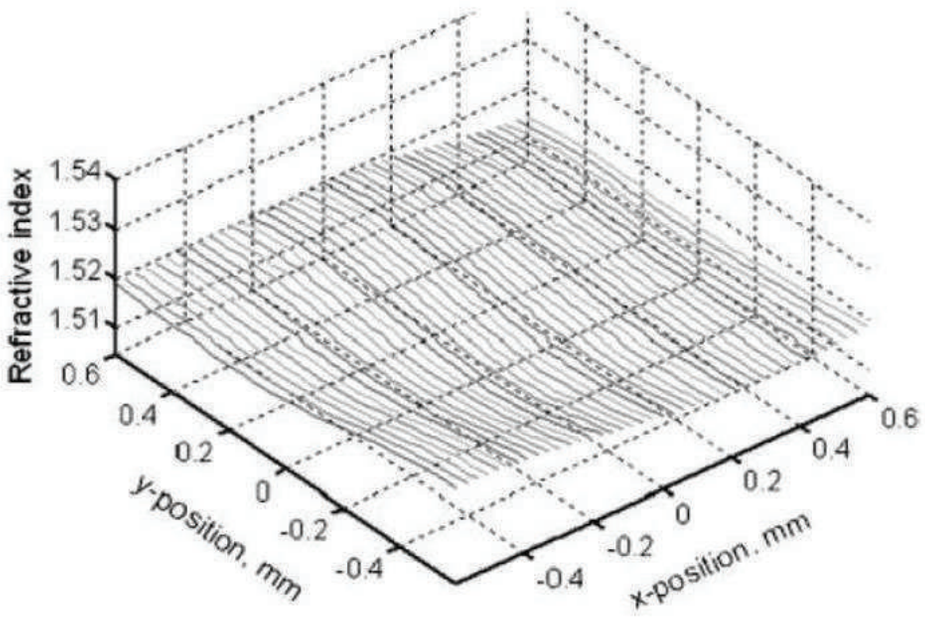

Figure 5. Imaging ellipsometric study of a BK7 glass: n = 1.520±0.003.

http://dx.doi.org/10.5772/intechopen.70086

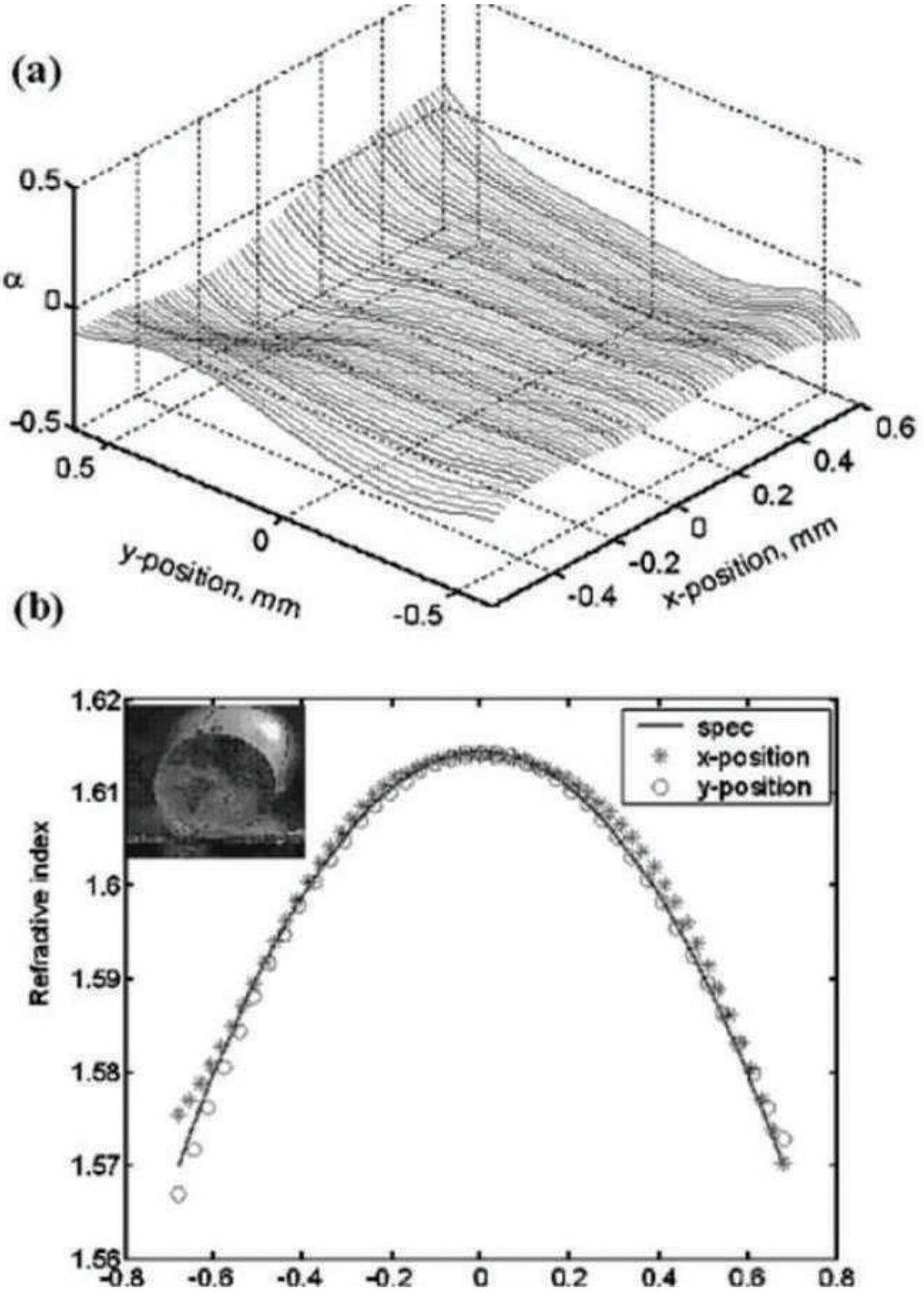

Figure 6. Imaging ellipsometric study of a flat GRIN lens: (a) azimuth deviation (α) of the surface. (b) Measured refractive index profile (*: x-axis, ○: y-axis, solid line: RIP provided by NSG).

deviation of polarizer measured by this imaging ellipsometry can be used to measure the surface's normal; thus, it can be used to measure the surface topography of a lens. In the beginning, the alcohol surface is regarded as a flat surface for calibration; then one can tilt an SiO_2/Si sample for investigating its effect to the azimuth deviation of polarizer. In the previous section, the refractive index profile of a GRIN lens has been obtained. Here, one can use the same technique to measure the RIP of the diluted alcohol, such as shown in **Figure 7**. Since both the GRIN lens and diluted alcohol have flat surfaces, their azimuth deviations are near to zero. Tilting a plate confirms that α can be used to measure the normal line of the surface, such as shown in **Figure 8**. After understanding the meaning of α, one can measure the refractive index of a BK7 plano-convex lens and its surface's normal, such as shown in **Figure 9**. This can be flattened by correcting the α, as shown in **Figure 10**. Furthermore, one can rotate the tilted SiO_2/Si to investigate the three-direction cosines of the surface's normal. From the top view of a tilted plane, such as shown in **Figure 11b**, one can identify the surface's normal deviated by the tilted angle Θ with components α, and $\Delta\theta$ along x- and y-axes, respectively. The measured deviation α is the surface's normal projected on x-axis, which is perpendicular to the intersection of incident plane and sample surface. $\Delta\theta$ is the deviation of the incident angle caused by the tilting and can be deduced from the three-direction cosines. Three positions are examined, **Table 3**; all these results can be used to deduce the thickness of the thin film SiO_2 on silicon substrate [12]. For simplicity, one shall use a cylindrical lens and set it up as in **Figure 12**, then examine the thickness of its coating by the three-intensity measurements technique, the

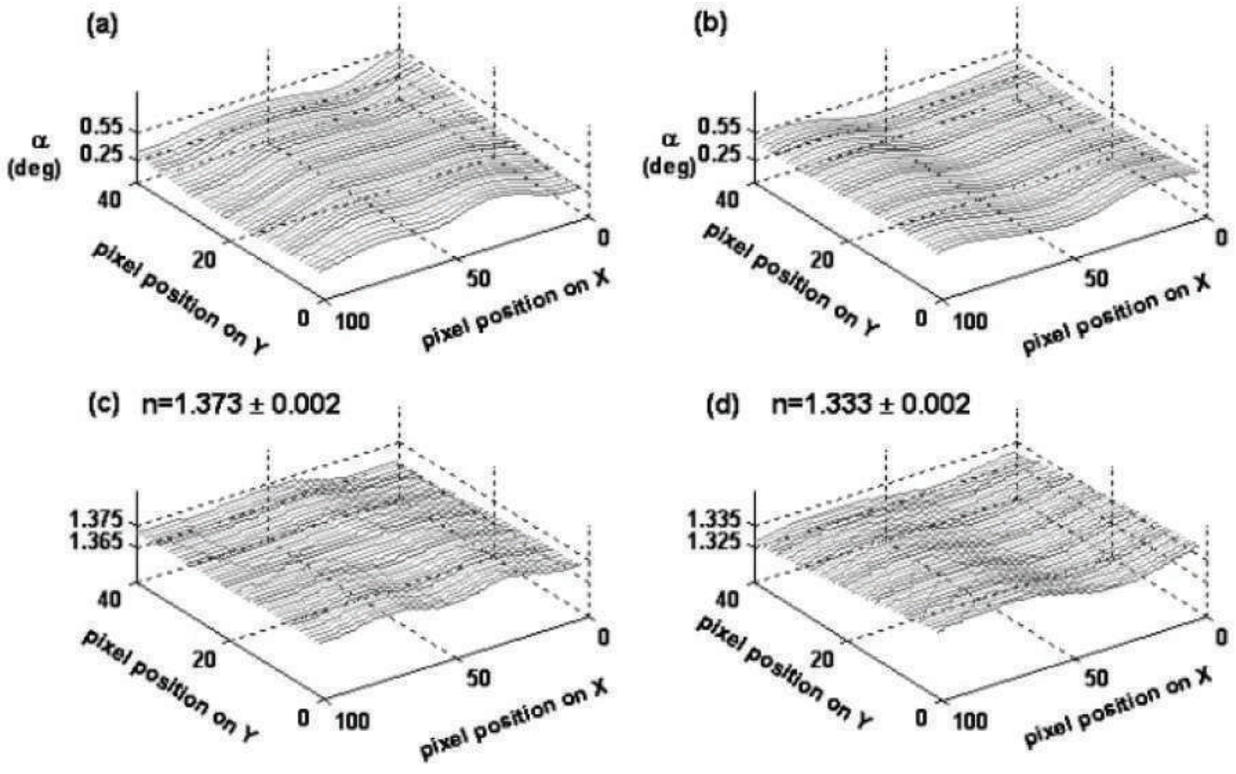

Figure 7. Imaging ellipsometric study of water and diluted alcohol: (a) azimuth deviation (α) of the diluted alcohol surface, (b) azimuth deviation (α) of the water surface, (c) refractive index profile of diluted alcohol n = 1.373 ± 0.002, and (d) refractive index profile of water n = 1.333 ± 0.002.

http://dx.doi.org/10.5772/intechopen.70086

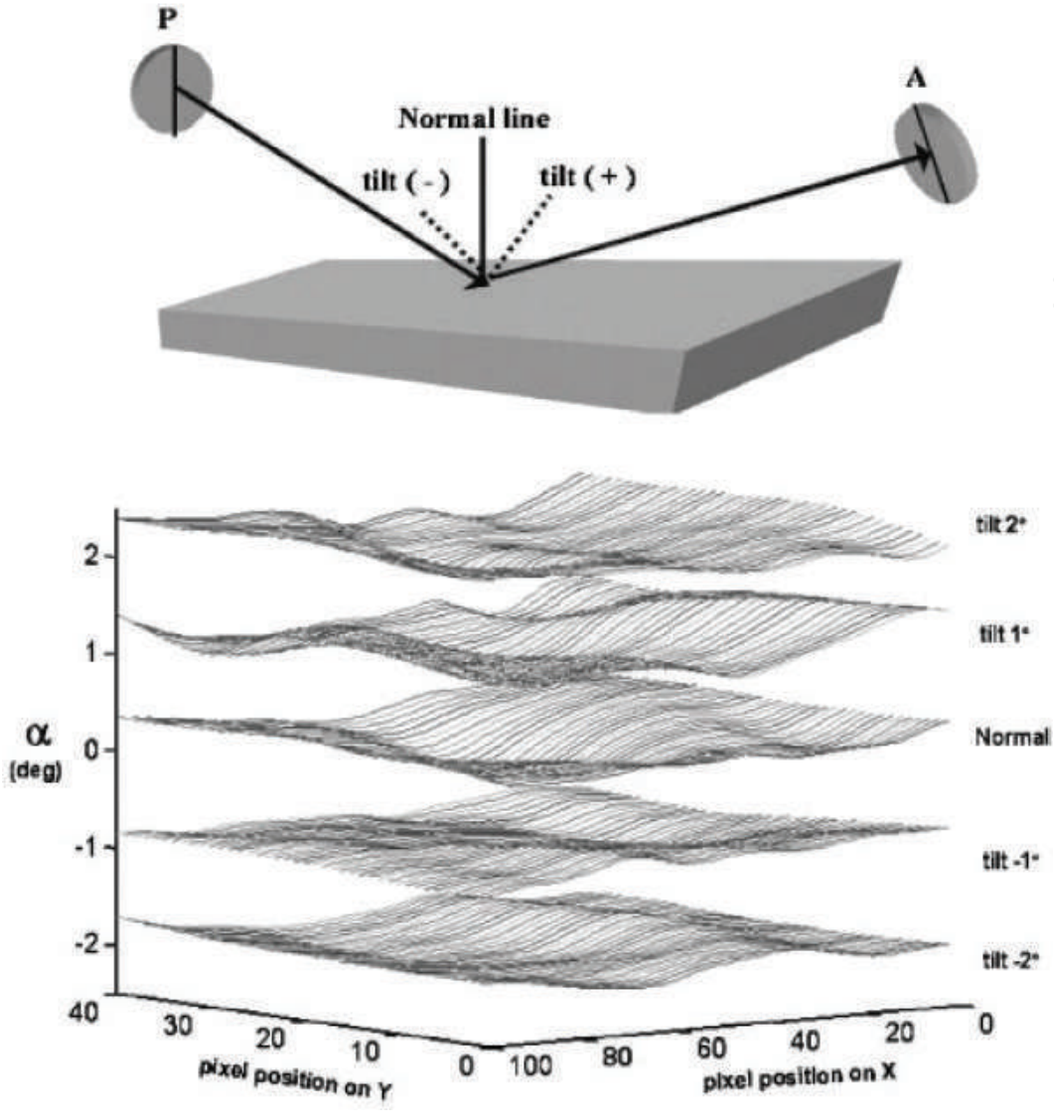

Figure 8. Imaging ellipsometric study of azimuth deviation of polarizer (a) caused by the tilting of a SiO_2 thin film on Si substrate. The thin film is tilted from −2 to 2° with step 1°.

measured Ψ and Δ are shown in **Figure 13**. In this configuration, the measured α is zero at the vertex of the cylinder. The corrected Ψ and Δ are flat which can be used to deduct the thickness of the coating. In conclusion, this three-intensity measurement technique can perform a measurement on thin film coating of a curved and titled surface with high precision.

3.2.3. Focused beam and surface plasmon resonance

In conventional ellipsometry, the light beam has to be collimated carefully to avoid the polarization errors. In the last section, we show that one can perform the ellipsometric measurement of a curved surface. Since the three-direction cosines have been well understood, one can measure a convergent/ divergent beam without any restriction [13]. Using a focused beam in the PSA imaging ellipsometry, one can perform the ellipsometric measurement under the surface plasmon resonance (SPR) condition and observe the resonance phenomena.

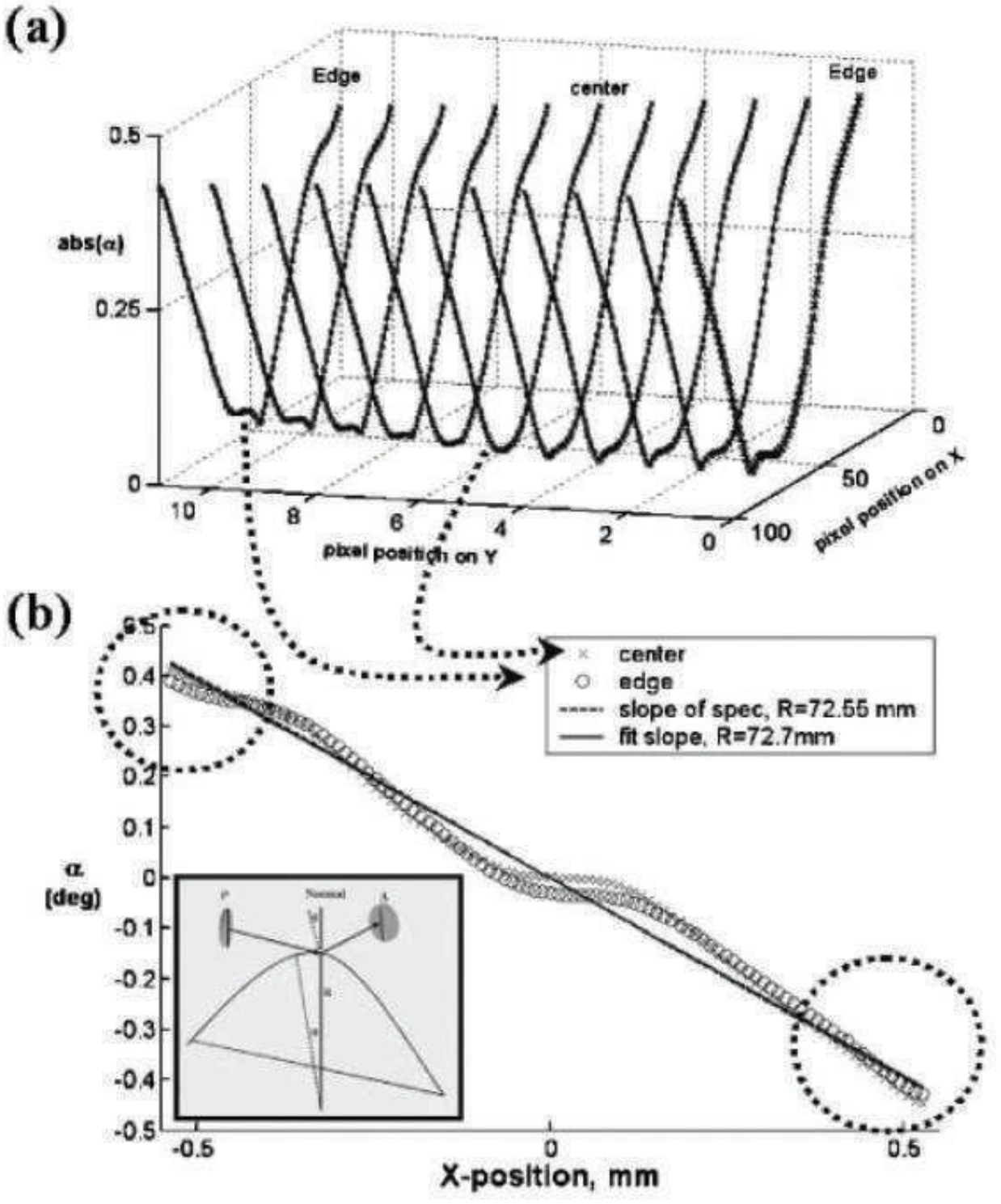

Figure 9. Imaging ellipsometric study of the radius of curvature of the BK7 plano-convex lens: (a) the magnitude of the azimuth deviation (α) of the surface and (b) the derived and measured α of the lens at the center and the edge (dashed line: derived from the radius measured by the Zygo phase-shift interferometer, solid line: measured by the imaging ellipsometric technique).

http://dx.doi.org/10.5772/intechopen.70086

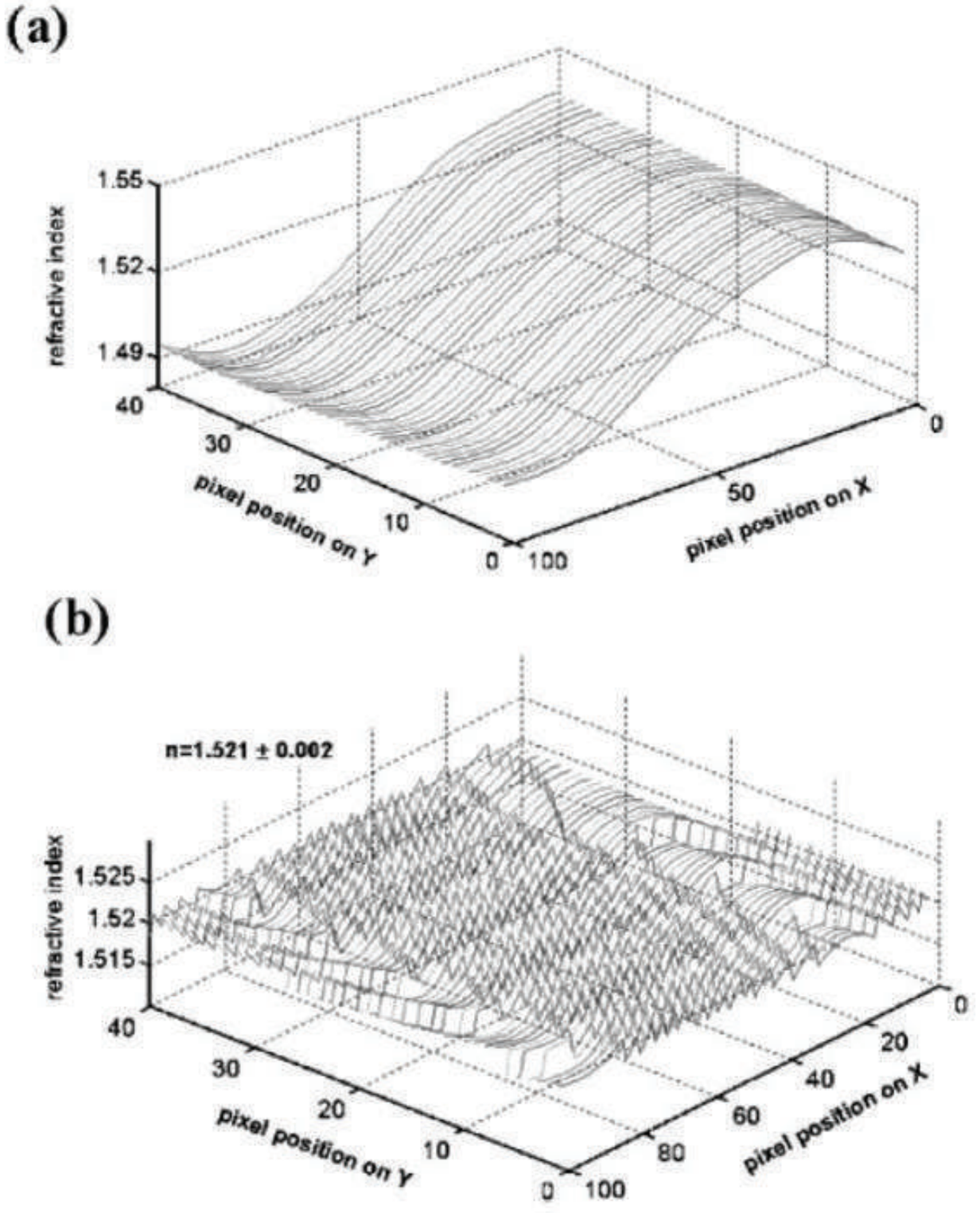

Figure 10. Imaging ellipsometric study of the RIP of the BK7 plano-convex lens: (a) the deduced RIP by considering the incident angle at 70° and (b) the deduced RIP by substituting its corresponding incident angles.

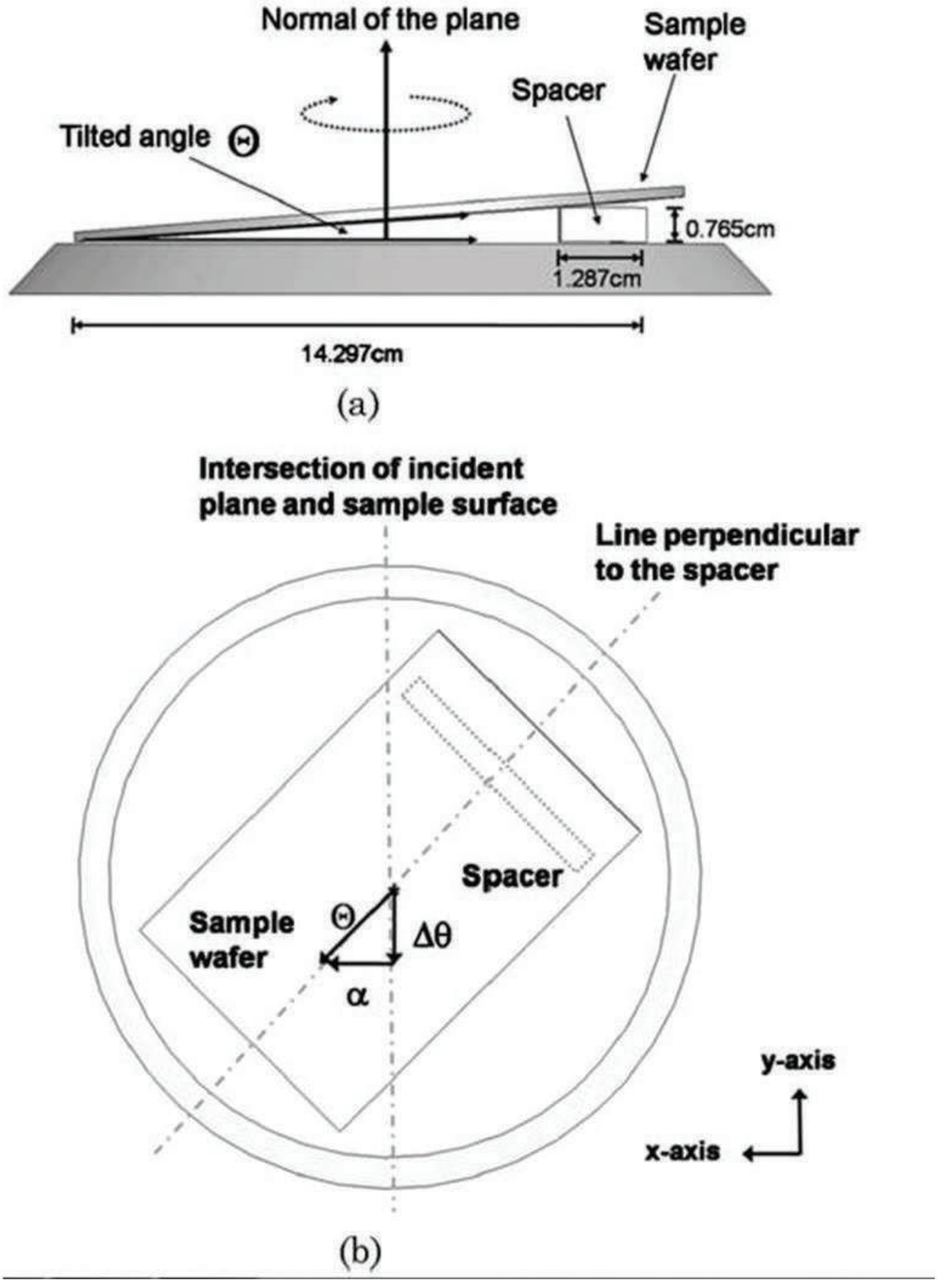

Figure 11. Schematic configuration of a tilted sample: (a) side view and (b) top view that indicates the motion of its surface normal: Θ, the tilted angle by spacer; Δθ, the component that contributes to the incident angle variation; α, the component measured in the deviation of the polarizer.

http://dx.doi.org/10.5772/intechopen.70086

Condition	Ψ (deg)	Δ (deg)	α (deg)	$\Delta\alpha$ (deg)	θ^a (deg)	$\Delta\theta$ (deg)	Θ^a (deg)
Untilted	69.28	90.35	0.02	2.59	69.76	1.35	2.94
Tilted	69.68	99.42	−2:57		68.41		
Untilted	69.08	90.40	0.06	2.75	69.73	1.06	2.94
Tilted	66.69	97.71	−2:69		68.67		
Untilted	69.24	90.42	0.06	2.95	69.75	0.08	2.94
Tilted	68.89	89.71	−2:89		69.83		

[a]θ, the incident angle; Θ, the tilted angle; the relationship of the three-direction cosine is $\cos^2\Theta = 1-[\sin^2\Delta\alpha + \sin^2\Delta\theta]$.

Table 3. Ellipsometric measurements of tilted and untilted samples.

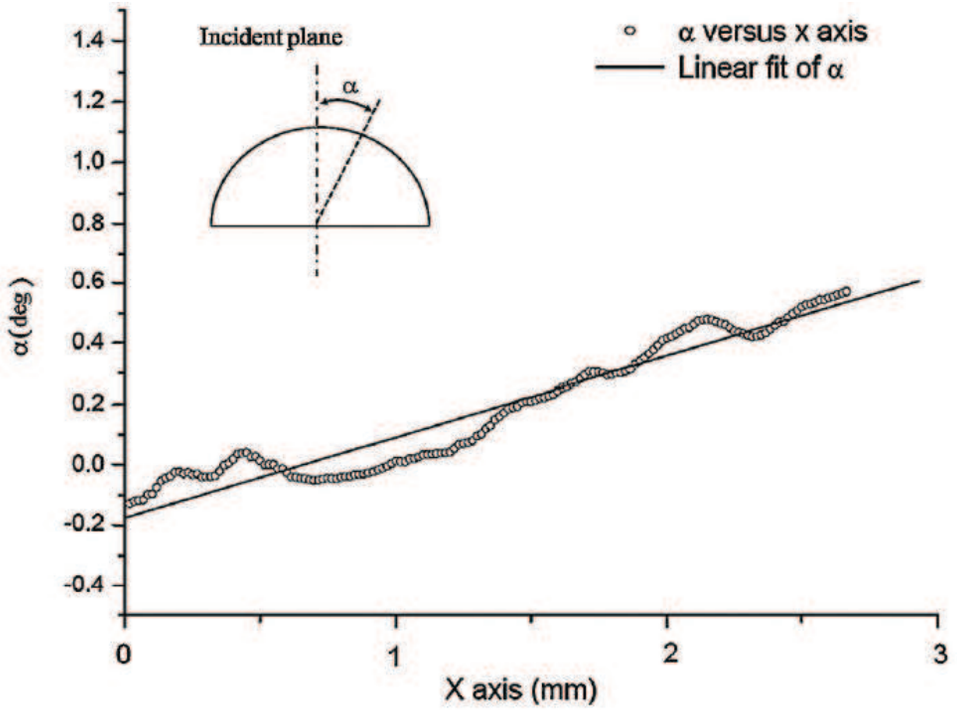

Figure 12. Deviation angle of the surface normal across the vertex of a cylindrical lens: open circles, measured α across the vertex of the lens; solid line, its best linear fit.

A cylindrical lens is used to produce a fan-shaped beam for multiple incident angles configuration. This can simplify the analysis to be a two-dimensional case. The three-intensity measurement technique can measure the ellipsometric parameters against each incidence angle but do not have to calibrate the azimuth errors of polarizer and analyzer. As a result of multiple incident angles approach, the whole Ψ curve around the SPR region can be obtained without rotating the sensor chip. The basic setup of the SPR sensor chip is in Kretchmann's configuration, such as shown in **Figure 14**. The beam can be expanded by a beam expander, then focused it on the base of a prism/biosensor around the resonance incident angle (air: 44°). One can measure the three intensities when P is at 45° and −45°, respectively. The measured intensities

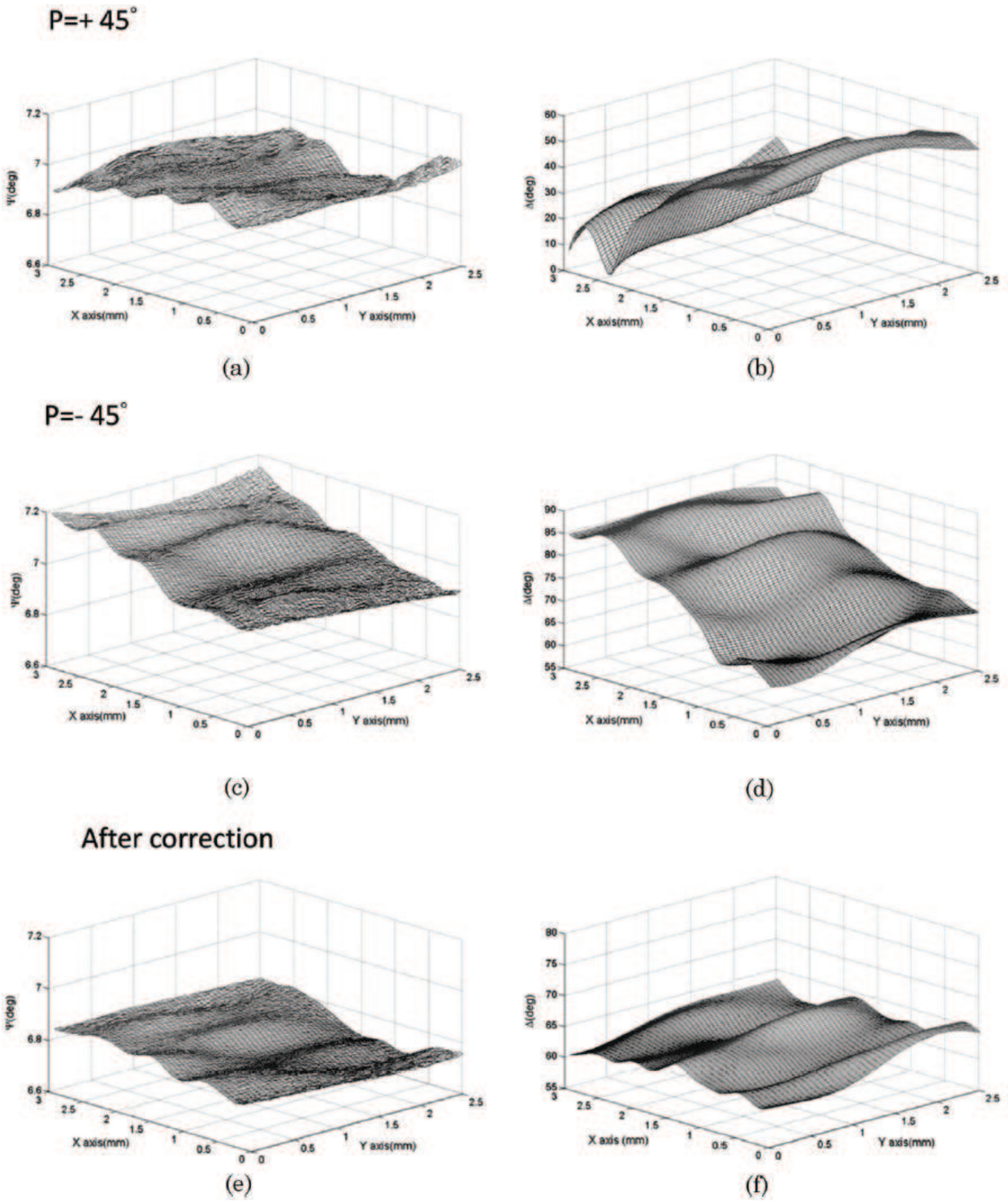

Figure 13. Ellipsometric parameters and thickness profile of the cylindrical lens: (a) Ψ and (b) Δ measured when P = 45°; (c) Ψ and (d) Δ measured when P = −45°; (e) Ψ and (f) Δ after correction. Film thickness is 100±4.3 nm.

can be converted into ellipsometric parameters Ψ and Δ. Since the SPR phenomenon is more clearly observable by Ψ, we would like to present it by the distribution of Ψ versus the incident angle. The sensor chip is in Au/air (**Figure 15**) assembly. The solid line in the figure represents the theoretical value. This result can be used for calibration before other measurements.

http://dx.doi.org/10.5772/intechopen.70086

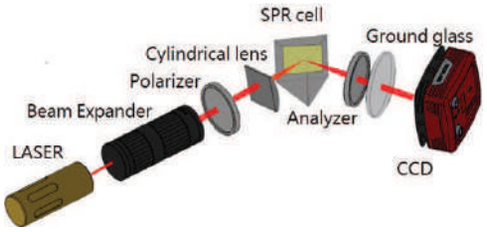

Figure 14. The schematic setup of SPR for imaging ellipsometry.

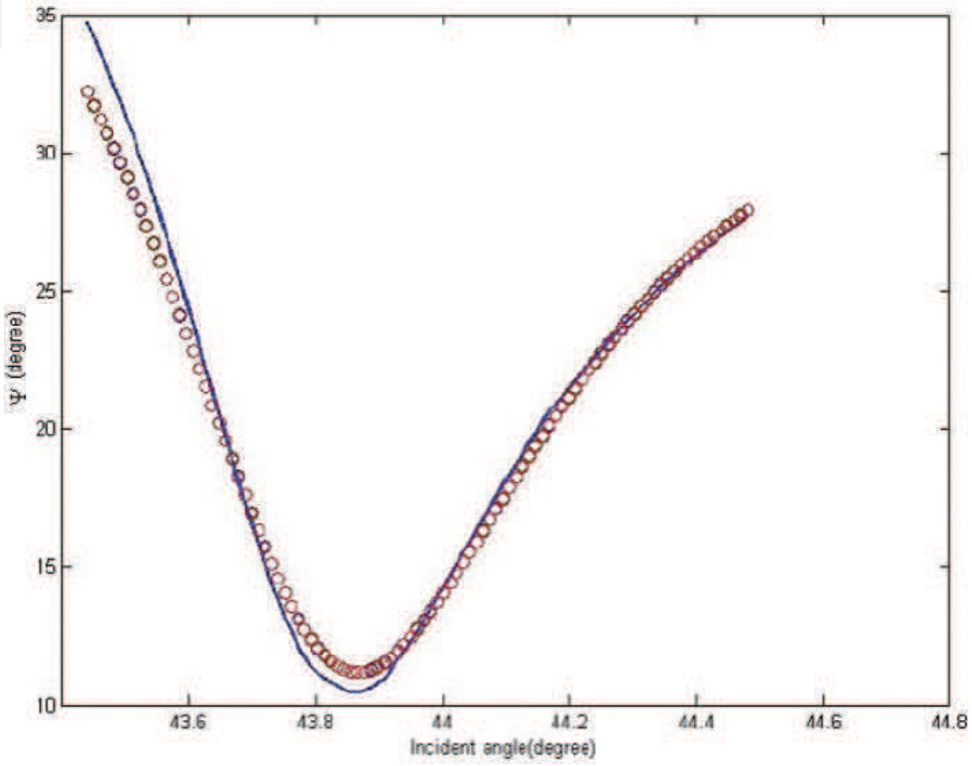

Figure 15. The distribution of Ψ versus incident angle of the sensor chip in air (circles are the measured value; solid line is the theoretical value).

4. PEM ellipsometry

In PSA ellipsometry, one has to rotate both polarizer and analyzer in order to measure the ellipsometric parameters. These rotations do cause the incident angle to deviate from the setup and slow down the speed of measurements. In the beginning of 1990, the real-time/in situ ellipsometric system has started to develop. By inserting a PEM in the PSA ellipsometry, one can construct an ellipsometry without any mechanical motion and thus substantially increase the speed of measurement. A photoelastic modulator (PEM) is a device that utilizes the photoelastic effect to modulate the phase retardation in a harmonic form [14]. For accurately measuring the ellipsometric parameters with high precision, one has to align the strain axis of PEM to the incident plane and calibrate its modulation amplitude. Since the incident plane has been well aligned in the PSA ellipsometry, one can easily align the strain axis to the incident plane by null and then determine its axis directly through the measurements of two DC

intensities when the azimuths of the analyzer are separated by 45°. Regarding the modulation amplitude of PEM, although one can use the waveform of its half-wave in an oscilloscope to calibrate the modulation amplitude, it is usually very hard to visualize the flat shape of the waveform while its modulation amplitude is at half-wave. Recently, there is great progress in the data acquisition (DAQ) system with multi-functions. In this chapter, we perform the two options of the DAQ system for aligning the strain axis and calibrating the modulation amplitude of PEM in the ellipsometry: (1) lock-in amplifiers and (2) digitized oscilloscope. Since the digitized waveform can be stored for analyzing, the system errors of PEM controller can be inspected.

4.1. Alignment of the strain axis of PEM

The basic setup of the PEM ellipsometer is shown in **Figure 16**. If the azimuth angle of the initial linear polarized light is set at 45°, and the strain axis of PEM deviates from the incident plane by θ, the measured intensity can be simplified as

$$I(A) = I_0\left[L\sin^2 A + M\cos^2 A \quad \tan^2\Psi + N\sin A \quad \cos A\right] \tag{19}$$

where

$$L = 0.5[1 + \cos\Delta_P + (1 - \cos\Delta_P)(1 - \sin\Delta_P)] \tag{20}$$

$$M = 0.5[1 + \cos\Delta_P + (1 - \cos\Delta_P)(1 + \sin 4\theta)] \tag{21}$$

$$N = 0.5[1 + \cos\Delta_P - (1 - \cos\Delta_P)\cos 4\theta]\tan\Psi \quad \cos\Delta - \sin\Delta_P \quad \cos 2\theta \quad \tan\Psi \quad \sin\Delta \tag{22}$$

The modulation amplitude Δ_p of PEM is modulated as $\delta_0\cos(\omega t)$. By setting the azimuth angle of analyzer at 0°, the measured intensity can be expressed as

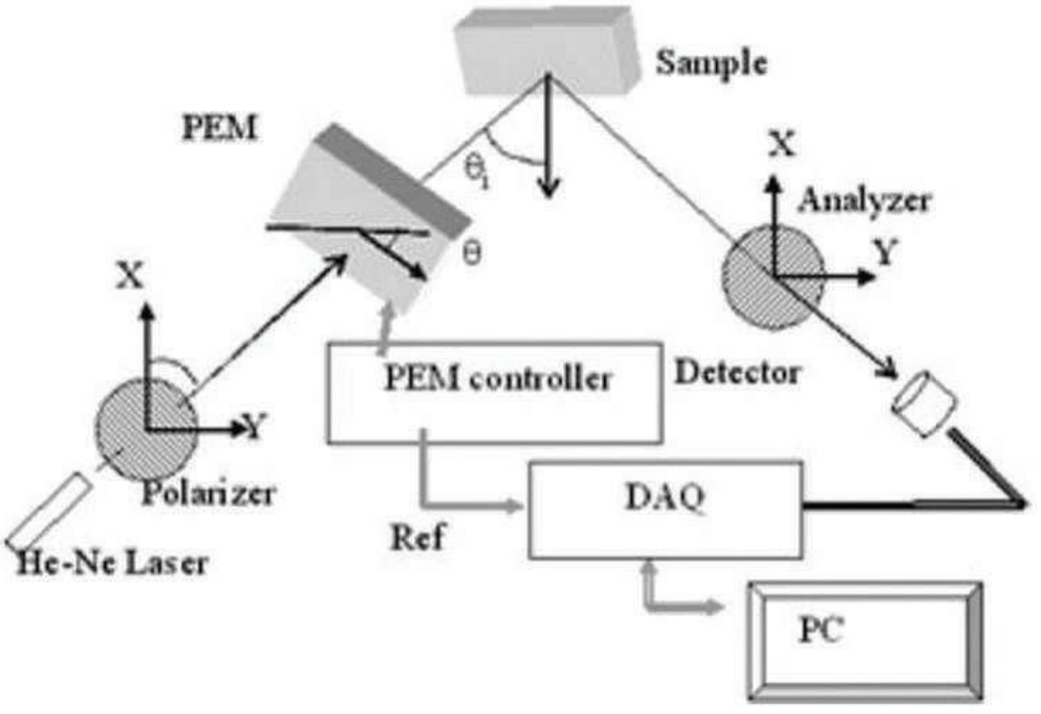

Figure 16. Schematic setup of PEM ellipsometer.

http://dx.doi.org/10.5772/intechopen.70086

$$I(0^\circ) = 0.5I_0 \tan^2\Psi \ [2 + (1 - \cos\Delta_P)\sin 4\theta] \tag{23}$$

then the intensity can be Fourier expanded by its harmonic function

$$\cos\Delta_P = J_0(\delta_0) - 2J_2(\delta_2)\cos 2\omega t \ldots \tag{24}$$

By taking the zero-order Bessel function $J(\delta_0)$ at its zero point, that is, δ_0 =0.383λ, we can simplify the DC component of its intensity as

$$I_{dc}(0^\circ) = 0.5I_0 \tan^2\Psi \ [2 + \sin 4\theta] \tag{25}$$

From this equation, the strain axis of PEM deviates from zero by θ°, which can be measured by the DC component of the intensity. Taking two I_{dc} at θ_0 and θ_0+45°, one can obtain θ_0 through the following relation:

$$\sin 4\theta_0 = 2\frac{I_{dc}(0^\circ)_{\theta=\theta_0} - I_{dc}(0^\circ)_{\theta=\theta_0+45^\circ}}{I_{dc}(0^\circ)_{\theta=\theta_0} + I_{dc}(0^\circ)_{\theta=\theta_0+45^\circ}} \tag{26}$$

A typical result after rough alignment is shown in **Figure 17**. According to the intensity ratio of Eq. (26), one can easily prove that the deviation of azimuth $\delta\theta_o$ resulting from those intensity fluctuations is

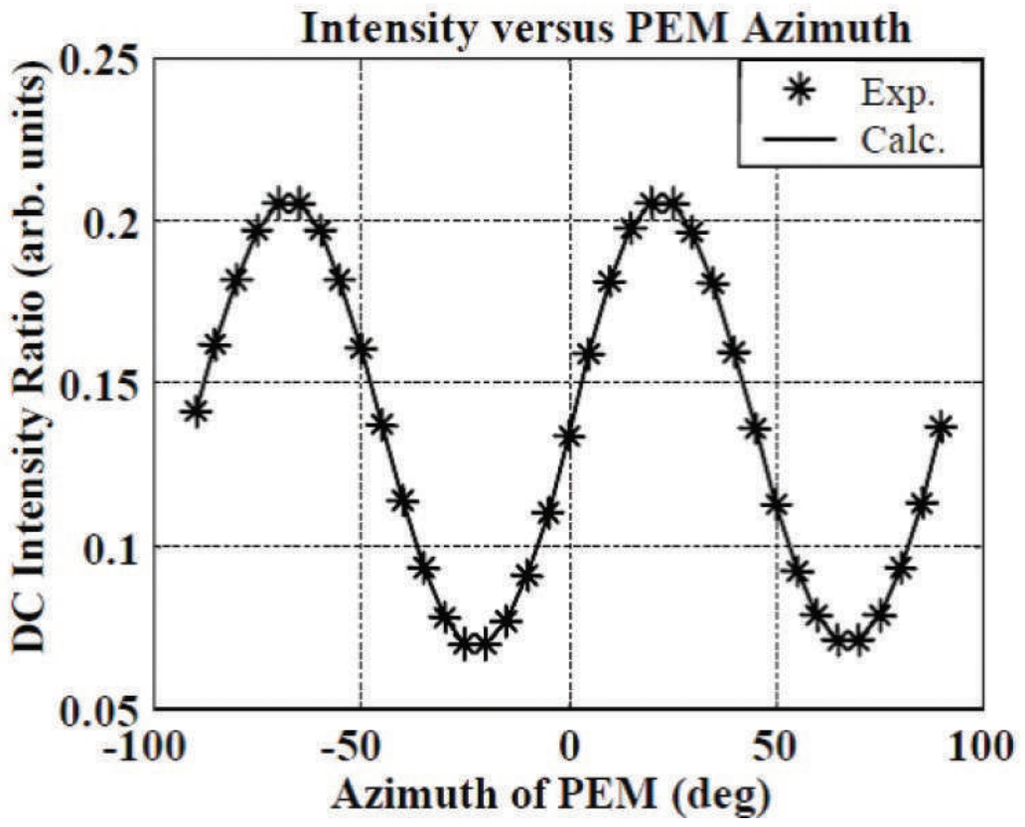

Figure 17. DC intensity distribution of the PEM ellipsometer. The azimuth angle of A is at 0° versus the azimuthal angle of the strain axis of PEM. *The experimental data and the solid line show the intensity distribution when the strain axis of PEM is at 0.2764±0.0003°.

$$\delta\theta_0 = \frac{\tan 4\theta_0}{4\tan^2\Psi}\frac{\delta I}{I} \tag{27}$$

The intensity fluctuation can be large at $\theta_0 = 22.5^\circ$, which is far away from the roughly aligned value. By readjusting the θ_0 to zero, one can obtain a well-aligned PEM ellipsometry.

4.2. Calibration of the modulation amplitude of PEM

According to the last section, the strain axis of PEM can be well aligned to the incident plane, θ is zero, and the azimuth of polarizer is at 45°, Eq. (19), can be simplified as

$$I(A) = 0.5I_0\left[\sin^2 A + \tan^2\Psi \ \cos^2 A - \tan\Psi \ \sin 2A \ (\cos\Delta \ \cos\Delta_P + \sin\Delta \ \sin\Delta_P)\right] \tag{28}$$

Since the Fourier expansions of the harmonic functions are

$$\sin\Delta_P = 2J_1(\delta_0)\sin\omega t + 2J_3(\delta_0)\sin 3\omega t + \ldots \tag{29}$$

$$\cos\Delta_P = 2J_0(\delta_0) + 2J_2(\delta_0)\sin 2\omega t + 2J_4(\delta_0)\cos 4\omega t + \ldots \tag{30}$$

One can prove the following relation for the measurement of Ψ and Δ:

$$\sin 2\Psi = \frac{\sqrt{\left(\frac{I_{1f}(45^\circ)}{J_1(\delta_0)}\right)^2 + \left(\frac{I_{2f}(45^\circ)}{J_2(\delta_0)}\right)^2}}{I_{dc}(45^\circ) + I_{dc}(-45^\circ)} \tag{31}$$

$$\tan\Delta = \frac{I_{1f}(45^\circ)J_2(\delta_0)}{I_{2f}(45^\circ)J_1(\delta_0)} \tag{32}$$

It is very interesting to notice that the even/odd harmonics are related by the similar physical parameters except the orders of its Bessel function. So,

$$\frac{I_{1f}}{I_{3f}} = \frac{J_1(\delta_0)}{J_3(\delta_0)} \tag{33}$$

$$\frac{I_{2f}}{I_{4f}} = \frac{J_2(\delta_0)}{J_4(\delta_0)} \tag{34}$$

The modulation amplitude δ_0 can be measured by the intensity ratio of even/odd harmonics. In the operation menu of PEM [15], the value δ_0 can be calibrated by the oscilloscope waveform of a half-wave, that is, $\delta_0 = 0.5$, such as shown in **Figure 18**. However, when one is constructing a new element in a system, some defects are expected. Since one can measure the modulation amplitude by the even/odd intensity ratios, one can calibrate the modulation amplitude and compare it with the digitized oscilloscope waveform obtained from DAQ system, such as shown in **Figure 19**. The system errors, azimuth angle, and modulation amplitude can be corrected after the alignment and calibration in order to establish an accurate PEM ellipsometer.

http://dx.doi.org/10.5772/intechopen.70086

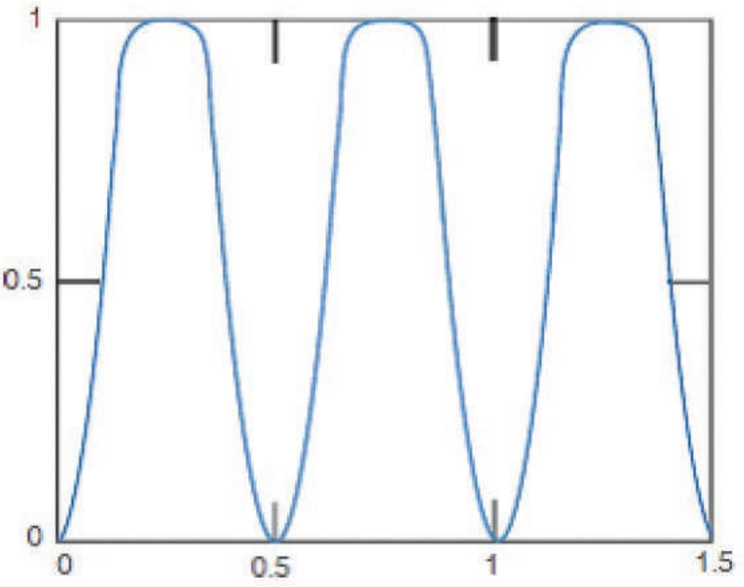

Figure 18. The oscilloscope waveforms when the modulation amplitude of PEM is a half-wave [15].

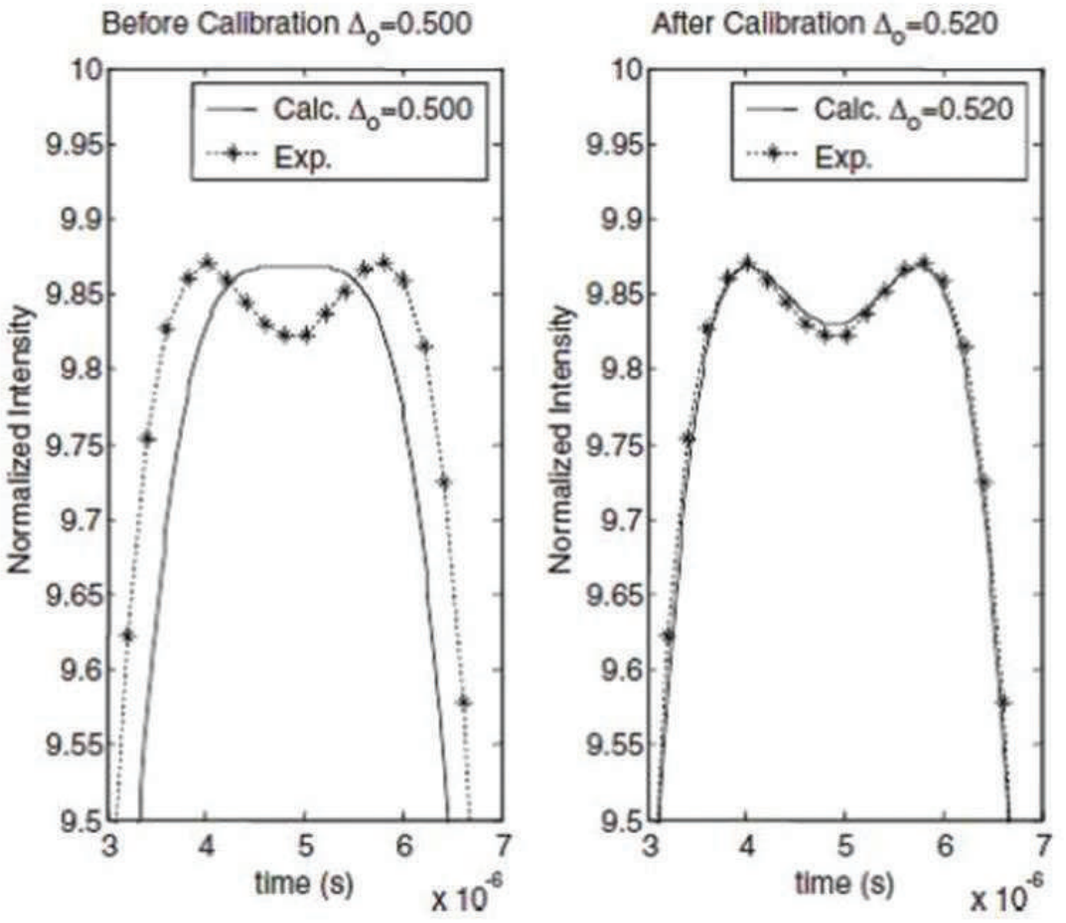

Figure 19. Recorded digitized oscilloscope waveform when the modulation amplitude of PEM has been claimed as half-wave: left—before calibration and right—after calibration.

4.3. Applications

For monitoring the physical processes, plasma etching [16], deposition [17], thermal heating [18], and photo-induced [19], one has to establish the in situ alignment technique for PEM ellipsometry. A DAQ card is an analog-to-digital converter. In the PEM ellipsometry, the multi-function DAQ (typical PCI-6111) can be used as two lock-in amplifiers for real-time measurement (10 sets/s), and post-flight analysis, that is, analyze the reflected waveform of the digital oscilloscope specification of the DAQ system, so the data rate can reach 25,000 sets/s. With the help of a stroboscope to modulate the light source, one can lock the wave at four specific phases to measure the ellipsometric parameters of the testing sample. By using CCD as the detector, an imaging ellipsometry can also be established in the PEM ellipsometry. The followings are examples for the applications of PEM ellipsometry.

4.3.1. Plasma etching

For monitoring the etching process, a plasma-etching chamber can install a PEM ellipsometer to monitor the etching process, such as the schematic setup shown in **Figure 20**. A thick wafer is used to extract the etched thickness under etching, which can be monitored by the PEM ellipsometry to avoid over-etch. After calibrating the modulation amplitude, one can etch the film to the targeted thickness by monitoring the behavior of Ψ and Δ with the theoretical predication in real time. For example, we target a thick SiO_2 on polysilicon started from around 500 nm to be etched to 30 nm. The measured value with the theoretical value, such as

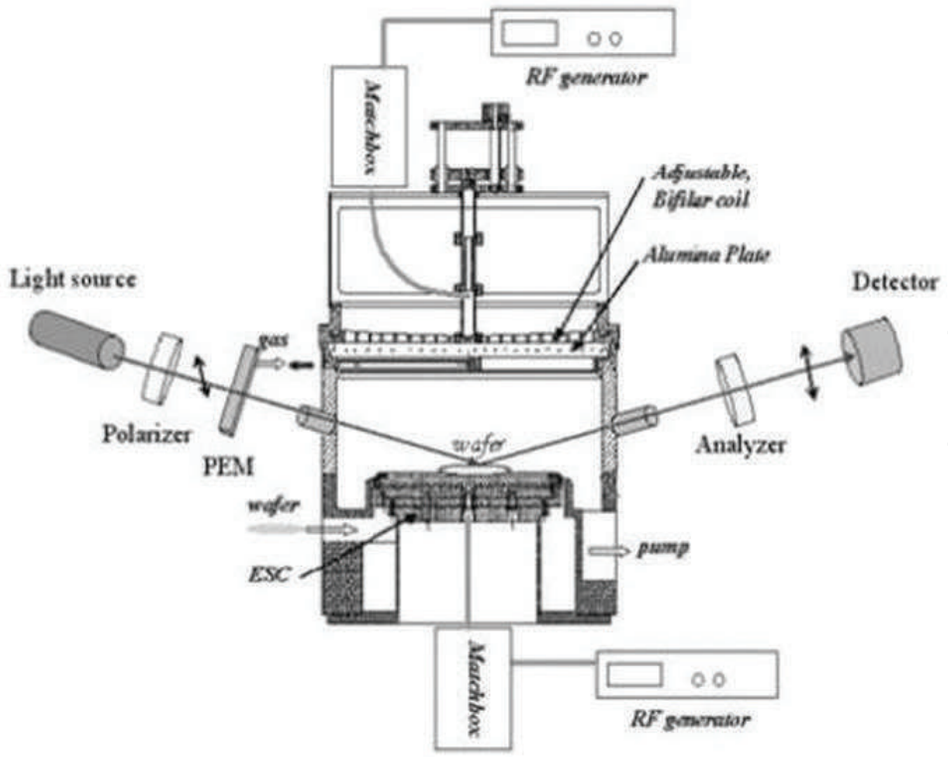

Figure 20. Schematic setup of the IPC etcher.

http://dx.doi.org/10.5772/intechopen.70086

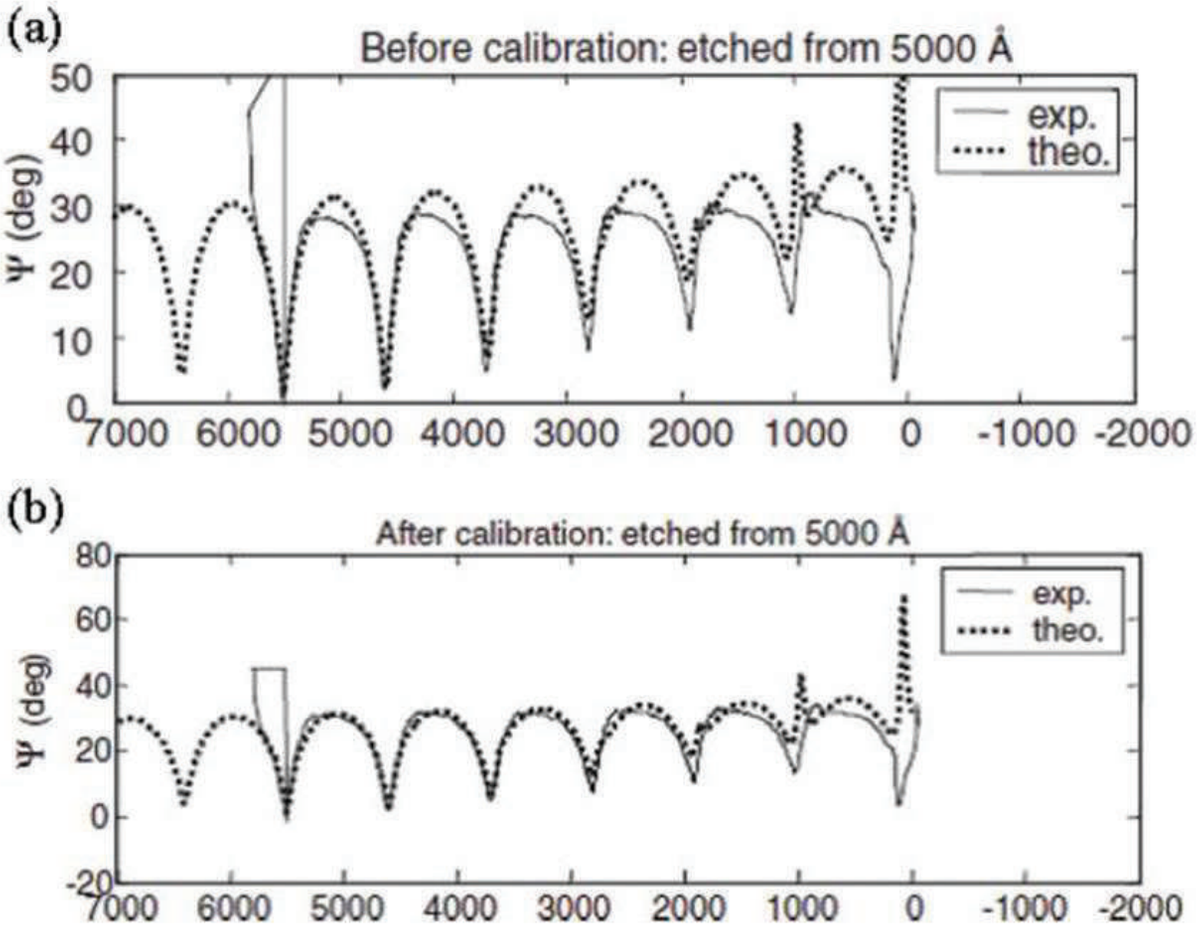

Figure 21. Distributions of Ψ for film etched from 500-nm thickness of SiO_2 on silicon substrate (a) before calibration and (b) after calibration: (dotted line) theoretical value; (solid line) measured value × fc [16].

in **Figure 21a**, the histogram of Ψ before correction, and **Figure 21b**, the histogram of Ψ after correction (fc, the correction factor from the measurement of modulation amplitude), can be compared. In the corrected curve, we observed the behavior of etching: the sharp rising of Ψ in the end cycle, around 70 nm. In the end, we can control the etching process: the etching stopped at the thickness of the film to be close to 30 nm within 0.2 nm, such as shown in **Figure 22**.

4.3.2. Thermal heating

The perovskite materials are attractive because they exhibit extremely high piezoelectric coefficients and a wide region of controlled dielectric constants when the compositions are near the morphotropic phase boundary (MPB) [20]. In previous studies, doping Ru into complex oxides can enhance the photorefractive effect in the red and near-infrared spectral regions [21]. In addition, using Ru as a dopant in various inorganic crystals can considerably improve their response time and photoconductivity [22]. Therefore, Ru-doped perovskites can be considered as practical material for optical memories. In the process of storage, the temperature of the surroundings can fluctuate due to laser irradiation, heat dissipation, and so on. However, for

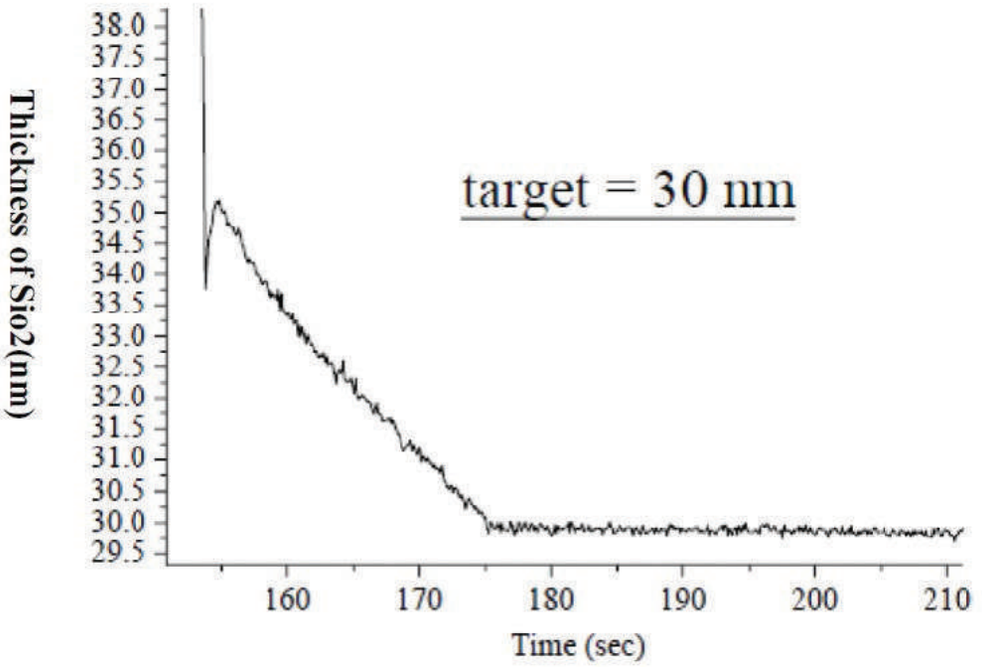

Figure 22. The histogram of an etching of SiO_2/Si, the target of the process was 30 nm.

optical storage, the refractive index of the perovskite material must be stable under the working temperature. It will be interesting to measure their refractive indices during heating in order to understand what would be the most favorable working temperature for optical storage. One can setup the PEM ellipsometry as shown in **Figure 23** to monitor the refractive index of perovskite material under heating. In the thermally isolated chamber, the samples can be heated from room temperature to 200°C by the thermoelectric cooler (TE cooler), which operates based on the Peltier effect, so it can be used as heater when the electric current is

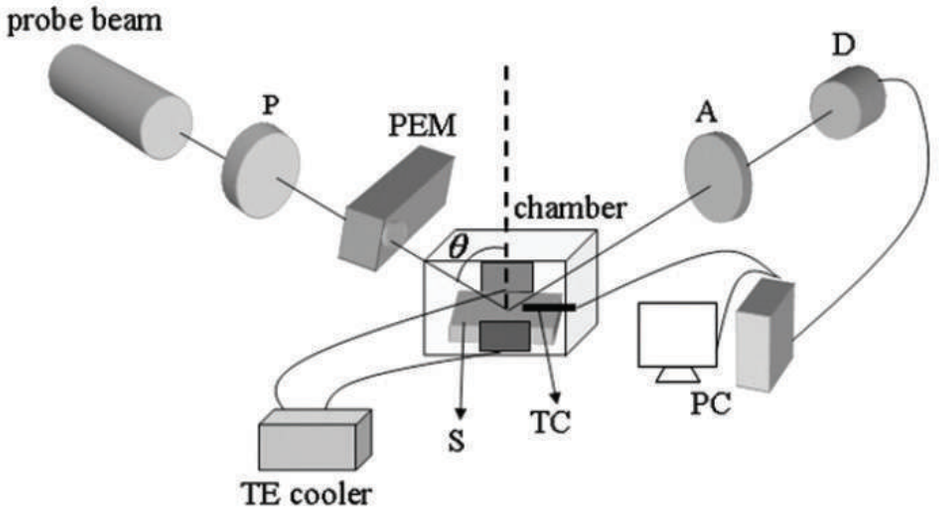

Figure 23. Schematic setup of the PEM ellipsometer for measuring the variation in the refractive index during the heating process: probe beam: HeNe laser (632.8 nm); P: polarizer; PEM: photoelastic modulator; S: sample; θ: incident angle.

http://dx.doi.org/10.5772/intechopen.70086

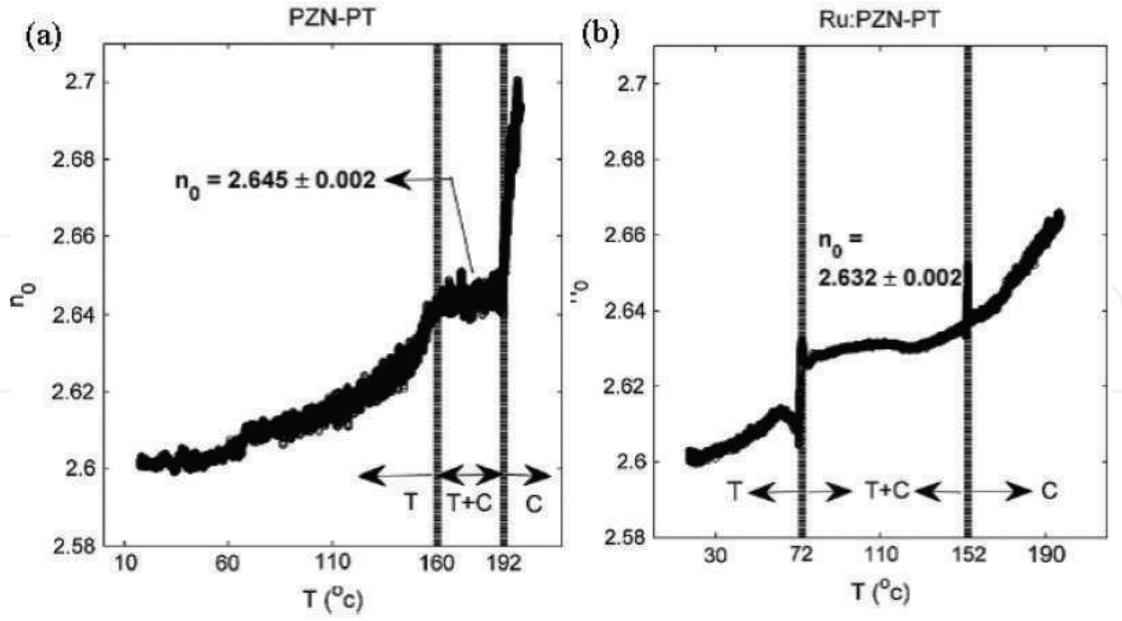

Figure 24. Refractive indices of (a) pure 0.9PZN-0.1PT and (b) Ru-doped 0.9PZN-0.1PT against temperature during heating: T: tetragonal; C: cubic.

inversely applied. The TE cooler is small but highly reliable. The sample can be sandwiched between two TE coolers to maintain uniformity of temperature of the sample. A k-type thermocouple was attached to the surface of the sample to monitor the temperature. The voltage produced by the thermocouple can be acquired by one of the channels of the same data acquisition system. The voltage is then converted to the required temperature scale according to the NIST ITS-90 Thermocouple Database. In this way, both the temperature and the ellipsometric parameters can be simultaneously monitored. According to the study by Chuang et al. [18], the ellipsometric parameters of pure and Ru-doped 0.9PZN–0.1PT were measured by PEM ellipsometry with a sampling rate of 10 sets/s. The refractive indices were converted from the measured Ψ and Δ, such as shown in **Figures 24a** and **b**. From the results of the experiment, one can conclude that when Ru is used as a dopant in 0.9PZN–0.1PT, the Curie region is broadened and shifted closer to room temperature. Therefore, the PEM ellipsometry can be used to analyze the behavior of material under heating.

4.3.3. Photo-induced effect

Holographic data storage has been considered to be a promising data storage technology because it provides high storage density and fast readout rate. One of the fundamental issues for this technique to be successful is the availability of thick recording materials. Recently, research involving organic photopolymers has become of interest because of the flexibility for fabrication. Photopolymers exhibit a photorefractive effect, and the photo-induced changes in the refractive index can be used to record the holographic interference pattern in order to form phase grating. Based on this idea, many new photopolymers have been synthesized and studied. The photo-induced refractive index variation and photo-induced birefringence are two of the most often used mechanisms for producing the necessary changes in refractive

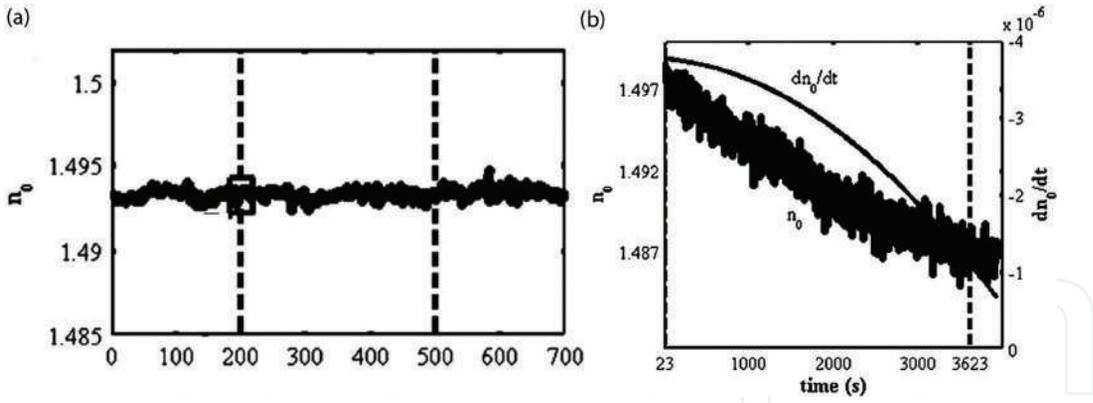

Figure 25. Histogram of measured refractive index during heating: (a) pure PMMA: the 488-nm laser was turned on at the 200th second and then turned off at the 500th second. The average refractive index is 1.493±0.003; (b) PQ-doped PMMA: the 488-nm laser was turned on at the 23rd second and turned off at the 3623rd second; the refractive changes from 1.497 to 1.487. It is exposed to 488 nm (Ar/Kr tunable laser) with total exposure energy density of 68.4 J/cm^2.

indices for holographic recording. Thus, various methods have been proposed for investigating these two effects in different photopolymers for further improving the properties of the recording materials. The refractive indices of the photopolymers have been measured by an Abbe refractometer and a prism coupler, but the variation of the refractive index is commonly extracted from the diffraction formula by measuring the diffraction efficiency of a recorded grating [23]. Since the PEM ellipsometry can measure the refractive index during exposure, one can compare the photorefractive effect of photopolymers under irradiation. The PEM ellipsometry was used to measure the pure and doped PMMA, such as shown in **Figures 25a** and **b**. From these two measurements, one can conclude that the holographic recording in PQ-doped PMMA was mainly due to the change in the refractive index. The change in the refractive index is produced by molecular structure changes of the PQ molecules. This in situ/real time can observe the structure change under irradiation.

4.3.4. Post-flight analysis

Since most data acquisition systems are multi-function systems, if the PEM ellipsometry employs its function of lock-in amplifier to measure dc, 1f, and 2f signals for deducing the ellipsometric parameters, one can only obtain a data rate of 10 sets/s. In Section 4.2, the DAQ system has been used as digital oscilloscope for calibrating the modulation amplitude of PEM. The waveform obtained from the digital oscilloscope can be stored for post-flight analysis. The ellipsometric parameters can be obtained by fast Fourier transform of the stored waveform. In this case, the PEM ellipsometry can reach the speed limit of PEM, since Hinds PEM90 operated at an oscillating frequency around 50 kHz, so its data rate can reach 25,000 sets/s, for example, if one wishes to measure the response time of twisted nematic liquid crystals. It is known that the response time of twisted nematic liquid crystals (TN-LC) is in the millisecond regime, the transmitted PEM-DAQ ellipsometry can be used to analyze the variation of its ellipsometric parameters under a square wave. **Figure 26** shows the histogram of the ellipsometric parameters of a TN-LC cell applying a 5-Hz square wave with a step voltage of 5 V. From the graph, one can measure the rising time and fall time of the TN-LC, which are 7.5 and 19 ms, respectively.

http://dx.doi.org/10.5772/intechopen.70086

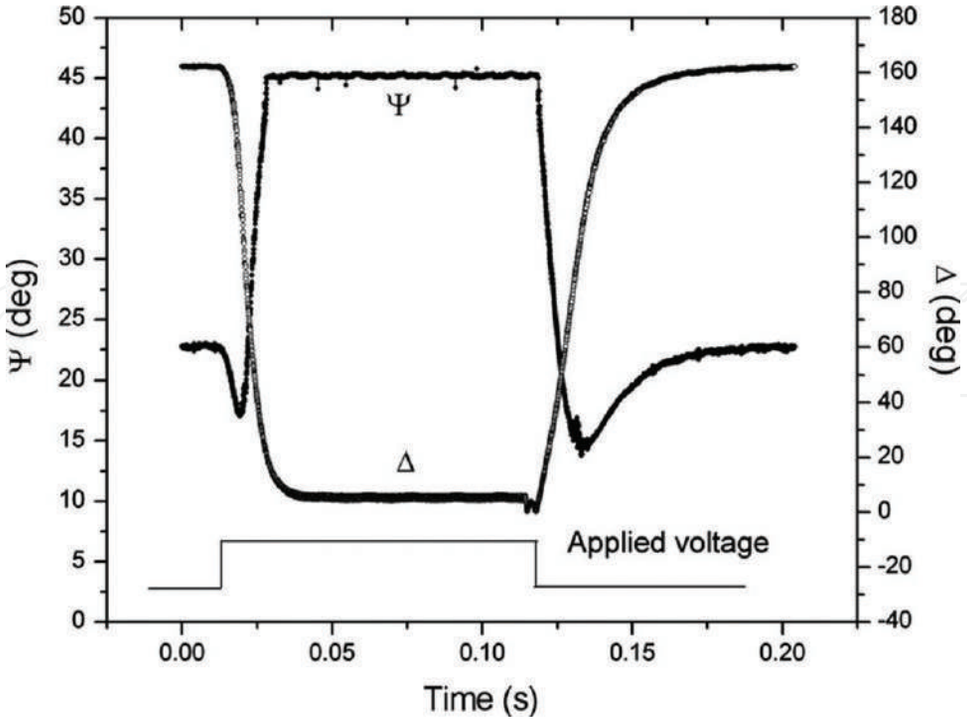

Figure 26. Histograms of measured ellipsometric parameters for the twisted nematic liquid crystal cell (transmission ellipsometry, λ = 632.8 nm). A square wave of 5 Hz and strength 5 V was applied.

The generalized ellipsometry (GE) has been developed to measure the refractive indices of anisotropic crystals [24]. In GE, at least three polarization states have to be used for extracting the physical parameters of anisotropic crystals. Using a fixed polarizer and PEM, one can generate various polarization states (200/cycle, Hinds90) because of the harmonic oscillation property of PEM. Two modulators of generalized ellipsometry [25] have been developed to measure the anisotropic medium. Due to the development of inverse problem in optics, Chuang et al. [26] implemented the program of Hodgkinson (BTF tool box) to simulate the reflected intensity profile. This profile can be analyzed and compared with the digitized waveform obtained from DAQ system of PEM ellipsometer. In his study, he found a distinguished characteristic in the reflected waveform for different complex refractive indices. Instead of using the Fourier transform on the waveform, he analyzed the reflected/transmitted waveform to extract the physical parameters. In the same reference, he proved that two incident angles are required to extract the complex refractive indices and the orientation of its optical axis of the anisotropic crystal. First, he concentrated his analysis on the reflected waveform at the incident angle of 70°. According to the Fresnel reflection coefficient of a uniaxial crystal, one can graph the normalized reflected intensity waveform as **Figure 27a**. The asymmetric distribution provides the information of absorbing or nonadsorbing materials. Assume $k_{ave} = 0.5(k_e+k_o)$ and $\Delta k = k_e - k_o$ are the averaged and difference between the extinction of ordinary and extraordinary coefficients, respectively, and $n_{ave} = 0.5(n_e+n_o)$ and $\Delta n = n_e - n_o$ are the averaged and difference between ordinary and extraordinary refractive indices, respectively. Using **Figures 27b** and **c**, one can conclude that the value of averaged extinction coefficient and difference can be estimated from the height (H) of the dip by the parametric

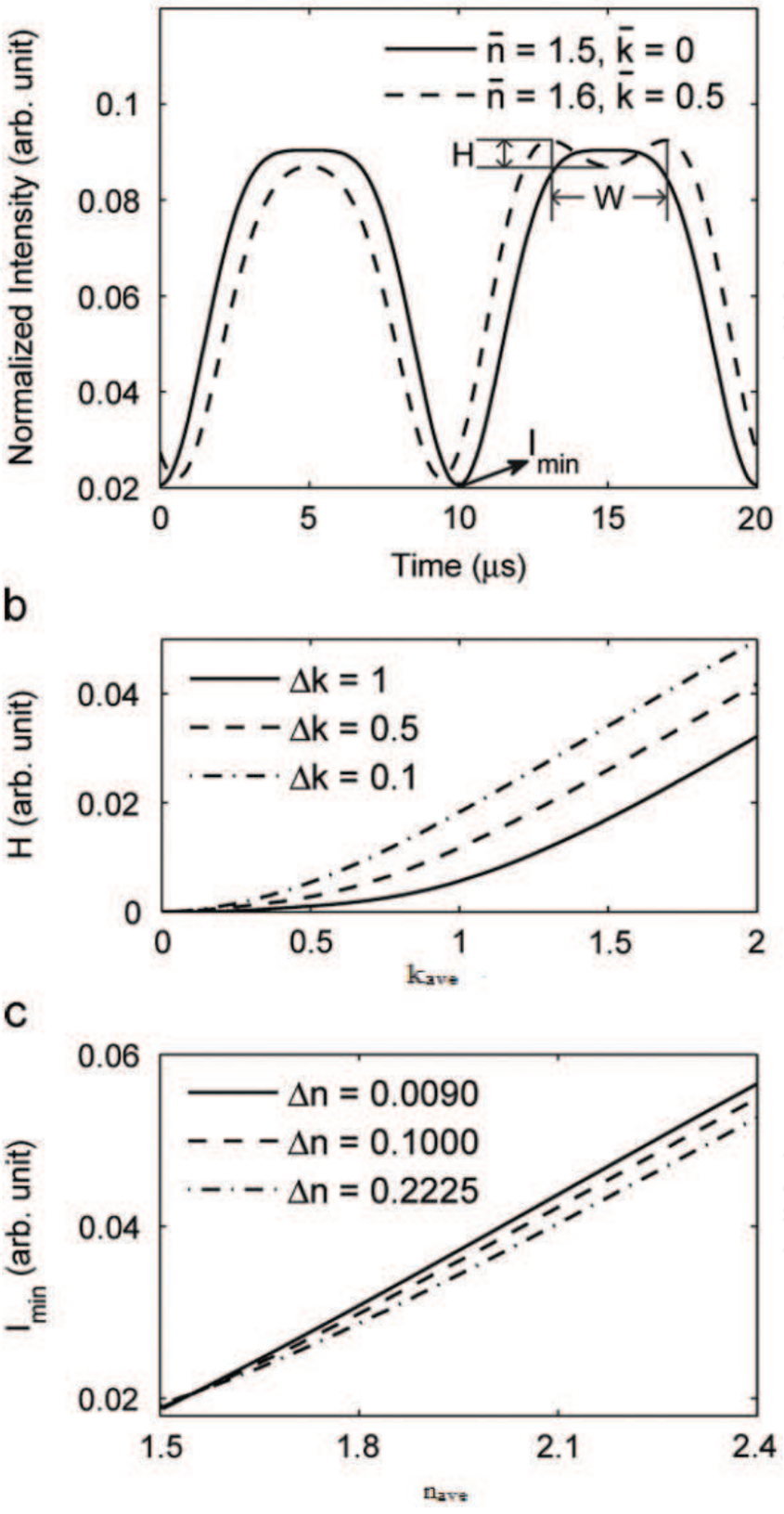

Figure 27. Estimation for complex refractive index (θ_i=70°): (a) the normalized reflected intensity profile; (b) the parametric equations of the dip depth (H) versus the averaged extinction coefficient (k_{ave}); and (c) the parametric equations of the minimum intensity (I_{min}) versus the averaged refractive indices (n_{ave}).

http://dx.doi.org/10.5772/intechopen.70086

$k_{ave} = 0.5(k_e+k_o)$	$H_{70} = p_0 + p_1 k_{ave} + p_2 k_{ave}^2$
$\Delta k = k_e - k_o$	$p_0 = -0.002 + 0.003\Delta k$
	$p_1 = -0.015 + 0.021\Delta k$
	$p_2 = 0.006 + 0.005\Delta k$

Table 4. The parametric equations of dip height H for estimating the extinction coefficients obtained by simulated reflected waveform when θ_t at 70°.

$n_{ave} = 0.5(n_e+n_0)$	$I_{70min} = q_0 + q_1 n_{ave}$
$\Delta n = n_e - n_0$	$q_0 = -0.046 + 0.031\Delta n$
	$q_1 = 0.043 + 0.022\Delta n$

Table 5. The parametric equations of I_{min} for estimating the refractive coefficient obtained by simulated reflected waveform when θ_t at 70°.

equations (**Table 4**). The averaged refractive index can be estimated by the minimum intensity I_{min} of the waveform, which is linearly related to the average refractive index (**Table 5**). It is known that the genetic algorithm is the mechanism of nature evolution and is considered as the optimal solution in the complex multidimensional search spaces. The parametric equations really can narrow down the searching region in genetic algorithm. Since the genetic algorithm [27] has been applied in ellipsometry, one can simulate the waveform and find the characteristic property to narrow down the searching region, then to search the complex refractive indices and the orientation of optical axis. Using two optimized incident angles, Chuang et al. [26] extracted the n_o and n_e of quartz crystal to be 1.543 and 1.552, respectively. In addition, the orientation of its optical axes was also measured from the same

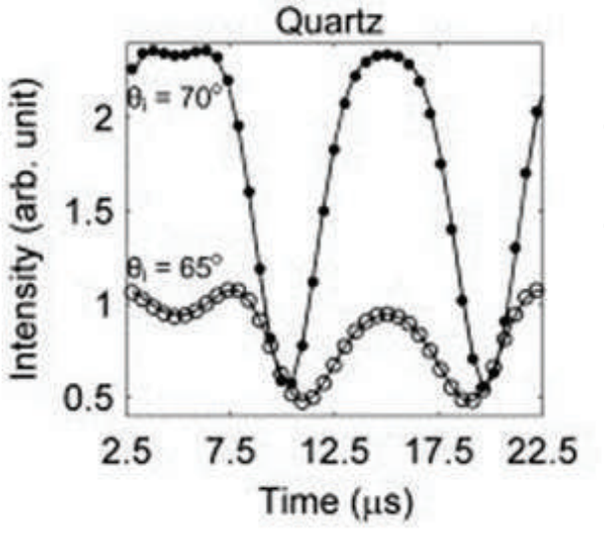

Figure 28. Measured reflected intensity profiles of quartz at incident angles of 65° (o) and 70° (●). All these measured values are compared with the calculated values (-). Only 1/5 data points in each cycle are displayed.

waveform. **Figure 28** shows the comparison between simulated waveform by using the extracted physical parameters (refractive indexes, orientation of optical axis) and measured values. This work presents the powerfulness of the post-flight analysis technique; one only has to use one cycle (20 μs of Hinds PEM 90) of the reflected intensity signals to extract all the optical parameters.

5. Future prospects

The three-intensity measurements technique in PSA ellipsometry can be easily constructed into the imaging ellipsometry. In this system, the rotation of polarizer and analyzer not only slows down the measuring speed but also causes the incident beam to deviate from its setting. This is the reason for establishing the PEM ellipsometry. However, the modulation frequency of PEM is very high (most PEM operates in 50 kHz), and one must use fast response detector for PEM ellipsometry. The operation of CCD camera is a time-consuming process in comparing with the modulation frequency of PEM. The PEM imaging ellipsometry can only be established by employing the modulated laser diode as pulse for strobe illumination [28] at four specific phases. In this technique, one has to calibrate the initial phase for synchronizing the four specific phases to perform ellipsometric measurements. Again, with the help of symbolic computer program, Mathematica, Tsai [29] de-associated the initial phase by extra strobe measurement. This PEM stroboscopic imaging ellipsometry can measure a moving sample dynamically, such as the motion of dropping oil on SiO_2 film. The speed of measurement can be improved by using high-power light source to reduce the exposure time and high-speed DAQ system to match the data transfer of CCD.

For further developing the ellipsometry, one can use the liquid crystal variable retarder to replace PEM. It is interesting to notice [30] a three-intensity measurements technique in ellipsometry by varying the phase retardation of liquid crystal instead of varying the polarization by rotating any part of the system. In addition to a liquid crystal variable retarder, a quarter wave plate has been introduced to form an ellipsometer without any mechanical motion. The in situ calibration of the liquid crystal variable retarder has to be performed. Just like the three-intensity measurement in PSA ellipsometry, one can install a liquid crystal variable retarder by varying three phases to form an imaging ellipsometry. Polarizer and quarter wave plate can be formed as polarization generator, liquid crystal variable retarder and analyzer can be packed as polarization analyzer. Since all these components are light-weight with low cost, one can construct a compact and portable system for imaging ellipsometric measurements. The only disadvantage of liquid crystal variable retarder is its stability in temperature. For accurate measurement, one has to use a temperature controller. We await the improvement of the liquid crystal variable retarder for the establishment.

Acknowledgements

All these works were accomplished by my students under the grants of National Science Council in Taiwan.

http://dx.doi.org/10.5772/intechopen.70086

Author details

Yu-Faye Chao

Address all correspondence to: yfchao@mail.nctu.edu.tw

Department of Photonics, National Chiao Tung University, Taiwan, ROC

References

[1] Azzam RMA, Bashara NM. Ellipsometry and Polarized Light. Paperback. North Holland: Elsevier Science Publishers B.V.; 1987

[2] Collins RW. Automatic rotating element ellipsometers: Calibration, operation, and real-time applications. Review of Scientific Instruments. 1990;**61**:2029-2062. DOI: 10.1063/1.1141417

[3] Chao YF, Wei CS, Lee WC, Lin SC, Chao TS. Ellipsometric measurements and its alignment: Using the intensity ratio technique. Japanese Journal of Applied Physics. 1995;**34**:5016-5019. DOI: 10.1143/JJAP.34.5016

[4] Chao YF, Lee WC, Hung CS, Lin JJ. A three-intensity technique for polarizer-sample-analyser photometric ellipsometry and polarimetry. Journal of Physics D: Applied Physics. 1998;**31**:1968-1974. DOI: 10.1088/0022-3727/31/16/005

[5] Steel MR. Method for azimuthal alignment in ellipsometry. Applied Optics. 1971;**10**:2370-2371

[6] Wang MW, Chao YF. Azimuth alignment in photoelastic modulation ellipsometry at a fixed incident angle. Japanese Journal of Applied Physics. 2002;**41**:3981-3986. DOI: 10.1143/JJAP.41.3981

[7] Chao YF, Lee KY, Lin YD. Analytical solutions of the azimuthal deviation of a polarizer and an analyzer by polarizer-sample-analyzer ellipsometry. Applied Optics. 2006;**45**:3935-3939. DOI: 10.1364/ao.45.003935

[8] Chao YF, Wang MW, Ko ZC. An error evaluation technique for the angle of incidence in a rotating element ellipsometer using a quartz crystal. Journal of Physics D: Applied Physics. 1999;**32**:2246-2249. DOI: 10.1088/0022-3727/32/17/315

[9] Tomlinson WJ. Application of GRIN-rod lenses in optical fiber communication systems. Applied Optics. 1980;**19**:1127-1138. DOI: 10.1364/AO.19.001127

[10] Garratt J, Mills M. Measurement of the roughness of supersmooth surfaces using a stylus instrument. Nanotechnology. 1996;**7**:13-20. DOI: 10.1088/0957-4484/7/1/002

[11] D'Acquisto L, Fratini L, Siddiolo AM. A modified moiré technique for three-dimensional surface topography. Measurement Science and Technology. 2002;**13**:613-622. DOI: 10.1088/0957-0233/13/4/326

[12] Han CY, Lee ZY, Chao YF. Determining thickness of films on a curved substrate by use of ellipsometric measurements. Applied Optics. 2009;**48**:3139-3143. DOI: 10.1364/AO.48.003140

[13] Han CY, Du CY, Chen YR, Chao YF. Developing a phase and intensity measurement technique with multiple incident angles under surface plasmon resonance condition. Proceedings of SPIE. September 2013;**8905**:89052N:1-7. DOI: 10.1117/12.2035029

[14] Jasperson SN, Schnatterly SE. An improved method for high reflectivity ellipsometry based on a new polarization modulation technique. Review of Scientific Instruments. 1969;**40**:761-767. DOI: 10.1063/1.1684062

[15] Oakberg T, Wang B. Light intensity modulation using a PEM. Technology for Polarization Measurement. 2000:1-3 http://www.hindsinstruments.com/wp-content/uploads/Light-Intensity-Modulation.pdf

[16] Wang MW, Chao YF, Leou KC, Tsai FH, Lin TL, Chen SS, et al. Calibrations of phase modulation amplitude of photoelastic modulator. Japanese Journal of Applied Physics. 2004;**43**:827-832. DOI: 10.1143/JJAP.43.827

[17] Collins RW. In situ ellipsometry of thin-film deposition: Implications for amorphous and microcrystalline Si growth. Journal of Vacuum Science & Technology. B. Microelectronics and Nanometer Structure. 1989;**B7**:1155-1164. DOI: 10.1116/1.584566

[18] Chuang CI, Marinova V, Lin SH, Chao YF. Phase-modulated ellipsometry for probing the temperature-induced phase transition in ruthenium-doped lead zinc niobate-lead titanate single crystal. Thin Solid Films. 2011;**519**:2867-2869. DOI: 10.1016/j.tsf.2010.12.085

[19] Chuang CI, Hsiao YN, Lin SH, Chao YF. Real-time measurement of photo-induced effects in 9,10-phenanthrenequinone-doped poly(methyl methacrylate) photopolymer by phase-modulated ellipsometry. Optical Communication. 2010;**283**:3279-3283. DOI: 10.1016/j.optcom.2010.04.036

[20] Liu W, Ren X. Large piezoelectric effect in Pb-free ceramics. Physical Review Letters. 2009;**103**:257602 1-4. DOI: 10.1103/PhysRevLett.103.257602

[21] Lin CH, Huang CY, Chang JY. Increasing the conductivity of photorefractive $BaTiO_3$ single crystals by doping Ru. Applied Surface Science. 2003;**208–209**:340-344. DOI: 10.1016/S0169-4332(02)01393-4

[22] Rakitina L, Gospodinov M, Briat B. Photorefractive and photochromic properties of Ru doped Sr0:61Ba0:39Nb2O6 crystal. Optical Communication. 2002;**213**:373-378. DOI: 10.1016/S0030-4018(02)02124-7

[23] Robinson TG, DeCorby RG, McMullin JN, Haugen CJ, Kasap SO, Tonchev D. Strong Bragg gratings photoinduced by 633-nm illumination in evaporated As2Se3 thin films. Optics Letters. 2003;**28**:459-461. DOI: 10.1364/OL.28.000459

[24] Azzam RMA, Bashara NM. Application of generalized ellipsometry to anisotropic crystals. Journal of the Optical Society of America. 1974;**64**:128-133. DOI: 10.1364/JOSA.64.000128

[25] Jellison GE, Modine F. Two-modulator generalized ellipsometry: Theory. Applied Optics. 1997;**36**:8190-8198. DOI: 10.1364/AO.42.003765

[26] Chuang CI, Lin SH, Chao YF. Rapid and accurate extraction of optical parameters for uniaxial bulk media by phase modulated ellipsometry. Optics and Lasers in Engineering. 2013;**51**:861-866. DOI: 10.1016/j.optlaseng.2013.02.004

[27] Cormier G, Boudreau R. Genetic algorithm for ellipsometric data inversion of absorbing layers. Journal of the Optical Society of America A: Optics, Image Science and Vision. 2000;**17**:129-134. DOI: 10.1364/JOSAA.17.000129

[28] Han CY, Chao YF. Photoelastic modulated imaging ellipsometry by stroboscopic illumination technique. Reviews in Scientific Instruments. 2006;**77**:1-5. DOI: 10.1063/1.2173027

[29] Tsai HM, Chen CW, Tsai TH, Chao YF. Deassociate the initial temporal phase deviation provided by photoelastic modulator for stroboscopic illumination polarization modulated ellipsometry. Reviews in Scientific Instruments. 2011;**82**:5-10. DOI: 10.1063/1.3568745

[30] Shih W, Hsieh M, Chao YF. A compact in-situ ellipsometer using the liquid crystal variable retarder. Proceedings of SPIE. September 5, 2014;**9200**:1-7. DOI: 10.1117/12.2060567